

学位論文

Construction of Photochemical Water Oxidation System
Catalyzed by Ruthenium Complexes in Vesicles

(ルテニウム錯体を触媒とする
ベシクル中における水の光酸化反応系の構築)

平成 27 年 12 月博士 (理学) 申請

東京大学大学院理学系研究科

化学専攻

佐藤 洋一

Abstract

In this dissertation, with the aim of the construction of novel water splitting system utilizing vesicles as a reaction field, photochemical water oxidation catalyzed by Ru complexes embedded into vesicle membranes is reported.

In Chapter 1, as a general introduction, natural photosynthetic system is outlined, and the components of the system are classified as three parts by their roles: light harvesting, electron transport, and light-chemical energy conversion. In this chapter, artificial reaction systems mimicking the natural photosynthetic system are also introduced, and as a model of photosynthetic system, the usefulness of vesicles as a reaction field is noted. In §1.3, a brief introduction of Ru complexes and other metal complexes known to act as water oxidation catalysts is provided.

In Chapter 2, substituent effects on the catalytic activity of a Ru complex are investigated to find suitable structure for the photochemical water oxidation in vesicles. A series of complexes $\text{Ru}(\text{bda})(\text{pyR})_2$ (**1–6**; $\text{bda} = 2,2'$ -bipyridine-6,6'-dicarboxylate, $\text{pyR} =$ pyridine having a substituent R at the 4-position, $\text{R} = \text{OMe}, \text{Me}, \text{H}, \text{Br}, \text{CO}_2\text{Me},$ and CF_3) were prepared and examined for their photophysical and electrochemical properties. Then, chemical water oxidation using $\text{Ce}(\text{NH}_4)_2(\text{NO}_3)_6$ (CAN) as an oxidant and photochemical water oxidation using $[\text{Ru}(\text{bpy})_3]^{2+}$ as a sensitizer and $\text{S}_2\text{O}_8^{2-}$ as a sacrificial electron acceptor were performed in a homogeneous solution. The catalytic activities of the complexes were evaluated by initial consumption rates of Ce(IV) in the chemical oxidation and initial oxygen evolution rates in the photochemical oxidation. As a result of both chemical and photochemical reactions, it was found that the complexes with electron-withdrawing groups ($\text{R} = \text{CO}_2\text{Me}, \text{CF}_3$) have especially high catalytic activity. This result encouraged the author to design a novel amphiphilic Ru complex, $\text{Ru}(\text{bda})(\text{pyCO}_2\text{Me})(\text{pyCO}_2\text{Ocd})$ (**5R**; $\text{Ocd} = n$ -octadecyl), for the photochemical water oxidation in vesicles. On the other hand, the OMe-substituted complex exhibited relatively higher catalytic activity than the Me-substituted and unsubstituted complexes. This indicates that reaction steps accelerated by electron-donating groups also affect the overall reaction rate of the water oxidation.

In Chapter 3, complex **5R** having a long alkyl chain connected by an ester bond was synthesized. The photophysical and electrochemical properties of **5R** were found to be almost identical to those of complex Ru(bda)(pyCO₂Me)₂ (**5**). However, complex **5R** was moderately incorporated into DPPC vesicle membranes, while the incorporation of complex **5** was not observed almost at all. Photochemical water oxidation catalyzed by complex **5R** embedded into vesicle membranes successfully proceeded in the presence of [Ru(bpy)₃]²⁺ and S₂O₈²⁻ in the outer aqueous phase. Moreover, it was found that the turnover number (TON) and turnover frequency (TOF) of the photoinduced oxygen evolution in the vesicular system were more than twice as much as those in the homogeneous system using complex **5** as the catalyst. To obtain information about the vesicular photochemical water oxidation system, dependence of the catalytic activity on the concentrations of the sensitizer, the electron acceptor, and the catalyst was investigated. The initial oxygen evolution rate was saturated at the point where the sensitizer fully absorbed incident light and the excited sensitizers were fully quenched by the electron acceptor. It was also found that the initial oxygen evolution rate increased linearly with an increase in the catalyst concentration both in the vesicular and homogeneous system. However, in the low catalyst concentration region, the TOF in the vesicular system was more than twice as much as that in the homogeneous system, indicating that vesicles enhanced the catalytic efficiency of the Ru complex.

Table of Contents

Chapter 1	General Introduction	1
1.1	Natural photosynthetic system	1
1.1.1	Light harvesting	1
1.1.2	Electron transport	3
1.1.3	Energy conversion	5
1.2	Artificial photosynthetic system	7
1.2.1	Light harvesting	7
1.2.2	Electron transport	9
1.2.3	Energy conversion	15
1.3	Water oxidation	20
1.3.1	Water oxidation catalyzed by ruthenium complexes	20
1.3.2	Water oxidation catalyzed by iridium complexes	22
1.3.3	Water oxidation catalyzed by other metal complexes	23
1.4	Overview of this thesis	24
	References and notes	25
Chapter 2	Substituent Effect on Water Oxidation Catalyzed by Ruthenium Complexes	27
2.1	Introduction	27
2.2	Results and discussion	29
2.2.1	Synthesis	29
2.2.2	¹ H NMR spectroscopy	30
2.2.3	Photophysical properties	31
2.2.4	Cyclic voltammetric measurement	33
2.2.5	Theoretical calculation	35
2.2.6	Chemical water oxidation	43
2.2.7	Photochemical water oxidation	44

2.2.8	Quenching experiments	46
2.2.9	Reaction mechanism	52
2.3	Summary	55
2.4	Experimental	57
	References and notes	64
 Chapter 3 Photochemical Water Oxidation in Vesicles		66
3.1	Introduction	66
3.2	Results and discussion	68
3.2.1	Synthesis	68
3.2.2	Photophysical properties	70
3.2.3	Cyclic voltammetric measurement	71
3.2.4	Incorporation into the vesicle membranes	72
3.2.5	Photochemical water oxidation	77
3.2.6	Dependence on the concentration of the sensitizer	79
3.2.7	Dependence on the concentration of the electron acceptor	82
3.2.8	Emission quenching	83
3.2.9	Dependence on the concentration of the catalyst	90
3.2.10	Reaction mechanism	93
3.3	Summary	95
3.4	Experimental	97
	References and notes	101
 Chapter 4 Conclusion		102
 Acknowledgement		105
 List of Publications		106

Abbreviations

Anal.	elemental analysis
a.u.	arbitrary unit
B3LYP	Becke 3-parameter, Lee, Yang and Parr
br	broad
calcd	calculated
d	doublet
δ	chemical shift of NMR signal in ppm
DMSO	dimethyl sulfoxide
ϵ	molar extinction coefficient
Eq.	equation
ESI-MS	electrospray ionization mass spectrometry
Fc	ferrocene
GC	gas chromatography
h	hour
J	spin-spin coupling constant
λ	wavelength
λ_{em}	emission wavelength
λ_{ex}	excitation wavelength
LANL2DZ	Los Alamos National Laboratory, 2-double-zeta
LRMS	low resolution mass spectrometry
m	multiplet
M	molar
Me	methyl
MeOH	methanol
min	minute
mM	milimolar
μ M	micromolar

m.p.	melting point
nm	nanometer
ns	nanosecond
NMR	nuclear magnetic resonance
Ocd	<i>n</i> -octadecyl
quint	quintet
s	second
s	singlet
t	triplet
τ	emission lifetime
TCD	thermal conductivity detector
THF	tetrahydrofuran
UV-Vis	ultraviolet and visible
V	volt

Chapter 1 General Introduction

In this thesis, as a study on the construction of artificial systems mimicking natural photosynthesis in green plants, researches for modeling photochemical water oxidation process are presented. In this chapter, natural photosynthetic system is at first overviewed, and then the studies on artificial photosynthetic systems reported so far, as well as some examples of water oxidation catalysts, are introduced. The aim of this study and the outline of this thesis are also stated.

1.1 Natural photosynthetic system

Natural photosynthesis proceeds through three processes to transform carbon dioxide into sugars using solar energy: (i) light harvesting in the antenna complexes, (ii) charge separation in the reaction center, and (iii) energy conversion where charge separation energy is utilized to synthesize compounds having high chemical potential.^{1,2} In these processes, water is oxidized to molecular oxygen, and strong reductant, reduced nicotinamide adenine dinucleotide phosphate (NADPH), is synthesized. In addition, adenosine triphosphate (ATP) is synthesized from adenosine diphosphate (ADP) using proton concentration gradient. Then, NADPH and ATP are consumed to reduce carbon dioxide to sugars in enzymic reactions called Calvin cycle. Thus, natural photosynthesis can be assumed to be a light energy-chemical energy conversion process, and the reaction efficiency in these photochemical processes is known to be supremely high. These processes consist of complicated systems, and it can be understood as three processes stated above. In this section, a detailed account for each process is given.

1.1.1 Light harvesting

The light harvesting (LH) system is composed of chromoproteins. When light is absorbed by the antenna complexes, intermolecular excitation energy transfer is repeated, and the energy is transferred to the reaction center (RC) finally. The antenna complexes absorb light in a wide range of visible light, and the pigments are arranged and oriented so as to transfer the excitation energy with minimal losses. In different living things, the

structures of the antenna complex are known to have a wide variety although those of the reaction center have a fundamental similarity. This variation is considered to be a result that each living thing is adopted to harvest light and transfer the light energy most efficiently in its circumstances.

As a study of light harvesting system in natural photosynthesis, the antenna molecules of purple photosynthetic bacteria have been investigated in detail. In 1995, McDermott *et al.* reported that the structure of a light harvesting complex B800-850 (LH2) in a photosynthetic bacterium, *Rhodospseudomonas acidophila*, has been revealed in 2.5 Å resolution scale.³ Bacteriochlorophyll *a* (Bchl-*a*), a light harvesting pigment, is allocated in the surface part of the antenna complex and forms two groups: (i) 18 molecules of Bchl-*a* overlap with each other, construct a circular structure, and the structure is located vertically to the membrane, (ii) 9 molecules of Bchl-*a* are located horizontally to the membrane. The molecules in the former group have strong interaction between each other, and absorb light around 850 nm. The molecules in the latter group, which are located outside the former group, have not so strong interaction and absorb light around 800 nm. In addition, Walz and Ghosh reported the crystallographic image of LH1-RC complex obtained from *Rhodospirillum rubrum*, a photosynthetic bacterium, and revealed that the reaction center was positioned inside the LH1 column.⁴ Moreover, Hu and coworkers proposed a model of the bacterium photosynthetic unit.⁵ The LH1 complex is composed of chlorophylls and carotenoids in the protein, surrounding the reaction center. There are also ring-like aggregates so called LH2, which are far from the reaction center. Light energy harvested by LH2 is transport to the reaction center via LH1. Although the example of a well-studied purple photosynthetic bacterium is stated in this chapter, there are various antenna complexes in each photosynthetic living thing. The antenna system of the purple bacterium is shaped ideally, and the light energy harvested by many pigments is transferred to the reaction center with very high efficiency.

1.1.2 Electron transport

The light energy harvested by the antenna system in green plants triggers generation of charge-separated state through electron transport reactions shown in Fig.1-1, accompanied by the formation of proton concentration gradient across the thylakoid membrane. The schematic diagram showing redox potentials of molecules involved in these electron transport reactions, so called Z-scheme, is given in Fig. 1-2.

These figures show that light energy transferred from the light harvesting system to two species of chlorophyll dimer, P680 and P700, triggers many steps of electron transfer, resulting in an electron transport from water to NADP^+ and generation of a proton concentration gradient across the thylakoid membrane. Each redox species involved in this electron transport system has sufficient redox potential for the efficient electron transfer reaction.

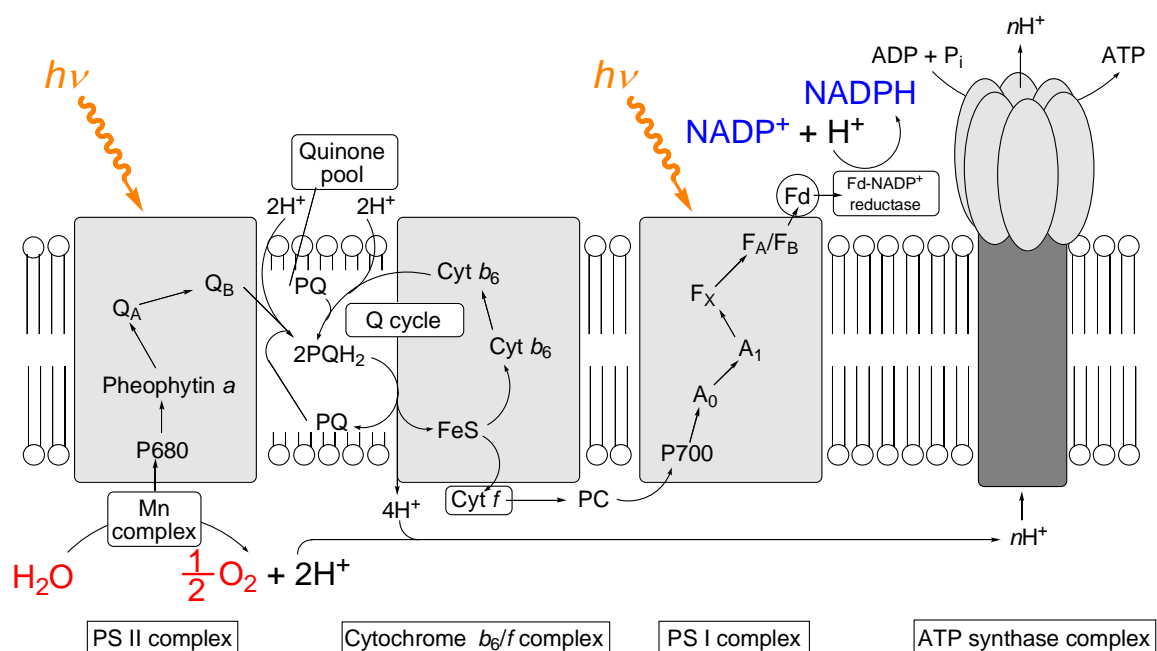


Figure 1-1. A schematic diagram of the photoinduced electron transport process in the photosynthetic system in green plants.

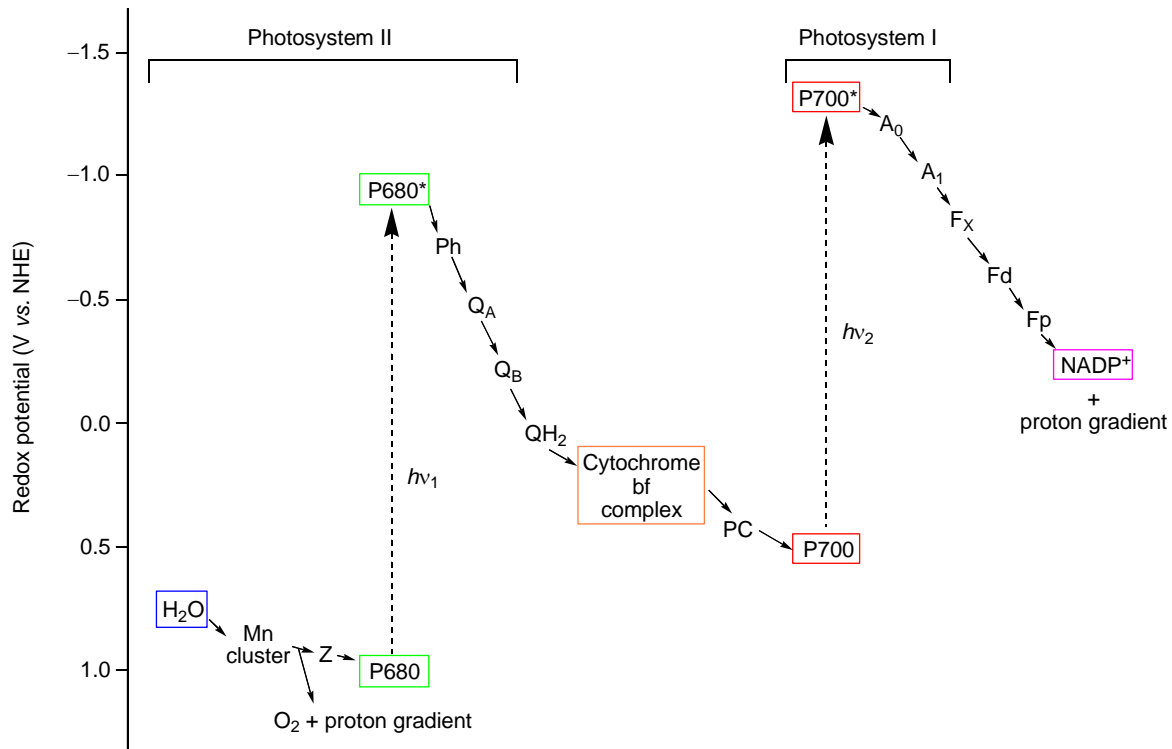


Figure 1-2. Z-scheme showing the redox potentials of the species involved in the photosynthesis of green plants.

The structure of the reaction center in a purple photosynthetic bacterium, *Rhodospseudomonas viridis*, which is revealed by X-ray crystallography, is shown in Fig. 1-3.⁶ Excitation energy is transferred to chlorophyll dimers so called special pair shown as D_A and D_B. Then, electron transfer reaction occurs from D_A to bacteriopheophytin BΦ_A, producing the charge-separated state D_A⁺-BΦ_A⁻. This means that the excitation energy is converted to charge separation energy. The electron of BΦ_A⁻ is transferred to Q_A and then to Q_B with the rate faster than that of charge recombination, and long-lived charge-separated state is formed. The whole structure of the reaction center including the special pair and bacteriochlorophylls B_A and B_B, which are not involved in the electron transport reaction, has approximately two-fold symmetry (C₂). It is known that this structure of the reaction center in each photosynthetic living thing is similar to that in each other although there are various structures in the antenna system.

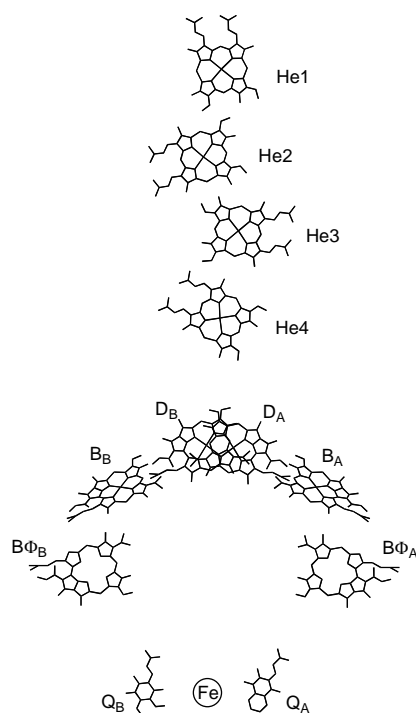
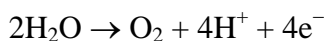
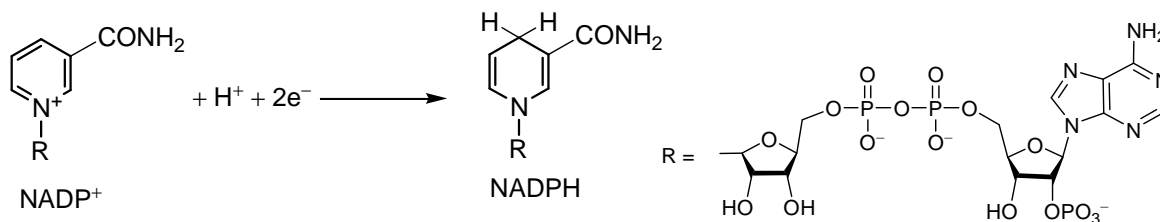


Figure 1-3. 3-Dimensional arrangement of the molecules constituting the reaction center in photosynthetic bacterium. (Frameworks composed of proteins are omitted for clarity. D; special pair, B; bacteriochlorophyll, BΦ; bacteriopheophytin, Q; quinone derivative)

1.1.3 Energy conversion

The light energy is converted to the charge separation energy in green plants via the process stated in §1.1.1 and §1.1.2, and chemically stable NADPH is then formed by two-electron reduction reaction and water is converted to oxygen by four-electron oxidation reaction. These reactions are represented by the two half reactions shown below. In these reactions, catalysts containing transition metals play an important role.



The formation of NADPH is known to be mediated by a hydrophilic protein, ferredoxin, that contains at least one 4Fe-4S cluster (Fig. 1-4).⁷ Ferredoxin is reduced through many steps of electron transfer from the reaction center. Ferredoxin-NADP⁺ reduction enzyme catalyzes the electron transfer from two molecules of reduced ferredoxin to one molecule of NADP⁺ to generate NADPH.

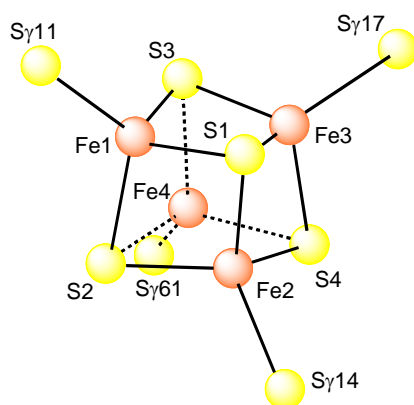


Figure 1-4. The arrangement of atoms in [4Fe-4S] cluster in the oxidized form of ferredoxin. Atoms labeled by “S γ ” represent cysteine S atoms.

On the other hand, water oxidation catalyst is known to be composed of four manganese ions. Its X-ray crystallographic image was reported by Kamiya *et al.* in 2011 and it revealed that the catalyst had a distorted chair-like shape (Fig. 1-5).⁸

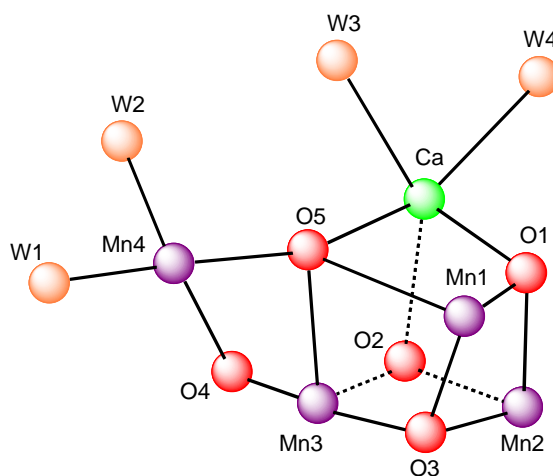


Figure 1-5. The arrangement of atoms in the Mn cluster. W represents a water molecule.

1.2 Artificial photosynthetic system

As stated in the preceding section, in natural photosynthetic system, many molecules that absorb light, transport light energy to the reaction center, mediate electron transfer between the catalysts, catalyze the formation of stable chemical species, and form reaction media such as phospholipids are involved in the photoreaction. They work collaboratively with proteins to achieve light-chemical energy conversion in high efficiency. Many researches to mimic this natural photosynthetic system were performed from various points of view, and a word “artificial photosynthesis” has various meanings. In this thesis, putting much value on significance of photosynthesis as a light energy conversion system, “artificial photosynthesis” is defined as “construction of artificial light-chemical energy conversion systems”. A short way to achieve artificial photosynthesis is imitation of natural photosynthesis, but models to extract the essence are required since natural photosynthetic system is highly advanced and complicated. In this section, focusing attention on each process (i)–(iii) described in the previous section, some examples of studies on artificially constructed photosynthetic systems are introduced.

1.2.1 Light harvesting

Light harvesting systems collect light energy and efficiently transfer it to the reaction center. Many studies have been done to construct such systems artificially. For example, Moore *et al.* have reported a phenyl acetylene dendrimer centered by a perylene moiety, in which excited energy transfer from the phenyl acetylene moiety to the perylene moiety occurs efficiently (Fig. 1-6).⁹ As an example using polymer, energy transfer from Ru complexes to Os complexes introduced to the polystyrene skeleton has been reported (Fig. 1-7).¹⁰

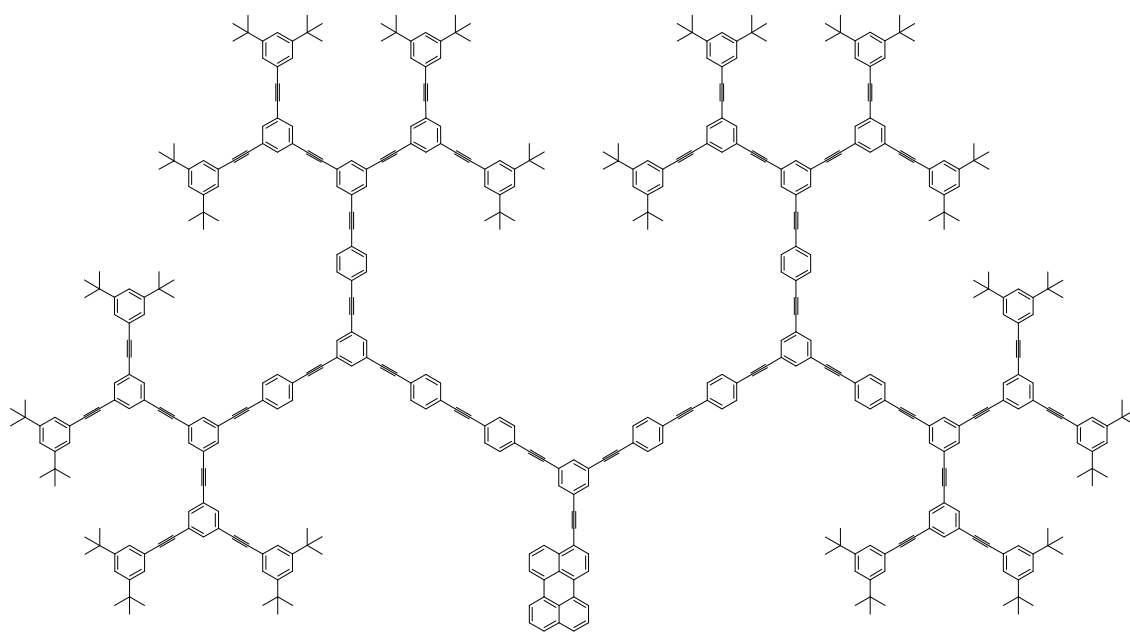


Figure 1-6. Chemical structure of the perylene-modified phenylacetylene dendrimer mimicking light harvesting system in photosynthetic system.⁹

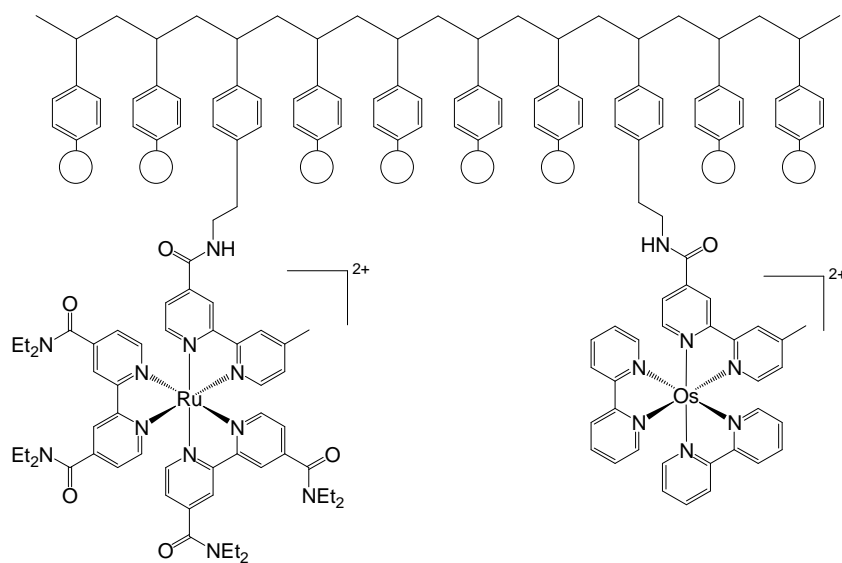


Figure 1-7. A schematic structure of the polymer modeling photothynthetic systems. Ru(II) complexes and Os(II) complexes are linked to the polystyrene skeleton by covalent bonds. Circles represent metal complexes.¹⁰

1.2.2 Electron transport

In natural photosynthetic systems, light energy collected by the light harvesting system is converted into charge separation energy. Therefore, formation of a charge-separated state having high energy utilizing light energy has been intensively studied. In this section, I will introduce some representative examples of charge-separated states formed by an intramolecular electron transfer in donor-acceptor type molecules and an intermolecular electron transfer utilizing heterogeneous reaction fields such as micelles and vesicles.

Charge separation by intramolecular electron transfer

It is known that a charge-separated state is formed by an intramolecular electron transfer in donor-acceptor (D-A) type or donor-sensitizer-acceptor (D-S-A) type molecules. When these types of molecules are photoirradiated, an electron is transferred from the donor moiety to the acceptor moiety, and their charge-separated states have long lifetimes. These studies have served important information about electron transport processes in photosynthetic systems. For example, Fukuzumi and co-workers have reported that D-S-A₁-A₂ type molecule, ferrocene-Zn porphyrin-free base porphyrin-fullerene (Fc-ZnP-H₂P-C₆₀, Fig. 1-8), forms a charge-separated state (Fc⁺-C₆₀⁻) with an exceptionally long lifetime (0.38 s).¹¹ The reduced species of fullerene (C₆₀⁻) is stable because of the delocalization of its negative charge to the entire rigid spherical molecule. Hence, fullerenes are thought to be useful electron acceptors for the formation of long-lived charge-separated states. In addition, back electron transfer is so highly exothermic that this process is in Marcus's inverted region. As a result, the back electron transfer is effectively suppressed and the charge-separated state has a particularly long lifetime.

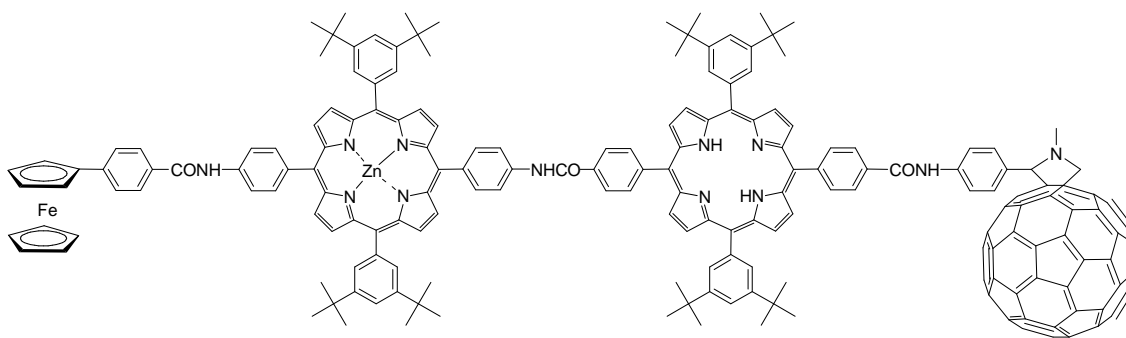


Figure 1-8. Chemical structure of Fc-ZnP-H₂P-C₆₀.¹¹

Charge separation by intermolecular electron transfer in heterogeneous system

As stated in §1.1, charge separation in photosynthetic systems of green plants is formed through the electron transport process driven by solar energy. However, charge-separated state generated by an electron transfer from the electron donor to the acceptor can be deactivated by back electron transfer. Grätzel and co-workers reported that this deactivation process can be suppressed using micelles as a reaction field.¹² In this system, C₁₄MV^{•+} generated by the photoinduced electron transfer from [Ru(bpy)₃]²⁺ (bpy = 2,2'-bipyridine) in its excited state to C₁₄MV²⁺ is incorporated into cetyltrimethylammonium chloride (CTAC) micelles, and the back electron transfer rate is ca. 200 times slower than that in the absence of CTAC because C₁₄MV^{•+} is separated from [Ru(bpy)₃]³⁺ (Fig. 1-9). This report has exhibited the usefulness of the micelles for a photoinduced electron transfer.

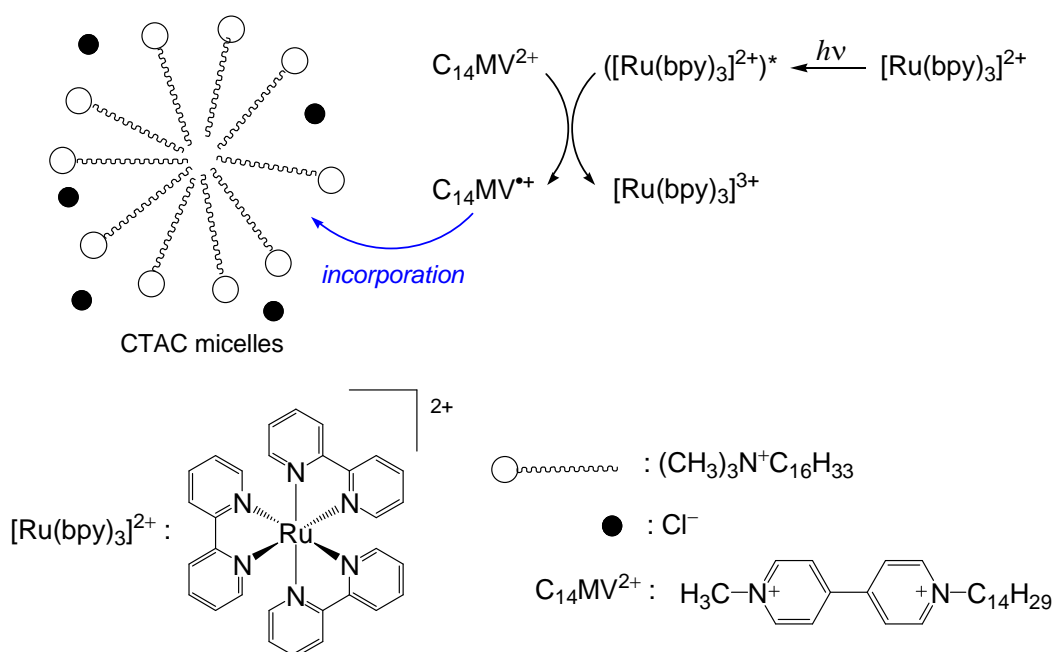


Figure 1-9. A schematic diagram of long-lived charge separation using micelles as a reaction field.¹²

However, in this system, the generated ion pair of one-electron oxidized species and reduced species is labile and can be deactivated by the back electron transfer between them. In addition, micelles have the small volume of hydrophobic field and the functional materials cannot be sufficiently incorporated.

Vesicles are an almost spherical bilayer membrane having an inner waterpool formed by self-organization of amphiphiles, such as phospholipids (Fig. 1-10). It is expected that the bilayer membrane works as a barrier to suppress a back electron transfer. If the electron transport across the membrane occurs, and oxidized species and reduced species are formed in an inner waterpool and the outer aqueous solution, respectively, the charge-separated state will have a long lifetime. For example, in 1979, Mangel and co-workers reported charge separation utilizing vesicles as a reaction field.¹³ In this system, chlorophyll as a sensitizer and β -carotene as an electron mediator are incorporated into the bilayer membrane of vesicles composed of egg-yolk phosphatidylcholine (EPC, Fig. 1-11). When the sensitizer was photoexcited, an electron was transported from ascorbate ion ($HAsc^-$, Fig. 1-11) in an inner waterpool to Fe^{3+} in

the outer aqueous solution. This system is the first example of a photoinduced electron transport across bilayer membranes. However, the Gibbs free-energy change for this reaction is negative. Hence, this system is not able to be regarded as a light energy-charge separation energy conversion system.

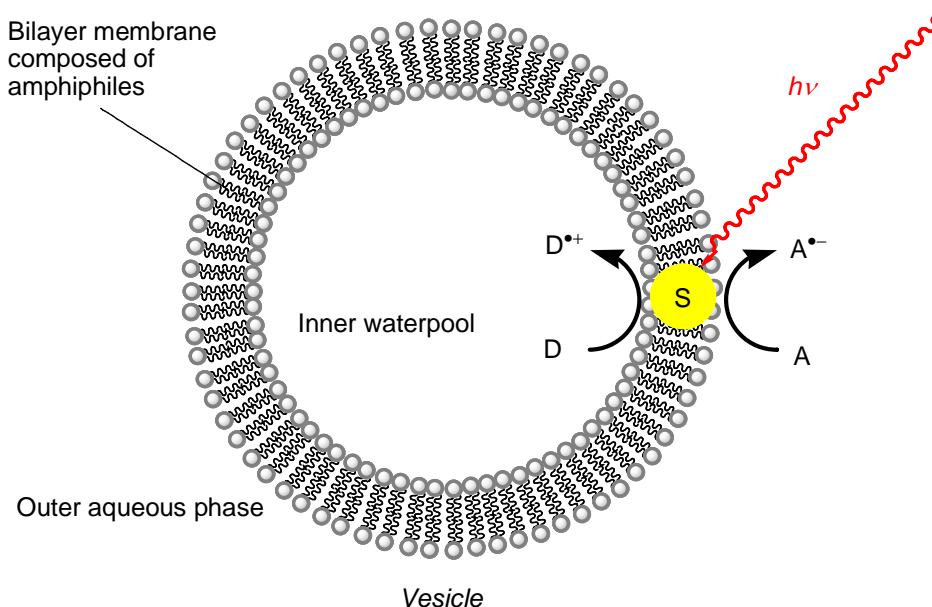


Figure 1-10. A schematic diagram of photoinduced charge separation in vesicle. S, D, and A represent a sensitizer, an electron donor, and an electron acceptor, respectively.

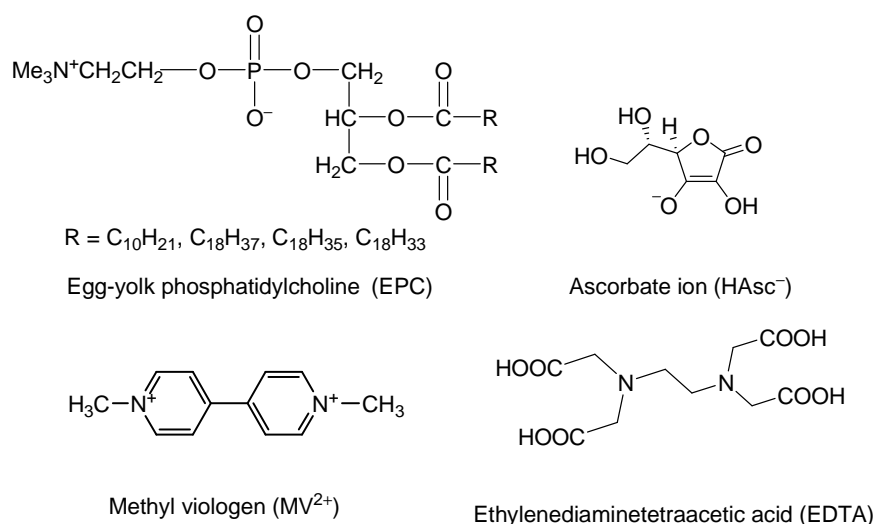


Figure 1-11. Chemical structures of egg-yolk phosphatidylcholine, ascorbate ion, methyl viologen, and ethylenediaminetetraacetic acid.

In 1979, Calvin *et al.* reported a photoinduced electron transport across vesicular bilayer membranes from ethylenediaminetetraacetic acid (EDTA) to methyl viologen (MV^{2+}) using the Ru complex ($RuC_{16}B^{2+}$, Fig. 1-12) as a sensitizer. The free-energy change in this reaction is positive. In this system, EDTA works as a sacrificial reagent, which decomposes irreversibly after the electron transfer as shown in Fig. 1-13, and the back electron transfer is efficiently suppressed by the use of sacrificial reagents because of their decomposition. In fact, this reaction can proceed without vesicles. In addition, it is questionable that the whole reaction is able to be regarded as a light-chemical energy conversion system because the decomposition of the sacrificial reagent is a highly exothermic reaction. On the contrary, Toda *et al.* have reported the electron transport system having positive free-energy change using a reversible electron donor, ascorbate ion ($HAsc^-$), as shown in Fig. 1-14.¹⁴ In this system, acridine orange (AOH^+) is employed as a water-soluble sensitizer. An electron is transferred from photoexcited AOH^+ to MV^{2+} to generate $MV^{\bullet+}$, then AOH^{2+} works as an electron mediator to oxidize $HAsc^-$ to $HAsc^{\bullet}$. These $HAsc^{\bullet}$ and $MV^{\bullet+}$ are generated in an inner waterpool and the outer aqueous phase, respectively, to produce the long-lived charge-separated state. The oxidized species of $HAsc^-$, $HAsc^{\bullet}$, is relatively stable and $HAsc^-$ does not decompose just after the oxidation, so that $HAsc^-$ can be employed as a reversible electron donor.

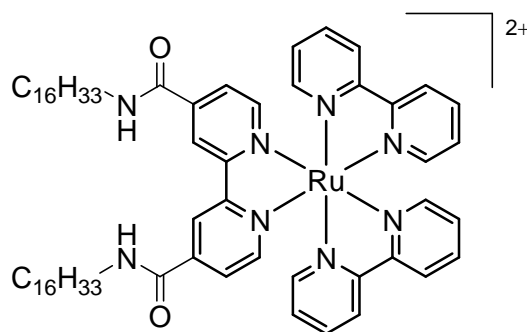


Figure 1-12. Chemical structure of $RuC_{16}B^{2+}$.

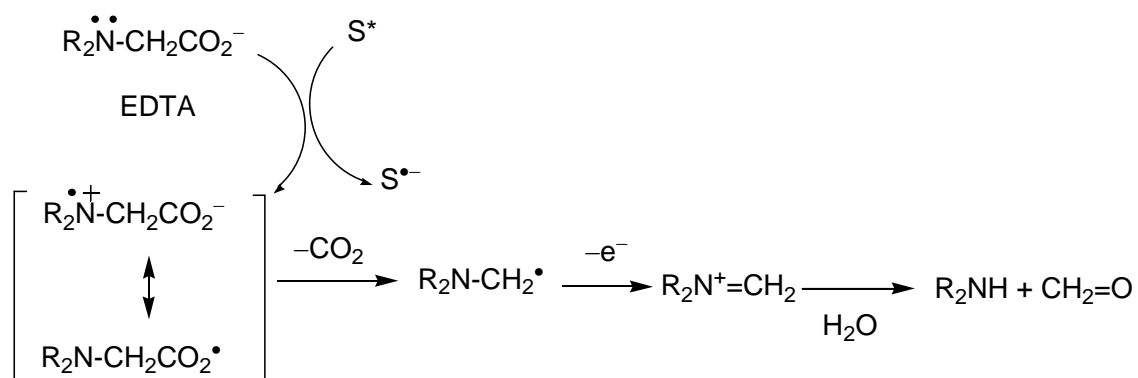


Figure 1-13. Irreversible decomposition process of one-electron oxidized species of EDTA; S represents a sensitizer.

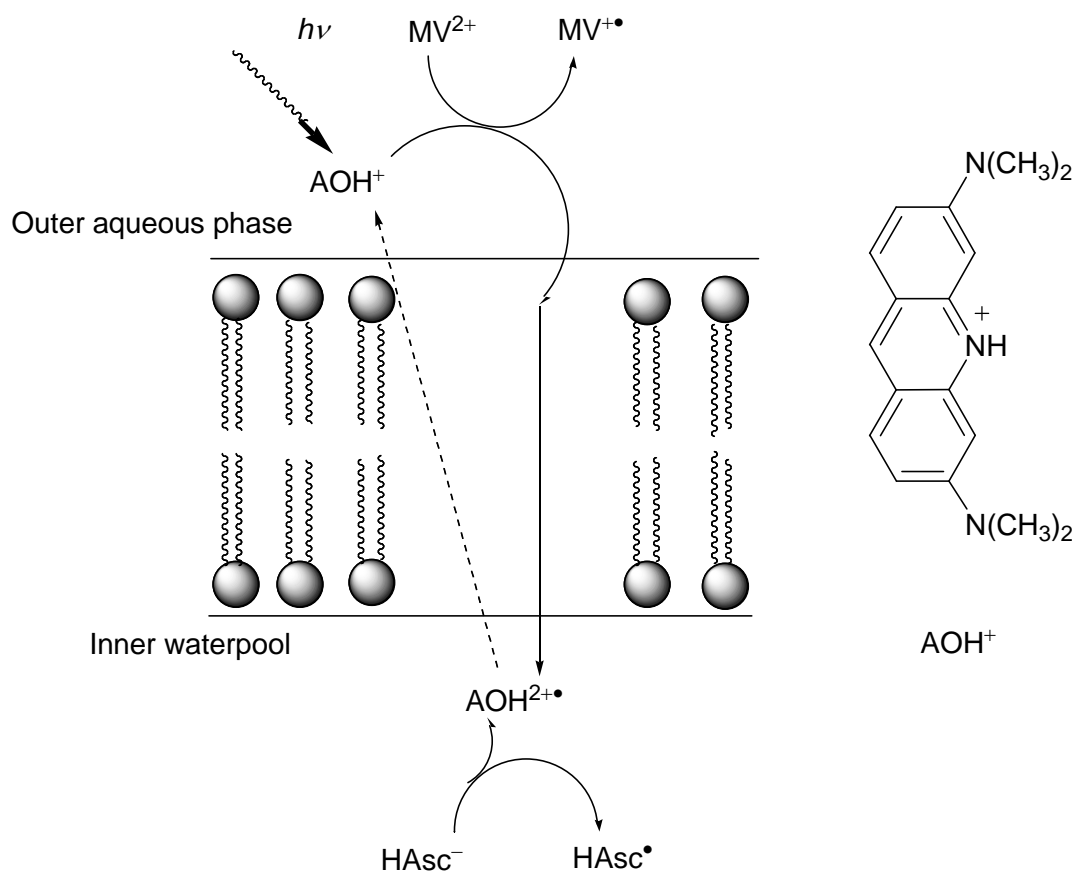


Figure 1-14. Photoinduced electron transport across the vesicle membrane reported by Toda *et al.*¹⁴

In our laboratory, photoinduced electron transport from HAsc^- in an inner waterpool to MV^{2+} in the outer aqueous solution has been achieved using pyrene derivatives having long-lived singlet excited state as a sensitizer, and the substituent effect of the sensitizers on the reaction efficiency has been investigated (Fig. 1-15).¹⁵ The free-energy change for the electron transport from HAsc^- to MV^{2+} is estimated to be $+12.7 \text{ kcal mol}^{-1}$. Although this system unfortunately cannot work using visible light, it appears to be one of the most faithful models of natural photosynthetic system in that an electron is transferred with the aid of light energy in the energetically uphill direction through the bilayer membrane.

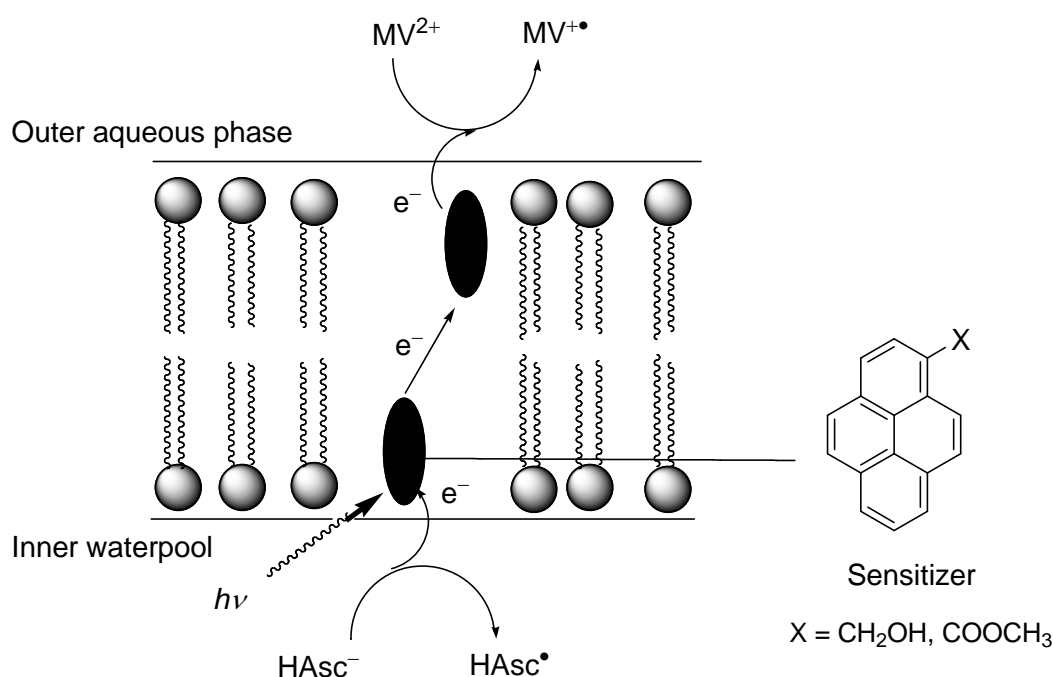


Figure 1-15. Photoinduced electron transport across the vesicle membrane sensitized by pyrene derivatives.¹⁵

1.2.3 Energy conversion

In the previous subsection, energy conversion systems, where light energy is converted into charge separation energy, were introduced. However, the charge-separated state is generally labile and its energy has to be converted into more stable chemical energy to achieve a meaningful system.

In such a point of view, material conversions driven by light energy have been intensively studied. Water splitting into hydrogen and oxygen molecules is one of the most attracting research fields because water is an abundant material, and hydrogen generated by water splitting is a clean energy source. Here, some examples related to the water splitting will be introduced.

Photocatalytic water splitting by inorganic semiconductor

It is known that charge separation as well as photocurrent is induced when titanium dioxide (TiO_2) is irradiated by UV light. By connecting with platinum electrode, hydrogen is generated on the Pt electrode and oxygen is generated on the TiO_2 electrode under photoirradiation. This epoch-making reaction is called “Honda-Fujishima effect”.¹⁶ The electronic state of TiO_2 is represented using a band structure composed of valence band, conduction band, and forbidden band (Fig. 1-16). An electron is excited from the valence band to the conduction band by photoirradiation, resulting in the formation of a hole and an electron, which work as an oxidant and a reductant to generate oxygen and hydrogen, respectively. However, this excitation can be induced only by photons having a higher energy than the bandgap between the valence band and the conduction band. In this reason, TiO_2 absorbs only UV light, hence, the investigation for the purpose of utilizing visible light, such as using semiconductors with a narrow bandgap or sensitizing dyes, and doping of typical elements, are ongoing.

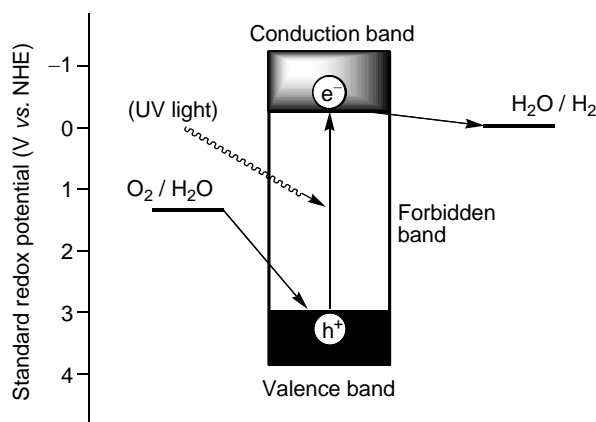


Figure 1-16. A band structure of TiO_2 and water splitting

Photochemical hydrogen production

In general photoinduced electron transfer systems, one electron is transferred per one photon although proton reduction to produce molecular hydrogen is a two-electron reductive process. Therefore, catalysts to enable multi-electron reduction by the stabilization of one-electron reduced species generated in the electron transfer reaction are necessary. In the natural photosynthetic system, ferredoxin-NADP⁺-reductase is participated in the catalytic reduction reaction.

In the photocatalytic water splitting system by inorganic semiconductors, the semiconductor works as both a sensitizer and a catalyst. On the other hand, for example, a photochemical hydrogen generation system using the combination of the sensitizer, colloidal Pt, and the electron mediator has been reported (Fig. 1-17).¹⁷ Although this system enables hydrogen evolution by the electron transfer from photochemically generated MV^{•+} to colloidal Pt, it requires EDTA as a sacrificial electron donor. This cannot be regarded as a light-chemical energy conversion system because EDTA is consumed stoichiometrically by the photochemical reaction. On the other hand, our laboratory has achieved hydrogen production using the photoinduced electron transport system across the vesicle membrane mentioned in the previous subsection catalyzed by colloidal Pt in the outer aqueous phase (Fig. 1-18)¹⁸ or Pt complexes embedded into vesicle membranes (Fig. 1-19)¹⁹. In these systems, HAsc[•] and MV^{•+} are separated by vesicle membranes so that the reversible electron donor HAsc⁻ can be employed for the photochemical hydrogen generation system.

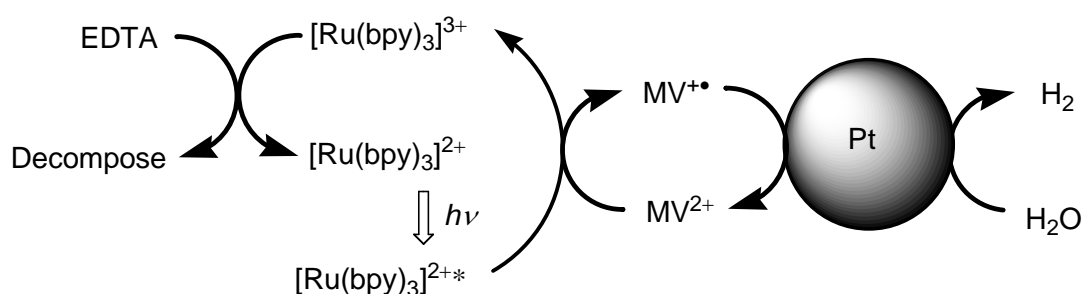


Figure 1-17. The reaction mechanism of photochemical hydrogen production using $[\text{Ru}(\text{bpy})_3]^{2+}$ as a sensitizer and colloidal Pt as a catalyst.¹⁷

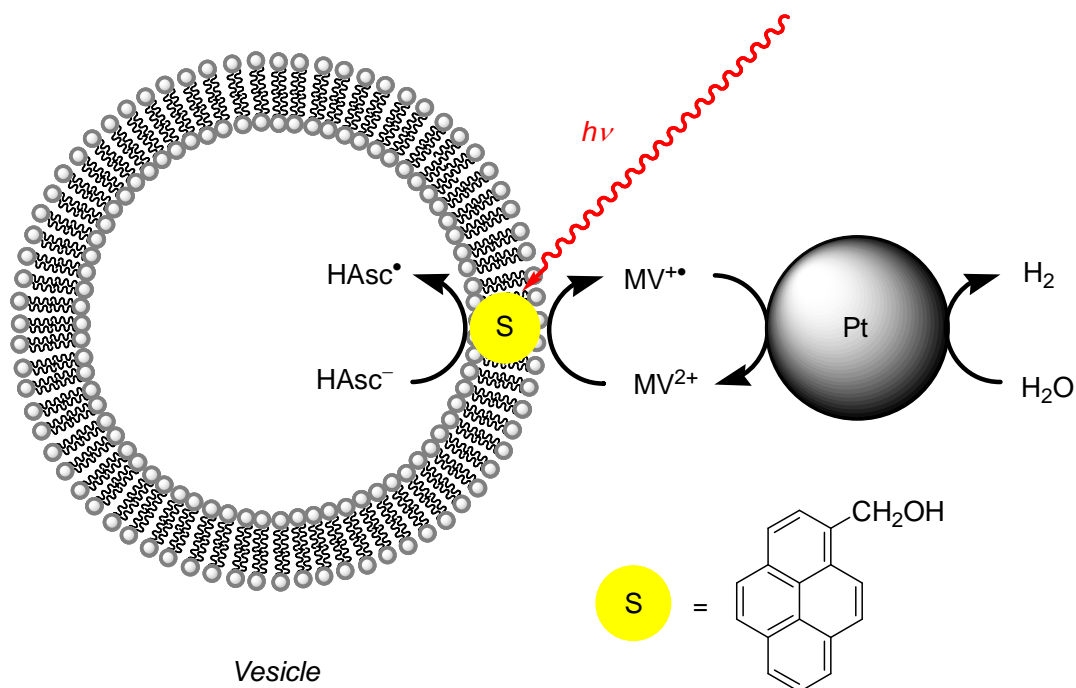


Figure 1-18. Photochemical hydrogen generation system utilizing the photoinduced electron transport system in vesicles catalyzed by the colloidal Pt.¹⁸

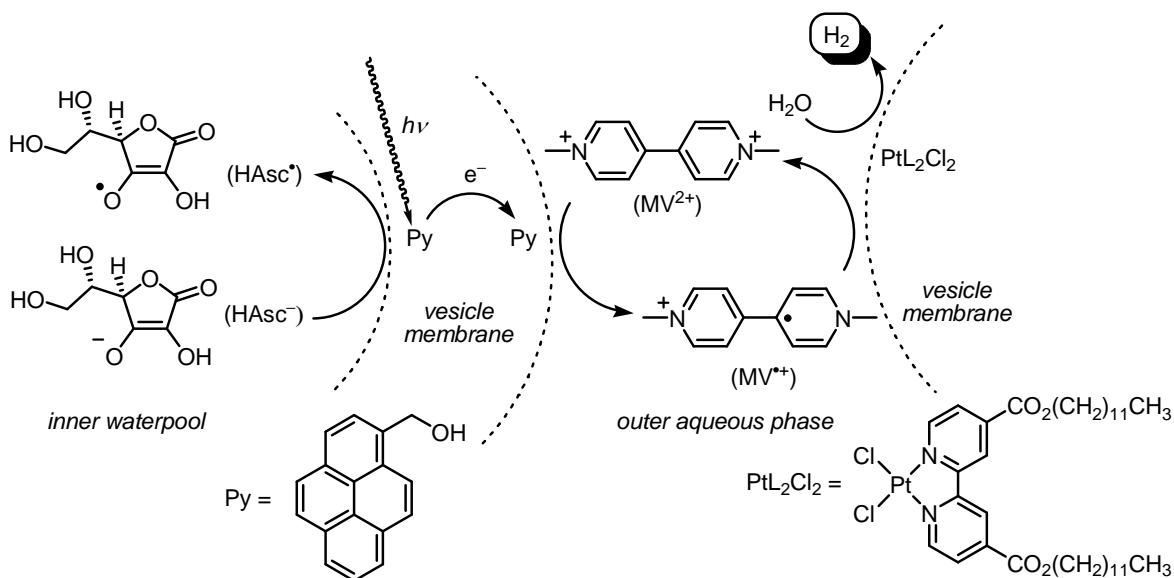


Figure 1-19. Photochemical hydrogen generation system utilizing the photoinduced electron transport system in vesicles catalyzed by Pt complexes embedded into vesicle membranes.¹⁹

Photochemical oxygen production

Molecular oxygen production by photochemical water oxidation has been reported using a Ru complexes as a catalyst (see §1.3.1). As a course of the research for achieving water splitting system, water oxidation catalyzed by a Ru complex embedded into vesicles has been reported just recently by König *et al* (Fig. 1-20).²⁰ In this system, a $[\text{Ru}(\text{bpy})_3]^{2+}$ derivative and a $\text{Ru}(\text{pda})(\text{py})_3$ (pda = pyridine-2,6-dicalyboxylate) derivative are incorporated into vesicle membranes as a sensitizer and a catalyst, respectively. When the sensitizer is photoexcited, an electron is transferred from the excited sensitizer to a sacrificial electron acceptor $\text{S}_2\text{O}_8^{2-}$ to produce a $[\text{Ru}(\text{bpy})_3]^{3+}$ derivative. This Ru(III) species then oxidizes the catalyst to initiate a catalytic cycle for water oxidation into molecular oxygen. This water oxidation system has been reported to be more efficient than the system in homogeneous solutions because of the enhanced intermolecular electron transfer between the sensitizer and the catalyst. However, the catalytic activity of the catalyst embedded into vesicle membranes is not yet clear to date and needs to be examined more deeply to know the reaction mechanism of the water oxidation system.

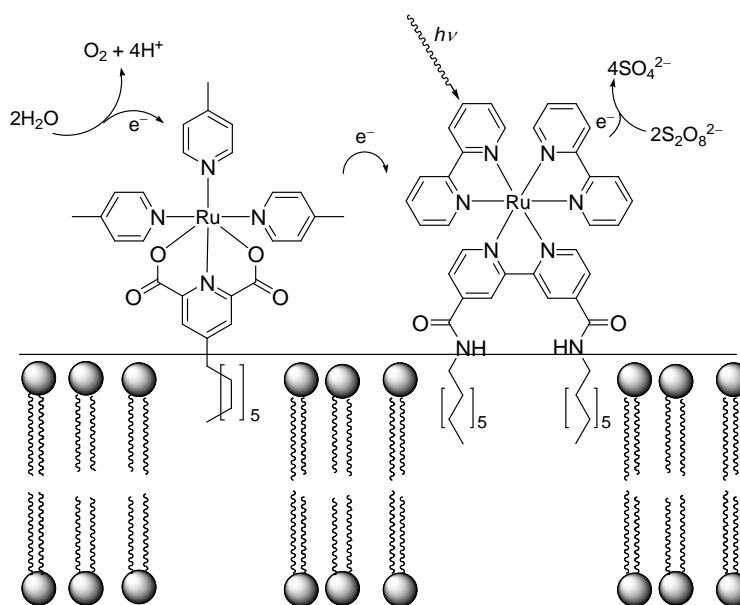
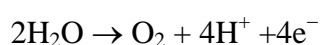
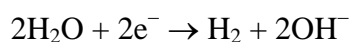


Figure 1-20. Photochemical water oxidation system using a sensitizer and a catalyst incorporated into vesicle membranes.²⁰

1.3 Water oxidation

As stated in §1.1.3, charge separation energy is fixed as chemical energy by redox reactions at each reaction terminal in natural photosynthetic system. Artificial light-chemical energy conversion systems have been intensively investigated, and water splitting reaction shown as the following formula is one of the most fascinating research fields.



Water reduction into molecular hydrogen is a two-electron reduction process, and various catalysts for water reduction have been reported so far. In our laboratory, as shown in the preceding section, photochemical reduction systems, such as hydrogen production by water reduction and CO generation by CO₂ reduction, have been achieved.^{19,21}

On the other hand, water oxidation into molecular oxygen is a four-electron oxidation reaction. Therefore, water oxidation is recognized to be relatively harder than water reduction. In natural photosynthetic system, an inorganic catalyst containing the Mn cluster in the photosystem II catalyzes the oxidation of water into molecular oxygen (see §1.1.3). Much effort has been made to achieve such a highly efficient water oxidation catalysis, and in recent years, it has been reported that transition metal complexes catalyze water oxidation reaction. Hence, I expect that the vesicular photochemical redox system such as water splitting into hydrogen and oxygen molecules can be constructed by the use of these metal complexes. In this section, some examples of metal complexes reported to act as water oxidation catalysts will be introduced.

1.3.1 Water oxidation catalyzed by ruthenium complexes

In 1982, the dimeric Ru complex [(bpy)₂(OH₂)Ru^{III}-O-Ru^{III}(OH₂)(bpy)₂]⁴⁺, which is so-called “blue dimer”, was reported by Meyer *et al.* as the first example of a water

oxidation catalyst (Fig. 1-21).²² Inspired by this report, researchers have devoted a lot of effort to explore efficient water oxidation catalysts, and various Ru complexes having catalytic activity toward water oxidation have been reported during the past several decades.²³ Among them, Ru(bda)(pyMe)₂ (bda = 2,2'-bipyridine-6,6'-dicarboxylate, pyMe = 4-methylpyridine) developed by Sun's group was epoch-making in large values of turnover number (TON) and turnover frequency (TOF) with respect to catalyst (Fig. 1-22, right). In the chemical water oxidation using Ce(NH₄)₂(NO₃)₆ (CAN) as an oxidant, the TON and TOF values of Ru(bda)(pyMe)₂ are 2000 and 41 s⁻¹,²⁴ while those of the blue dimer are only 13.2 and 0.0042 s⁻¹, respectively.^{25,26} A dinuclear Ru complex having bis(carboxylatopyridyl)phthalazine ligand has also been reported by Sun *et al.* (Fig. 1-22, left). This dinuclear complex exhibits a high TON of 10400, but the TOF is relatively low (TOF = 1.2 s⁻¹).²⁷

As described above, Ru(bda)(pyMe)₂ has high catalytic activity. Moreover, this complex can be prepared by the relatively facile procedure. In addition, it has been reported that the complex catalyzes not only chemical water oxidation using CAN as an oxidant but also photochemical water oxidation using [Ru(bpy)₃]²⁺ as a sensitizer.²⁸ Therefore, Ru(bda)(pyMe)₂ can be regarded as the most promising candidate for the investigation of the photochemical water oxidation in vesicles.

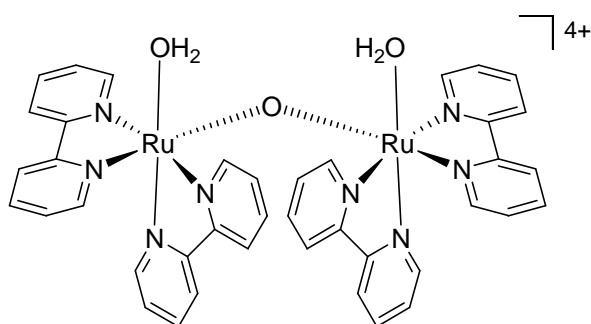


Figure 1-21. Chemical structure of the first water oxidation molecular Ru catalyst so-called “blue-dimer”, [(bpy)₂(OH₂)Ru^{III}-O-Ru^{III}(OH₂)(bpy)₂]⁴⁺.²²

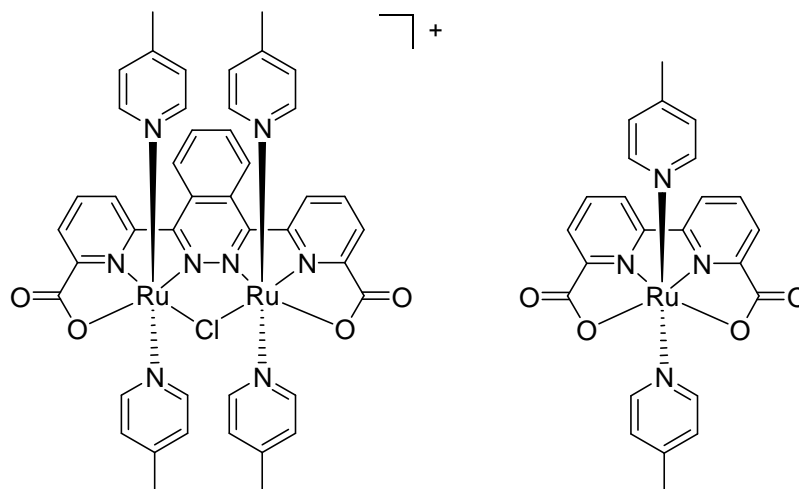


Figure 1-22. Chemical structures of the dinuclear and mononuclear Ru complexes reported to act as water oxidation catalysts.^{24,27}

1.3.2 Water oxidation catalyzed by iridium complexes

Ir complexes such as $[\text{Ir}(\text{ppy})_2(\text{OH}_2)]^+$ (ppy = 2-phenylpyridine) and $[\text{IrCp}^*(\text{dhbp})(\text{OH}_2)]^{2+}$ (Cp*H = 1,2,3,4,5-pentamethylcyclopentadiene, dhbp = 6,6'-dihydroxy-2,2'-bipyridine) have also been reported to catalyze water oxidation reaction (Fig. 1-23). The TON's of $[\text{Ir}(\text{ppy})_2(\text{OH}_2)]^+$ and $[\text{IrCp}^*(\text{dhbp})(\text{OH}_2)]^{2+}$ in the chemical water oxidation using CAN are 2490 and 6700,^{29,30} respectively, which are relatively high. However, the TOF's of these complexes are 0.0041 and 3.75 s^{-1} ,^{29,30} which are much lower compared to the Ru complex reported by Sun's group. Therefore, the investigation of Ir complexes capable of catalyzing water oxidation efficiently is still required.

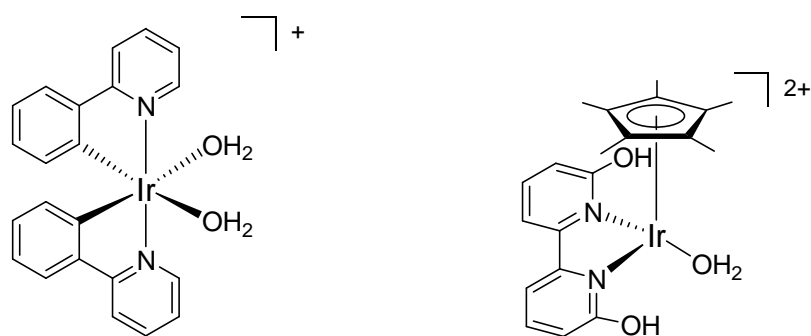


Figure 1-23. Chemical structures of Ir complexes reported to act as water oxidation catalysts.^{29,30}

1.3.3 Water oxidation catalyzed by other metal complexes

Complexes of other transition metals such as Mn, Fe, and Co have been reported to work as water oxidation catalysts (Fig. 1-24). These metals are earth-abundant, and as described in §1.1.3, it is known that the water oxidation in natural photosynthetic system is catalyzed by a Mn cluster.

The TON and TOF in the chemical water oxidation using CAN or $[\text{Ru}(\text{bpy})_3]^{3+}$ as an oxidant are reported to be 12 and 0.050 s^{-1} for the Mn complex,³¹ 360 and 0.23 s^{-1} for the Fe complex,³² 180 and 4.0 s^{-1} for the Co complex.³³ As shown above, the durability of these metal complexes in catalytic reaction is generally lower than that of Ru and Ir complexes.

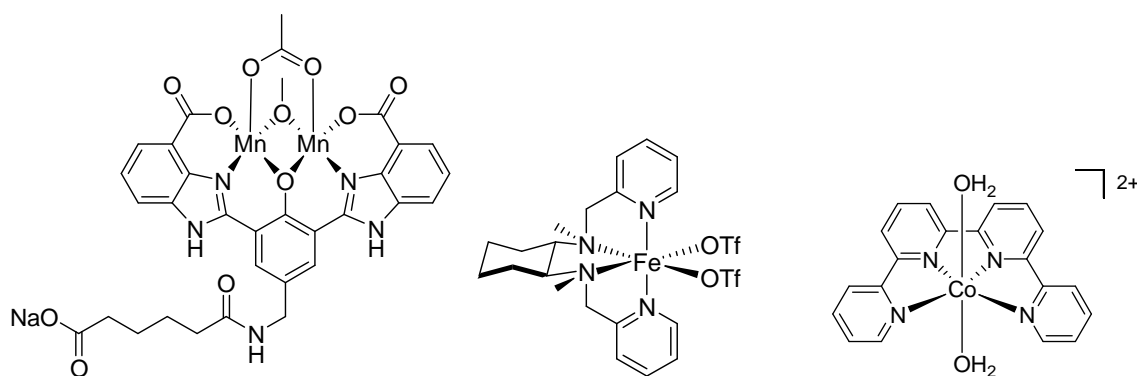


Figure 1-24. Chemical structures of metal complexes reported to act as water oxidation catalysts.^{31,32,33}

1.4 Overview of this thesis

The outline of natural photosynthetic system and some examples of artificially mimicked photosynthetic systems were introduced in this chapter. Artificial systems mimicking photosynthetic processes (i)–(iii) stated in §1.1 have been intensely reported. As a model of the photosynthetic system, vesicles are considered to be a useful reaction field for the efficient electron transport. However, photochemical water oxidation in vesicles has been scarcely reported and not completely examined yet. I have studied “construction of photochemical water oxidation system catalyzed by ruthenium complexes in vesicles” as my doctoral thesis with the aim of the construction of water splitting system in vesicles.

In Chapter 2, for the purpose of searching catalysts suitable for photochemical water oxidation system in vesicles, substituent effect of the Ru(bda)(pyR)₂ catalysts having different substituent groups at the 4-position of the axial pyridine ligands on the catalytic activity of the complex was investigated in a homogeneous solution.

In Chapter 3, based on the results obtained in Chapter 2, a novel amphiphilic Ru complex having a long alkyl chain connected by an ester bond was designed, and incorporation behavior as well as the catalytic activity of the complex in vesicles was investigated. In addition, to gain kinetic information about the vesicular photochemical water oxidation system, the dependence of the reaction rate on the concentrations of the sensitizer, the electron acceptor, and the catalyst was examined. On the basis of these kinetic data, the reaction mechanism was discussed.

Finally, the water oxidation system constructed in this study was evaluated, and the perspective of the water splitting system in vesicles was stated in Chapter 4.

References and Notes

1. B. Ke, *Photosynthesis*, Kluwer Academic Publishers, Doedrecht, 2001.
2. Mohr and Schopfer, *Plant Physiology (English translation of the 4th German edition of Pflanzenphysiologie)*, Springer, 1995.
3. G. McDermott; S. M. Prince; A. A. Freer; A. M. Hawthornthwaite-Lawless; M. Z. Papiz; R. J. Cogdell; N. W. Isaacs, *Nature*, **1995**, 374, 517.
4. T. Walz; R. Ghosh, *J. Mol. Biol.*, **1997**, 265, 107.
5. X. Hu; A. Damjanovic; T. Ritz; K. Schulten, *Proc. Nat. Acad., USA*, **1998**, 95, 5935.
6. J. Deisenhofer; Jr. Norris Eds. *The Photosynthetic Reaction Center*, Vol. II Academic Press, New York, **1993**.
7. K. Fukuyama; T. Okada; Y. Kakuta; Y. Takahashi, *J. Mol. Biol.*, **2002**, 315, 1155.
8. Y. Umena; K. Kawakami; J.-R. Shen; N. Kamiya, *Nature*, **2011**, 473, 55.
9. C. Devadoss; P. Bharathi; J. S. Moore, *J. Am. Chem. Soc.*, **1996**, 118, 9635.
10. C. N. Fleming; K.A. Maxwell; J. M. Desimone; T. J. Meyer; J. M. Papnikolas, *J. Am. Chem. Soc.*, **2001**, 123, 10336.
11. H. Imahori; D. M. Guldi; K. Tamaki; Y. Yoshida; C. Luo; Y. Sakata; S. Fukuzumi, *J. Am. Chem. Soc.*, **2001**, 123, 6617.
12. P. A. Brugger; M. Grätzel, *J. Am. Chem. Soc.*, **1980**, 102, 2461.
13. M. Mangel, *Biochem. Biophys. Acta*, **1979**, 430, 459.
14. A. Nakamura; R. Nishimura; K. Yoneyama; T. Umeda; F. Toda, *Nippon Kagaku Kaishi*, **1988**, 1208.
15. T. Mizushima; A. Yoshida; A. Harada; Y. Yoneda; T. Minatani; S. Murata, *Org. Biomol. Chem.*, **2006**, 4, 4336.
16. K. Honda; A. Fujishima, *Nature*, **1972**, 238, 37.
17. J. Kiwi; M. Grätzel, *J. Am. Chem. Soc.*, **1979**, 101, 7214.
18. K. Watanabe; K. Moriya; T. Kouyama; A. Onoda; T. Minatani; S. Takizawa; S. Murata, *J. Photochem. Photobiol. A: Chem.*, **2011**, 221, 113.
19. K. Watanabe; S. Takizawa; S. Murata, *Chem. Lett.*, **2011**, 40, 345.
20. M. Hansen; F. Li; L. Sun; B. König, *Chem. Sci.*, **2014**, 5, 2683.

21. N. Ikuta; S. Takizawa; S. Murata, *Photochem. Photobiol. Sci.*, **2014**, *13*, 691.
22. S. W. Gersten; G. J. Samuels; T. J. Meyer. *J. Am. Chem. Soc.*, **1982**, *104*, 4029.
23. M. K. Kärkäs; O. Verho; E. V. Johnston; B Åkermark, *Chem. Rev.*, **2014**, *114*, 11863.
24. L. Wang; L. Duan; B. Stewert; M. Pu; J. Liu; T. Privalov; L. Sun, *J. Am. Chem. Soc.*, **2012**, *134*, 18868.
25. J. P. Collin; J. P. Sauvage, *Inorg. Chem.*, **1986**, *25*, 135.
26. K. Nagoshi; S. Yamashita; M. Yagi; M. Kaneko, *J. Mol. Catal. A: Chem.*, **1999**, *144*, 71.
27. Y. Xu; A. Fischer; L. Duan; L. Tong; E. Gabrielsson; B. Åkermark; L. Sun, *Angew. Chem. Int. Ed.*, **2010**, *49*, 8934.
28. L. Duan; Y. Xu; P. Zhang; M. Wang; L. Sun, *Inorg. Chem.*, **2010**, *49*, 209.
29. N. D. McDaniel; F. J. Coughlin; L. L. Tinker; S. Bernhard, *J. Am. Chem. Soc.*, **2008**, *130*, 210.
30. A. Lewandowska-Andralojc; D. E. Polyansky; C.-H. Wang; W.-H. Wang; Y. Himeda; E. Fujita, *Phys. Chem. Chem. Phys.*, **2014**, *16*, 11976.
31. W. A. A. Arafa; M. D. Kärkäs B.-L. Lee; T. Åkermark; R.-Z. Liao; H.-M. Berends; J. Messinger; P. E. M. Siegbahn; B Åkermark, *Phys. Chem. Chem. Phys.*, **2014**, *16*, 11950.
32. J. L. Fillol; Z. Cordolá; I. Garcia-Bosch; L. Gómez; J. J. Pla; M. Costas, *Nat. Chem.*, **2011**, *3*, 807.
33. C.-F. Leung; S.-M. Ng; C.-C. Ko; W.-L. Man; J. Wu; L. Chen; T.-C. Lau, *Energy Environ. Sci.*, **2012**, *5*, 7903.

Chapter 2 Substituent Effect on Water Oxidation Catalyzed by Ruthenium Complexes

2.1 Introduction

Hydrogen generated by water splitting has been attracting much attention as a clean energy source. On the other hand, oxygen evolution by water oxidation is a big hurdle to achieving energy conversion utilizing water splitting to date. As stated in Chapter 1, photochemical water oxidation reaction catalyzed by metal complexes have been intensively studied in recent years. Among them, Ru(bda)(pyMe)₂ reported by Sun *et al.* is particularly attractive because of its synthetic facility and high catalytic efficiency in the photochemical water oxidation.¹ Therefore, this type of Ru complex is thought to be ideal for the investigation of the photochemical water oxidation in the vesicular system. Prior to the application in the vesicular system, I examined the substituent effect on the catalytic activity in the chemical and photochemical water oxidation reactions to find suitable structures for the vesicular water oxidation systems.

Sun and co-workers have reported that the photochemical water oxidation catalyzed by Ru(bda)(pyMe)₂ proceeds through the oxidative quenching of the photoexcited [Ru(bpy)₃]²⁺ by S₂O₈²⁻ to generate [Ru(bpy)₃]³⁺ and subsequent oxidation of the ruthenium catalyst by [Ru(bpy)₃]³⁺, leading to the oxidation of water into molecular oxygen.¹ Recently, they have also reported that Ru(bda)(pyR)₂ (pyR = pyridine having a substituent R at the 4-position) complexes catalyze water oxidation through the generation of Ru(IV)-O-O-Ru(IV) dimer from kinetic analysis using Ce(NH₄)₂(NO₃)₆ (CAN).² In this paper, the kinetic studies on the chemical water oxidation reaction catalyzed by Ru(bda)(pyR)₂ have been investigated, but those on the photochemical water oxidation have not been fully explored. Thus, I decided to investigate the water oxidation catalyzed by Ru(bda)(pyR)₂ systematically. In this chapter, I report the preparation and the catalytic activities in the chemical and photochemical water oxidation of a series of Ru(bda)(pyR)₂ (Fig. 2-1). In addition, the substituent effects on photophysical and electrochemical properties of these Ru complexes are also discussed.

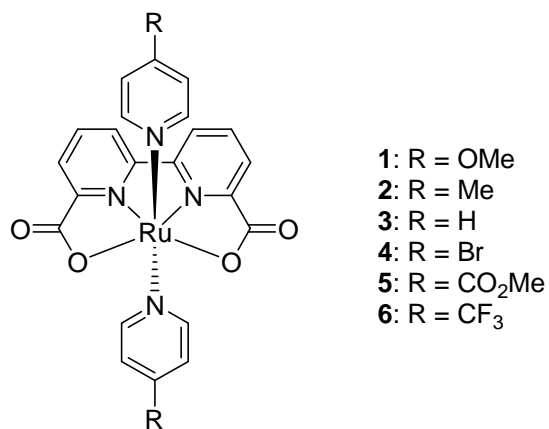


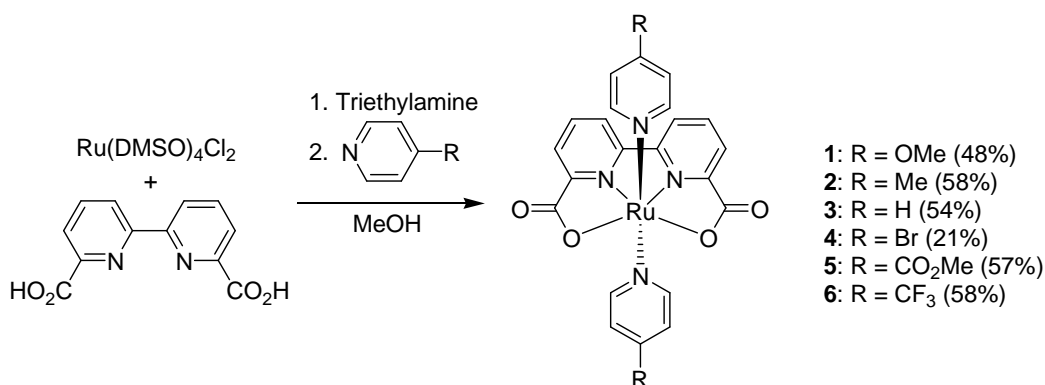
Figure 2-1. Chemical structure of Ru(bda)(pyR)₂ **1-6**.

2.2 Results and discussion

2.2.1 Synthesis

The known complexes **1–4** and **6** were prepared according to the literature procedure, as outlined in Scheme 2-1.^{3,4} The novel complex **5** was also synthesized in a similar manner. $\text{Ru}(\text{DMSO})_4\text{Cl}_2$ was prepared by heating RuCl_3 in DMSO containing small amounts of water. 2,2'-Bipyridine-6,6'-dicarboxylic acid (H_2bda) was prepared by oxidizing 6,6'-dimethyl-2,2'-bipyridyl by CrO_3 in conc. H_2SO_4 . $\text{Ru}(\text{bda})(\text{DMSO})_2$ was generated in situ by the reaction of $\text{Ru}(\text{DMSO})_4\text{Cl}_2$ and H_2bda in the presence of excess triethylamine in MeOH, and then the corresponding 4-substituted pyridine was added to give $\text{Ru}(\text{bda})(\text{pyR})_2$. Bromo-substituted complex **4** was synthesized using a mixture of 4-bromopyridine hydrochloride and excess triethylamine. Methoxycarbonyl-substituted complex **5** was synthesized using methyl isonicotinate that was prepared by the condensation of isonicotinic acid and methanol catalyzed by sulfuric acid. The formation of each complex was confirmed by ^1H NMR. In addition to the ^1H NMR spectrum, the structure of the novel complex **5** was confirmed by elemental analysis.

Scheme 2-1. Synthesis of complexes **1–6**.

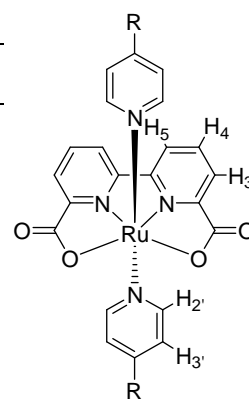


2.2.2 ¹H NMR spectroscopy

¹H NMR spectra of complexes **1–6** were measured in CDCl₃. The aromatic regions of their ¹H NMR spectra are shown in Fig. 2-2, and their chemical shifts are summarized in Table 2-1. For all the Ru complexes, signals due to the protons of the pyridine ligands and the bda ligand were observed. The change in the chemical shift by the substitution of the hydrogen atom at the 4-position of the pyridine ligands was found not only for the protons of the pyridine ligands, but also for those of the bda ligand. In the bda ligand, the chemical shift of H₄ changed most largely (from 7.65 ppm for **1** to 7.81 ppm for **6**). These results indicate that the electron-withdrawing substituents on the pyridine ligands reduce the electron density of the Ru center. This effect results in the enhanced σ-donation and/or the weakened π-back-donation of Ru–N bond between the Ru center and the bda ligand, reducing the electron density of the proton at *p*-position of the N atom, H₄, most largely. These NMR spectral changes imply that the substituent groups of the pyridine ligands affect the electronic nature not only of the pyridine ligands but also of the Ru center and the bda ligand.

Table 2-1. Chemical shifts δ (ppm) of the ¹H NMR signals of complexes Ru(bda)(pyR)₂ **1–6** in CDCl₃.

R	bda ligand			pyridine ligand		
	H ₃	H ₄	H ₅	H _{2'}	H _{3'}	R
OMe (1)	8.12	7.65	8.11	7.53	6.53	3.73
Me (2)	8.14	7.67	8.11	7.59	6.82	2.21
H (3)	8.18	7.71	8.12	7.80	7.03	7.49
Br (4)	8.18	7.74	8.15	7.60	7.20	–
CO ₂ Me (5)	8.24	7.78	8.12	7.79	7.57	3.89
CF ₃ (6)	8.26	7.81	8.16	8.06	7.28	–



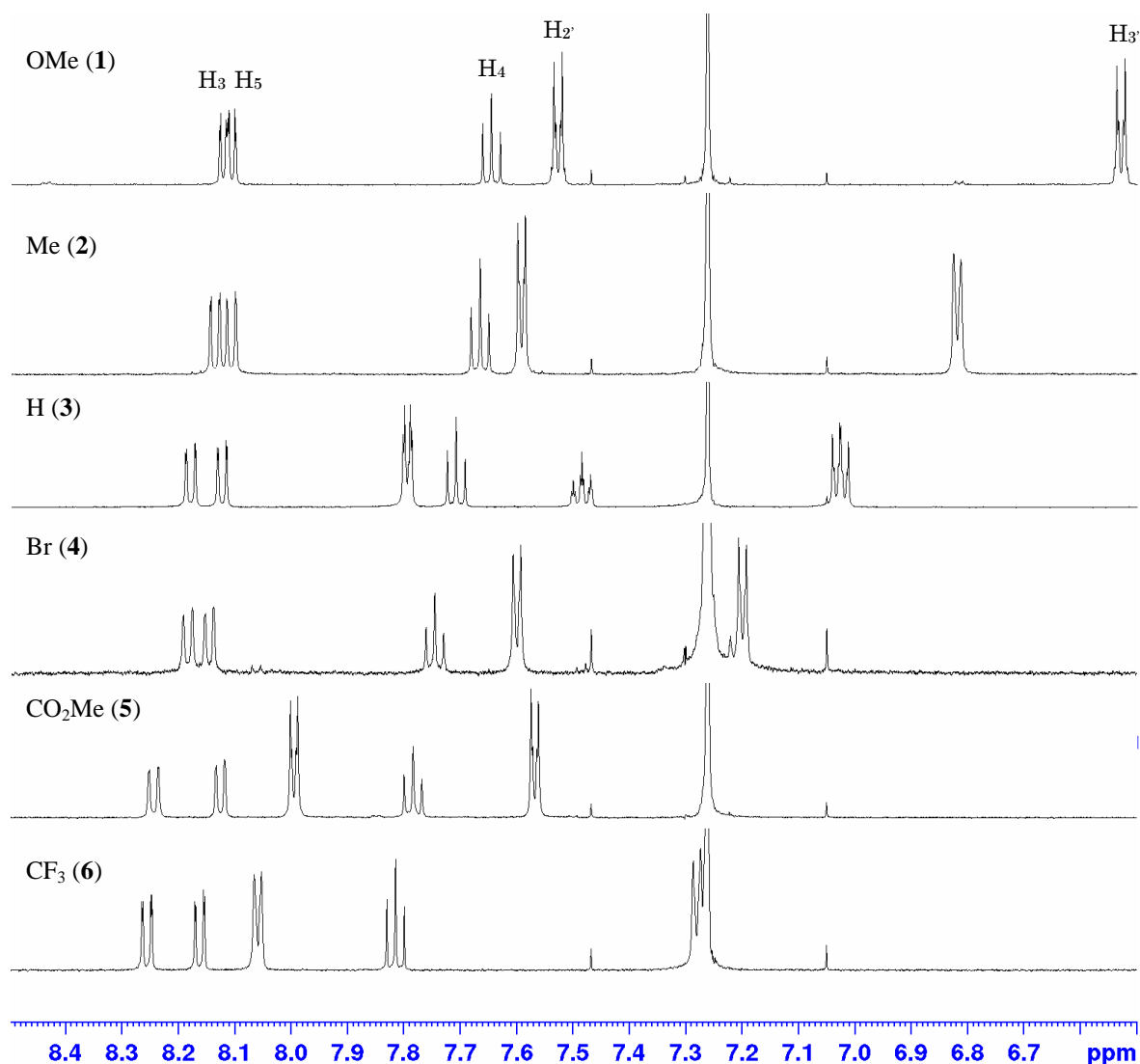


Figure 2-2. Aromatic region (δ 6.5–8.5 ppm) of the ^1H NMR spectra of complexes $\text{Ru}(\text{bda})(\text{pyR})_2$ **1–6** recorded in CDCl_3 .

2.2.3 Photophysical properties

UV-Vis absorption spectra of complexes **1–6** were measured in CHCl_3 and shown in Fig. 2-3. The absorption maximal wavelengths and the molar extinction coefficients are collected in Table 2-2. Each complex exhibits mainly three absorption peaks: small peaks or shoulders around 550 nm, relatively large peaks in 350–460 nm, and sharp peaks around 300 nm. The peaks observed in 350–460 nm are red-shifted by the introduction of the electron-withdrawing groups (from 347 nm for $\text{R} = \text{OMe}$ (**1**) to 462 nm for $\text{R} = \text{CO}_2\text{Me}$ (**5**)). In addition, peaks around 420 nm are also observed for complexes **1** and **2**.

It has been reported that Ru(pda)(pyH)₃ (pda = pyridine-2,6-dicarboxylate, pyH = pyridine) has two absorption bands at 390 nm and 450 nm, which are assigned to the metal-to-ligand charge-transfer (MLCT) transition from the Ru d orbital to the π* orbital of the pyridine ligands and the MLCT transition from the Ru d orbital to the π* orbital of the pdc ligand, respectively.⁵ It is also known that [Ru(bpy)₃]²⁺ has a sharp absorption peak at 285 nm and a broad peak at 452 nm, which originate from ligand-centered (LC) transition of bpy π-π* and MLCT transition from the Ru d orbital to the bpy π* orbital.⁶ Therefore, I consider that three main peaks of complexes **1–6** around 550 nm, 350–460 nm, and 300 nm can be assigned to MLCT(Ru d→bpy π*), MLCT(Ru d→py π*), and LC(bpy π→π*) transitions, respectively. Peaks at 420 nm observed for complexes **1** and **2** are tentatively ascribed to high-energy MLCT(Ru d→bpy π*) transition. These assignments for MLCT absorption bands were supported by DFT calculations (see §2.2.5). All the complexes showed no photoluminescence in CHCl₃.

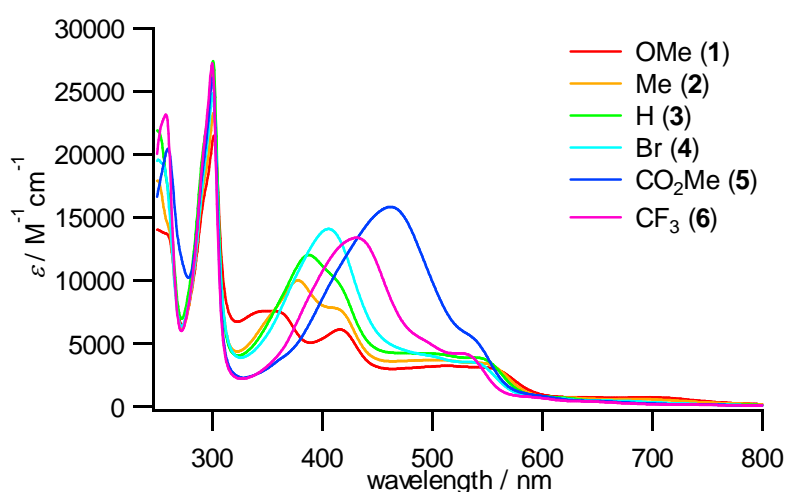


Figure 2-3. UV-Vis absorption spectra of complexes Ru(bda)(pyR)₂ **1–6** in CHCl₃

Table 2-2. Absorption properties of complexes Ru(bda)(pyR)₂ **1–6**.

R	$\lambda_{\text{abs}}^a / \text{nm}$ ($\epsilon_{\text{max}} / 10^3 \text{ M}^{-1} \text{ cm}^{-1}$)
OMe (1)	302 (21.5), 347 (7.55), 353 (7.55), 417 (6.09), 514 (3.21), 557sh (2.97)
Me (2)	302 (23.2), 378 (9.99), 416sh (7.67), 506 (3.69), 554sh (3.27)
H (3)	301 (27.6), 388 (12.0), 505sh (4.16), 546sh (3.76)
Br (4)	301 (24.8), 406 (14.1), 501sh (3.97), 541sh (3.45)
CO ₂ Me (5)	301 (26.1), 462 (15.8), 540sh (5.20)
CF ₃ (6)	300 (27.2), 431 (13.4), 525 (4.21)

^aWavelengths of absorption maxima recorded in CHCl₃.

2.2.4 Cyclic voltammetric measurement

Electrochemical properties of Ru complexes **1–6** were examined by cyclic voltammetry in CH₂Cl₂ degassed by N₂-bubbling. The results of oxidative sweeps are shown in Fig. 2-4, and the oxidation potentials are summarized in Table 2-3. Each Ru complex exhibited a reversible oxidation wave, which is attributable to the oxidation of the Ru center (Ru^{III/II} redox couple).^{1,2} Electron-withdrawing groups on the pyridine ligands induced a positive shift of the oxidation potential (from –0.09 V (vs. Fc⁺/Fc) for R = OMe (**1**) to 0.08 V for R = CF₃ (**6**)). Hence, it is indicated that the HOMO, which is localized to the Ru center (see §2.2.5), is inductively stabilized by the electron-withdrawing nature of the substituent groups on the pyridine ligands. These shifts of the oxidation potentials suggest that the catalytic behaviors of the complexes would be also affected by the substituent groups of the pyridine ligands. On the other hand, no obvious reduction waves were observed in reductive sweeps of 0 ~ –2.5 V region.

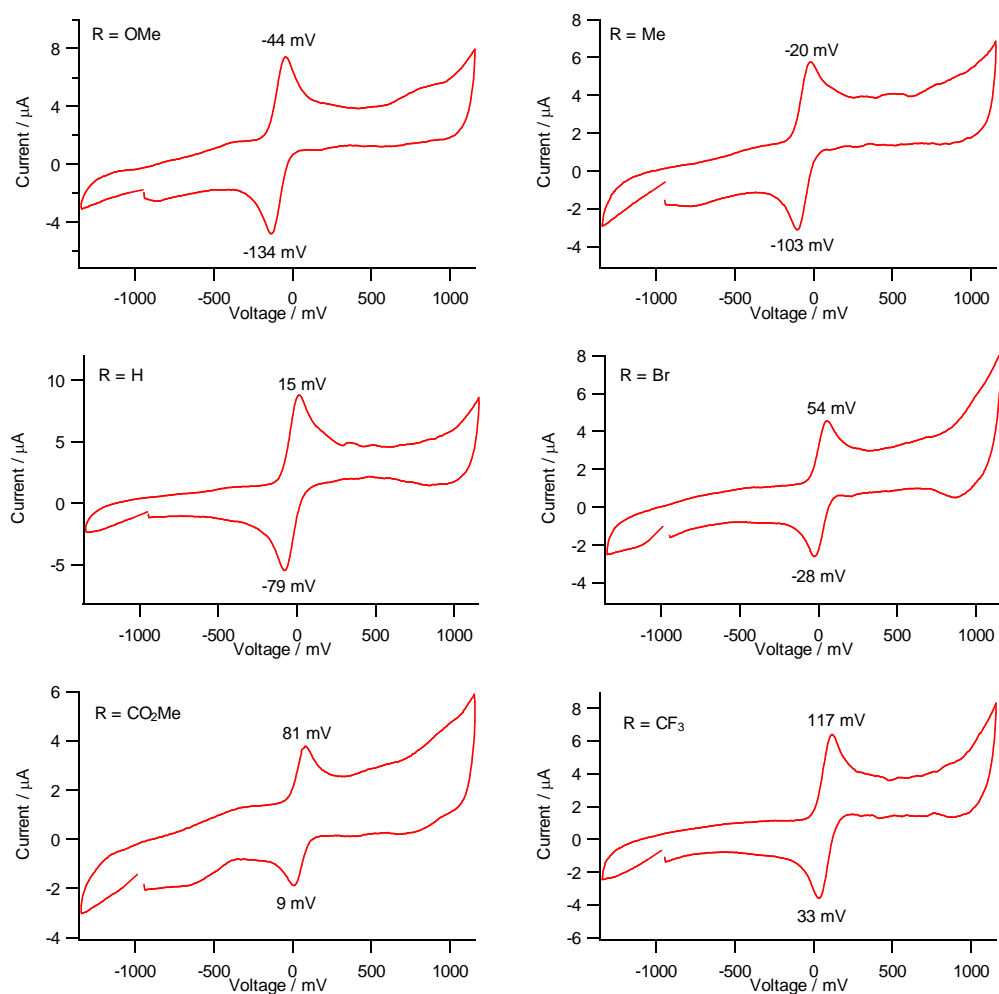


Figure 2-4. Cyclic voltammogram of complexes Ru(bda)(pyR)₂ **1–6** (vs. Fc⁺/Fc).

Table 2-3. Oxidation potentials of complexes Ru(bda)(pyR)₂ **1–6** in CH₂Cl₂

R	$E_{1/2(\text{oxdn})} / \text{V}^a$
OMe (1)	-0.09
Me (2)	-0.06
H (3)	-0.03
Br (4)	0.01
CO ₂ Me (5)	0.05
CF ₃ (6)	0.08

^avs. Fc⁺/Fc

2.2.5 Theoretical calculation

DFT calculations for complexes **1–6** were performed at the B3LYP level using the 6-31G basis set on C, H, N, O, F and Br atoms, and the LANL2DZ basis set on Ru atom. The energy levels of molecular orbitals (MOs) calculated for complexes **1–6** are summarized in Fig. 2-5 and Table 2-4. As shown in Fig. 2-5, all the Ru complexes have MOs localized to the Ru d orbital, bpy π^* orbital, and py π^* orbital, which are depicted by bold black, blue, and red lines, respectively, in the figure. The energy level of py π^* orbital is largely lowered by the electron-withdrawing groups, while the stabilization of the Ru d orbital and bpy π^* orbital are relatively small. The py π^* orbital of complex **5** is stabilized rather more largely than expected from the electron-withdrawing ability of the substituent group. This is because the π^* orbital of the pyridine ligands is delocalized to the carbonyl π orbital in **5**.

The oxidation potentials of complexes **1–6** stated in §2.2.3 are plotted against the energy levels of HOMO in Fig. 2-6. From this figure, one can see that the oxidation potential of complexes **1–6** has an approximately negative relationship with the energy level of HOMO, which is localized to the Ru center. Therefore, it should be concluded that the electronic nature of the Ru center is affected by the substituent groups on the pyridine ligands. The energy levels and distributions of MOs for complexes **1–6** are illustrated individually in Figs. 2-7 ~ 2-12.

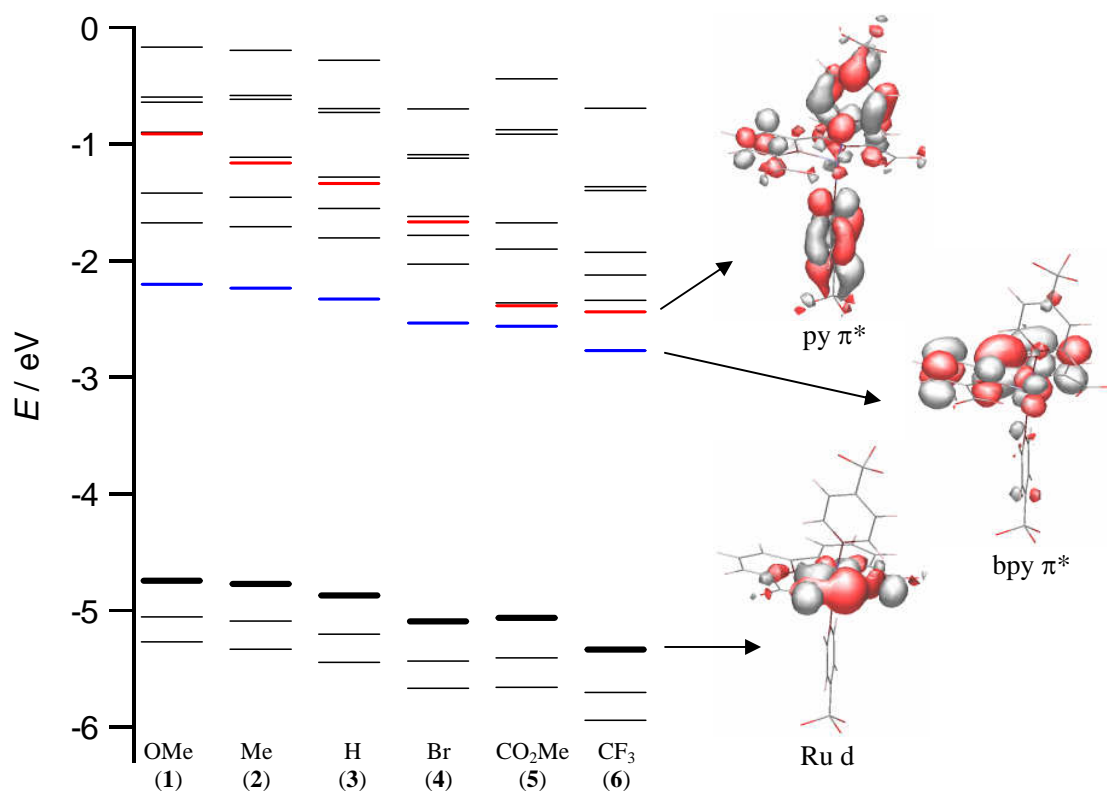
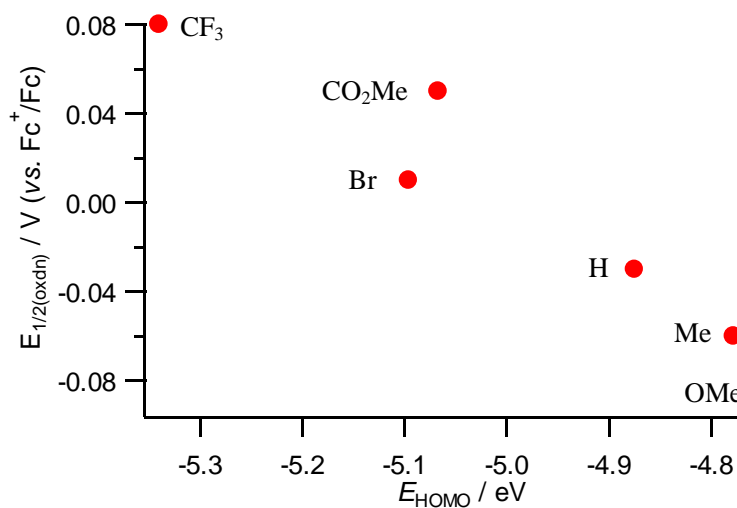


Figure 2-5. Schematic diagram showing the MO energy levels of complexes **1-6** from DFT calculations (B3LYP, 6-31G basis set on C, H, N, O, F, Br atoms; LANL2DZ basis set on Ru atom): MOs localized to d orbital of Ru center, bold black; π^* orbital of bipyridine ligand, bold blue; π^* orbital of pyridine ligands, bold red.

Table 2-4. Frontier orbital energies (eV) of complexes **1–6** from DFT calculations^a

	OMe (1)	Me (2)	H (3)	Br (4)	CO ₂ Me (5)	CF ₃ (6)
LUMO+6	-0.5990	-0.5864	-0.6982	-1.0925	-0.8798	-1.3670
LUMO+5	-0.6411	-0.6169	-0.7300	-1.1253	-0.9157	-1.4025
LUMO+4	-0.8995	-1.1173	-1.2850	-1.6223	-1.6772	-1.9313
LUMO+3	-0.9143	-1.1639	-1.3395	-1.6697	-1.9031	-2.1250
LUMO+2	-1.4232	-1.4577	-1.5542	-1.7848	-2.3663	-2.3427
LUMO+1	-1.6791	-1.7112	-1.8071	-2.0326	-2.3897	-2.4410
LUMO	-2.2065	-2.2382	-2.3300	-2.5367	-2.5667	-2.7744
HOMO	-4.7476	-4.7777	-4.8747	-5.0963	-5.0671	-5.3395
HOMO-1	-5.0608	-5.0939	-5.2055	-5.4389	-5.4119	-5.7077
HOMO-2	-5.2722	-5.3363	-5.4481	-5.6730	-5.6616	-5.9460

^aB3LYP, 6-31G basis set on C, H, N, O, F, Br atoms; LANL2DZ basis set on Ru atom.

**Figure 2-6.** Plots of $E_{1/2(\text{oxdn})}$ of complexes **1–6** against the HOMO energy level estimated from DFT calculations, E_{HOMO} .

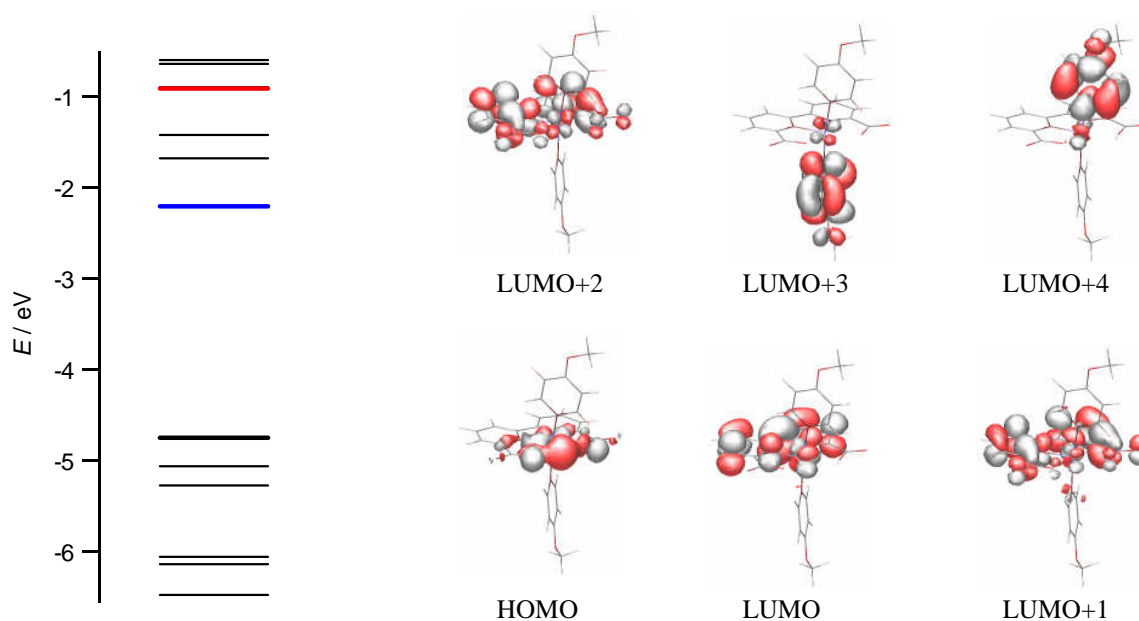


Figure 2-7. Schematic diagram showing the MO distributions and the MO energy levels of complex Ru(bda)(pyOMe)₂ (**1**) from DFT calculation (B3LYP, 6-31G basis set on C, H, N, O atoms; LANL2DZ basis set on Ru atom)

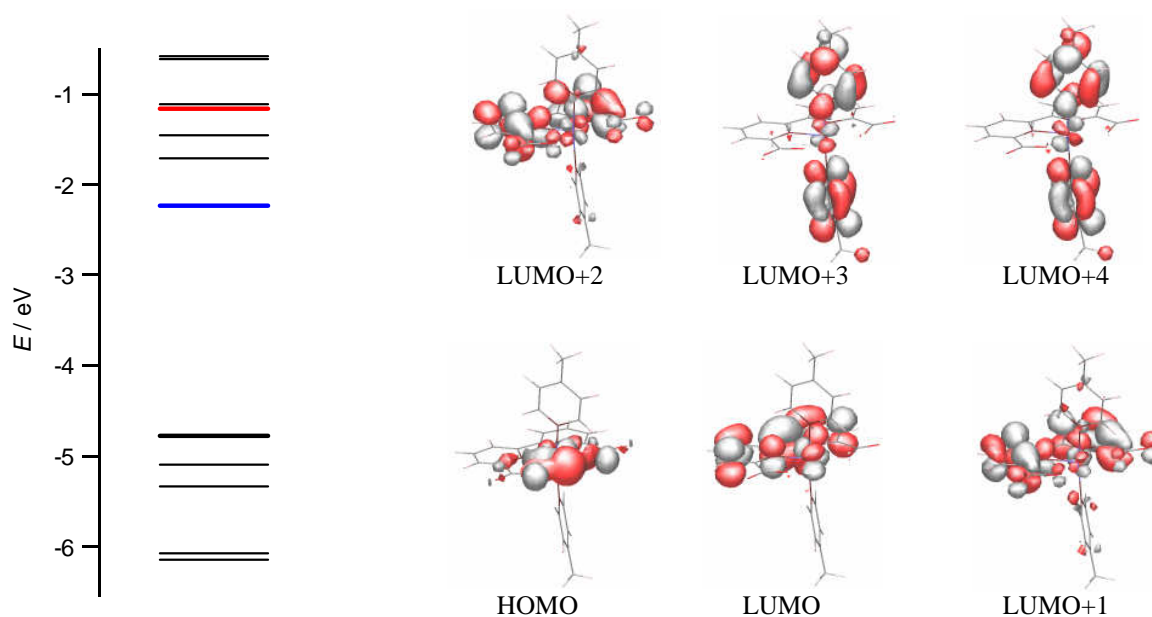


Figure 2-8. Schematic diagram showing the MO distributions and the MO energy levels of complex Ru(bda)(pyMe)₂ (**2**) from DFT calculation (B3LYP, 6-31G basis set on C, H, N, O atoms; LANL2DZ basis set on Ru atom)

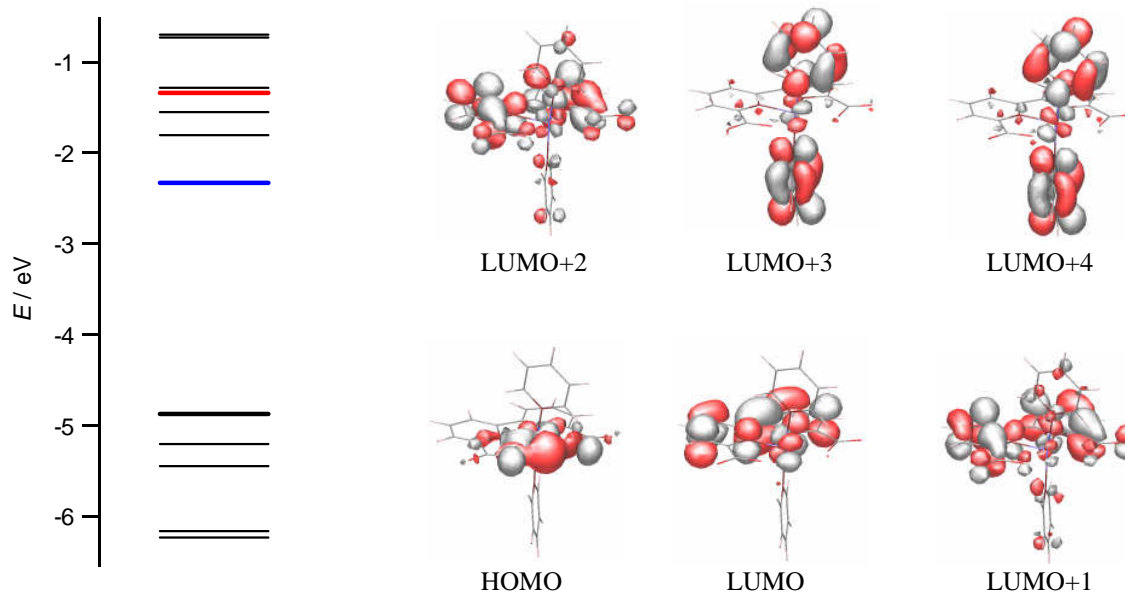


Figure 2-9. Schematic diagram showing the MO distributions and the MO energy levels of complex Ru(bda)(pyH)₂ (**3**) from DFT calculation (B3LYP, 6-31G basis set on C, H, N, O atoms; LANL2DZ basis set on Ru atom)

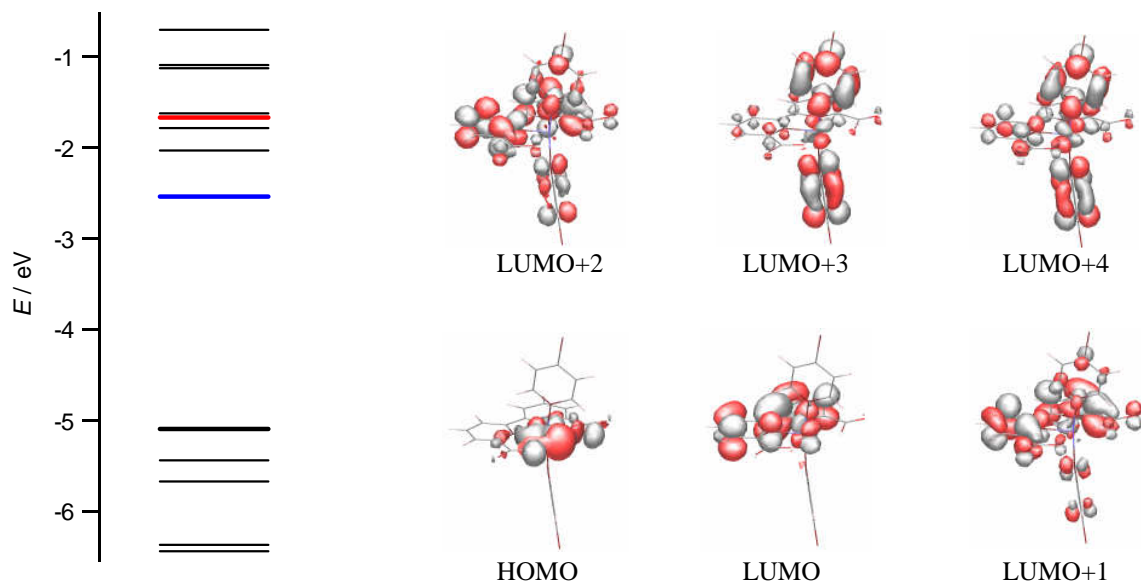


Figure 2-10. Schematic diagram showing the MO distributions and the MO energy levels of complex Ru(bda)(pyBr)₂ (**4**) from DFT calculation (B3LYP, 6-31G basis set on C, H, N, O, Br atoms; LANL2DZ basis set on Ru atom)

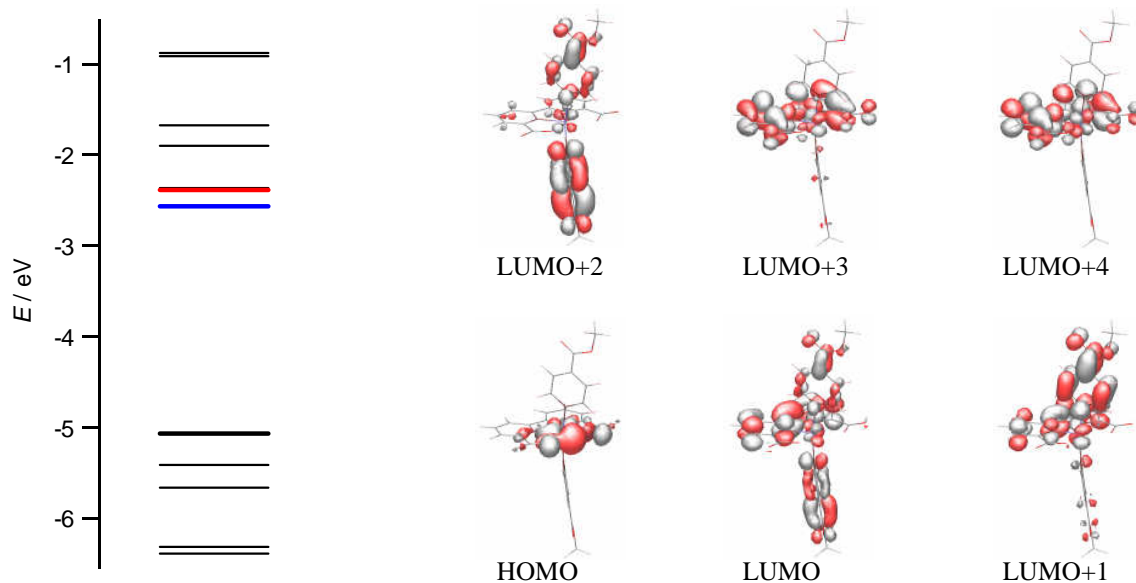


Figure 2-11. Schematic diagram showing the MO distributions and the MO energy levels of complex $\text{Ru}(\text{bda})(\text{pyCO}_2\text{Me})_2$ (**5**) from DFT calculation (B3LYP, 6-31G basis set on C, H, N, O atoms; LANL2DZ basis set on Ru atom)

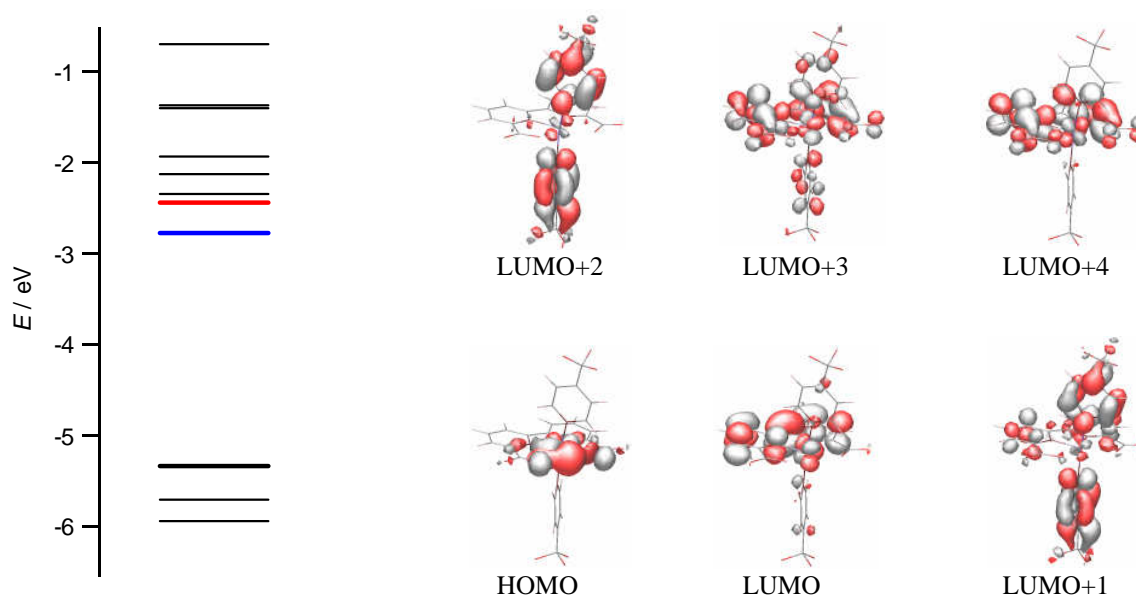


Figure 2-12. Schematic diagram showing the MO distributions and the MO energy levels of complex $\text{Ru}(\text{bda})(\text{pyCF}_3)_2$ (**6**) from DFT calculation (B3LYP, 6-31G basis set on C, H, N, O, F atoms; LANL2DZ basis set on Ru atom)

As mentioned in §2.2.3, in the UV-Vis absorption spectra, small bands around 550 nm and relatively large peaks from 350 nm to 460 nm were observed (Fig. 2-13). Since the LUMO of the complex corresponds to the bpy π^* orbital (see Fig. 2-5), the absorption peaks at the longer wavelengths are thought to be derived from the MLCT(Ru d \rightarrow bpy π^*) transitions. The absorption maxima of these peaks are almost constant. Similarly, the calculated energy gaps between Ru d and bpy π^* are also almost constant as shown as blue circles in Fig. 2-14. On the other hand, the peaks from 350 to 460 nm can be assigned to MLCT(Ru d \rightarrow py π^*) transition because the π^* orbital of the pyridine ligands is observed as LUMO+3 for complexes **1–4** or LUMO+1 for complexes **5** and **6** in Fig. 2-5. The energy level of py π^* orbital is largely stabilized by the electron-withdrawing groups (from -0.9143 eV for **1** to -2.4410 eV for **6**), while stabilization of the Ru d orbital (HOMO) is relatively small (from -4.7476 eV for **1** to -5.3395 eV for **6**). Therefore, the energy gap between Ru d and py π^* is narrowed by the electron-withdrawing groups and the absorption maximum is red-shifted. The plots of the transition energy estimated from the absorption maximum wavelength in 350–460 nm region vs. the calculated energy gap between HOMO and the unoccupied MO localized to py π^* orbital are shown in Fig. 2-14 (red triangles), demonstrating that the observed and calculated transition energies have a positive correlation. In addition, the peaks around 420 nm, which were observed for complexes **1** and **2**, are assigned to high-energy MLCT(Ru d \rightarrow bpy π^*) transition. This is because the bpy π^* orbital is observed as LUMO+1 and LUMO+2 for complexes **1** and **2**, whose energy levels are lower than that of the py π^* orbital (LUMO+3), and the energy levels of these orbitals are not largely shifted by the electron-withdrawing nature of the substituent groups.

Thus, the DFT calculations present strong evidence supporting the assignment of UV-Vis absorption bands discussed in §2.2.3. The assignments of the three MLCT bands are summarized graphically in Fig. 2-13.

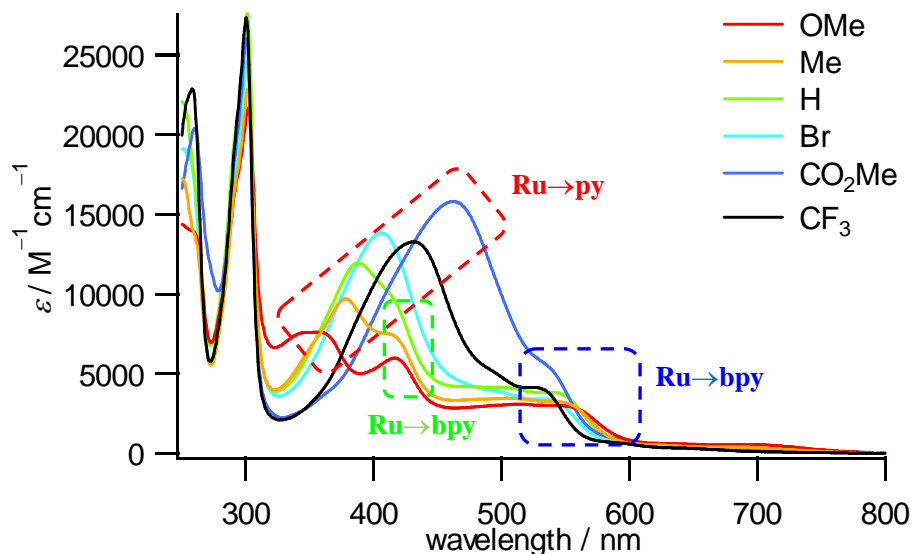


Figure 2-13. UV-Vis absorption spectra of complexes Ru(bda)(pyR)₂ **1–6** recorded in CHCl₃ and the assignment of each absorption peak.

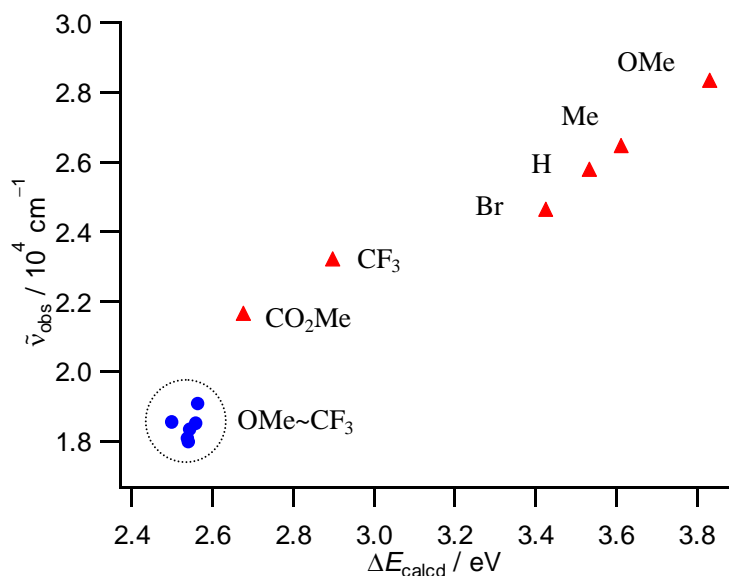


Figure 2-14. Transition energy estimated from the absorption spectra of complexes Ru(bda)(pyR)₂ **1–6** recorded in CHCl₃ as a function of the energy gap between HOMO and unoccupied MO from DFT calculation (B3LYP, 6-31G basis set on C, H, N, O, F, Br atoms; LANL2DZ basis set on Ru atom). Blue full circles: MLCT bands from Ru d orbital to bpy π* orbital. Red full triangles: MLCT bands from Ru d orbital to py π* orbital.

2.2.6 Chemical water oxidation

Chemical water oxidation experiments catalyzed by Ru complexes **1–6** were carried out as follows: 100 μL of the solution of **1–6** (30 μM) in acetonitrile was added to 2.9 mL of $\text{Ce}(\text{NH}_4)_2(\text{NO}_3)_6$ (CAN) solution (1.5 mM) in 0.1 M aqueous nitric acid. After addition of the catalyst solution, UV-Vis absorption spectral change was measured. Since CAN has a broad absorption band in UV region as shown in Fig. 2-15, the consumption of CAN is able to be monitored in the decrease of the absorption intensity.² The time profiles of the decrease in the absorbance at 360 nm after addition of the catalyst **1–6** are shown in Fig. 2-16. This decay curve was fitted by a single exponential function, and the initial consumption rate of CAN, v_i , was calculated, and listed in Table 2-5. After the reaction, the gas phase of reaction vessel was analyzed by gas chromatography and the generation of O_2 was also confirmed.

In Table 2-5, it is found that electron-withdrawing Br, CO_2Me and CF_3 groups particularly increase the catalytic efficiency of the complex. On the other hand, complex **1** (R = OMe) has relatively higher catalytic activity than complexes **2** (R = Me) and **3** (R = H), indicating that the overall reaction rate does not completely have a positive correlation with the electron-withdrawing ability of the substituent groups.

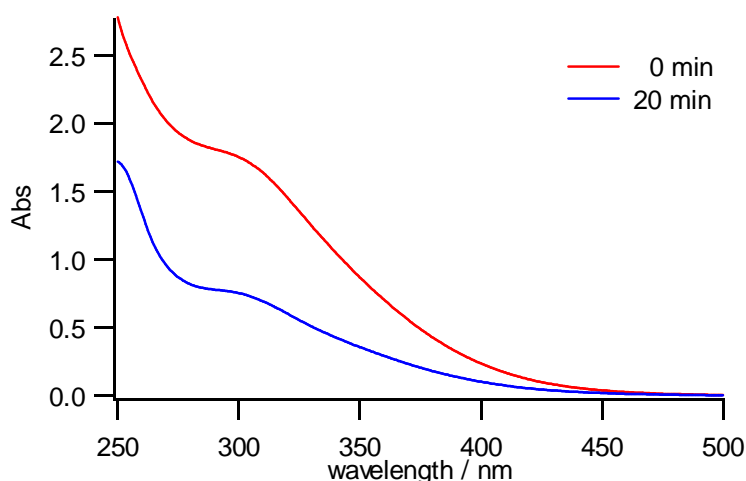


Figure 2-15. UV-Vis absorption spectral change of the solution containing $\text{Ce}(\text{NH}_4)_2(\text{NO}_3)_6$ (1.5 mM) and $\text{Ru}(\text{bda})(\text{pyCF}_3)_2$ (**6**, 1.0 μM) in aqueous HNO_3 (0.1 M) containing 3% acetonitrile.

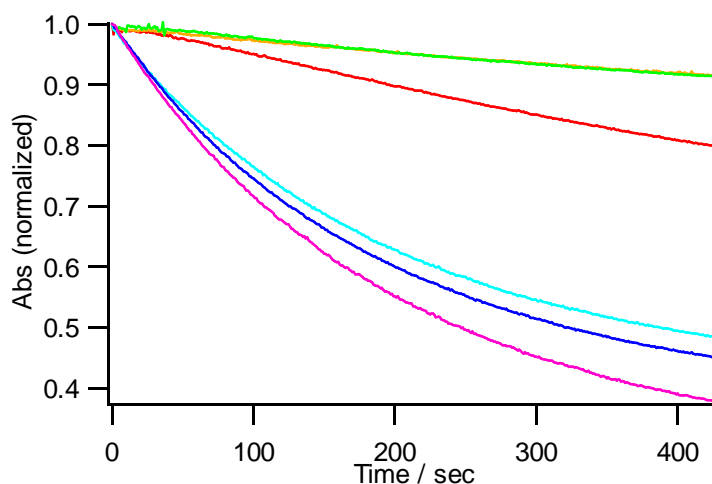


Figure 2-16. Consumption of Ce(IV) monitored by the absorbance at 360 nm in chemical water oxidation catalyzed by Ru(bda)(pyR)₂ **1–6** (1.0 μM) using Ce(NH₄)₂(NO₃)₆ (1.5 mM) as an oxidant in 0.1 M aqueous HNO₃ containing 3% acetonitrile: R = OMe (**1**), red; R = Me (**2**), orange; R = H (**3**), green; R = Br (**4**), light blue; R = CO₂Me (**5**), dark blue; R = CF₃ (**6**), violet.

Table 2-5. Kinetic data of chemical water oxidation catalyzed by complexes **1–6**.

R	$v_i / \mu\text{M s}^{-1}$
OMe (1)	0.829
Me (2)	0.381
H (3)	0.449
Br (4)	4.62
CO ₂ Me (5)	4.87
CF ₃ (6)	5.98

2.2.7 Photochemical water oxidation

Photochemical water oxidation was carried out by the following procedure. The solution containing [Ru(bpy)₃]Cl₂ (0.85 mM), Na₂S₂O₈ (5.0 mM), and Ru complexes **1–6** (17 μM) in 1:1 acetonitrile/borate buffer (40 mM, pH 8.0) was placed in a quartz cell and photoirradiated by a xenon arc lamp equipped with a cut-off filter ($\lambda > 390$ nm). The amounts of O₂ evolved were determined by GC analysis. The time course of the amounts

of O₂ was shown in Fig. 2-17. For all the complexes, the amounts of O₂ evolved increased linearly within initial 30 min, but O₂ generation ceased practically after 120 min of irradiation. The catalytic activity was evaluated by the initial turnover frequency (TOF) with respect to the catalyst, which was estimated from the amounts of O₂ evolved within initial 30 min. The TOF for complexes **1–6** are collected in Table 2-6.

As shown in Table 2-6, complexes **5** and **6**, both of which have the electron-withdrawing groups, exhibited the higher catalytic efficiency than other Ru complexes. Complex **1** (R = OMe) has the higher catalytic activity in comparison with complexes **2** (R = Me) and **3** (R = H). This tendency of the substituent effect in the photochemical water oxidation is qualitatively consistent with that in the chemical water oxidation mentioned in the previous subsection.

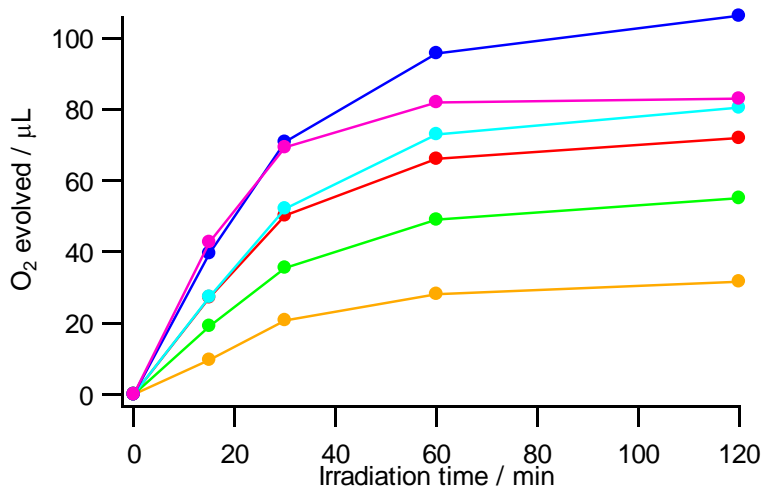


Figure 2-17. Time courses of the amounts of O₂ evolved in the photochemical water oxidation catalyzed by complexes **1–6**: [Ru(bpy)₃]Cl₂ (0.85 mM), Na₂S₂O₈ (5.0 mM), **1–6** (17 μM) in 1:1 acetonitrile/borate buffer (40 mM, pH 8.0), photoirradiated at λ > 390 nm: R = OMe (**1**), red; R = Me (**2**), orange; R = H (**3**), green; R = Br (**4**), light blue; R = CO₂Me (**5**), dark blue; R = CF₃ (**6**), violet.

Table 2-6. Kinetic data of photochemical water oxidation catalyzed by complexes **1–6**.

R	TOF / h ⁻¹
OMe (1)	80.5
Me (2)	33.4
H (3)	56.8
Br (4)	85.2
CO ₂ Me (5)	114
CF ₃ (6)	111

2.2.7 Quenching experiments

To obtain kinetic information about the photochemical water oxidation, quenching experiments were performed. Emission quenching experiment of [Ru(bpy)₃]²⁺ by S₂O₈²⁻ was carried out in air-saturated 1:1 acetonitrile/borate buffer (40 mM, pH 8.0). As shown in Fig. 2-18a, the emission intensity of [Ru(bpy)₃]²⁺ decreased with an increase in the concentration of S₂O₈²⁻.

The Stern-Volmer plot of the emission intensity ratio I_0/I , where I_0 and I stand for emission intensity at the emission maximum in the absence and in the presence of the quencher, respectively, against the quencher concentration, [Q], gave a straight line as shown in Fig. 2-18b. The quenching constant was calculated to be $k_q\tau_0 = 18.7 \text{ M}^{-1}$ by the least-square analysis of the plot using Eq. 2.1,

$$I_0/I = 1 + k_q\tau_0[Q] \quad (2.1)$$

where k_q and τ_0 represent the quenching rate constant and the emission lifetime in the absence of the quencher, respectively.

The emission lifetime of [Ru(bpy)₃]²⁺, τ_0 , was determined in air-saturated and degassed 1:1 acetonitrile/borate buffer. From the slope of the emission decay profile shown in Fig. 2-19, the values of $\log \tau_0$ were obtained. In this way, the emission lifetimes of [Ru(bpy)₃]²⁺ in air-saturated and degassed solvent were determined to be $\tau_0 = 254 \text{ ns}$

and 709 ns, respectively. Since the quenching experiment was carried out in the air-saturated solvent, the quenching rate constant k_q was calculated to be $k_q = 7.36 \times 10^7 \text{ M}^{-1}$ using $\tau_0 = 254 \text{ ns}$.

The quenching of $[\text{Ru}(\text{bpy})_3]^{2+}$ emission by $\text{Ru}(\text{bda})(\text{pyCO}_2\text{Me})_2$ (**5**) was also examined in a similar way. A decrease in the emission intensity was observed by the addition of complex **5** as shown in Fig. 2-20a. However, as illustrated in Fig. 2-20b, since complex **5** has an absorption band around the excitation wavelength (450 nm), the intensity of the light absorbed by $[\text{Ru}(\text{bpy})_3]^{2+}$ is affected by the addition of **5**. Taking the absorbance change into account, the emission intensity ratio I_0/I was corrected by Eq. 2.2,

$$I_0/I(\text{corrected}) = I_0/I(\text{found}) \times (1-10^{-(A(S)+A(Q))})/(1-10^{-A(S)}) \times A(S)/(A(S)+A(Q)) \quad (2.2)$$

where $A(S)$ and $A(Q)$ represent the absorption intensity of $[\text{Ru}(\text{bpy})_3]^{2+}$ and complex **5** at 450 nm, respectively.

The Stern-Volmer plot for the corrected intensity ratio $I_0/I(\text{corrected})$ against the concentration of **5** gave a good straight line (Fig. 2-20c), from which the rate constant for quenching of $[\text{Ru}(\text{bpy})_3]^{2+}$ emission by complex **5** was determined to be $k_q = 7.13 \times 10^9 \text{ M}^{-1}$.

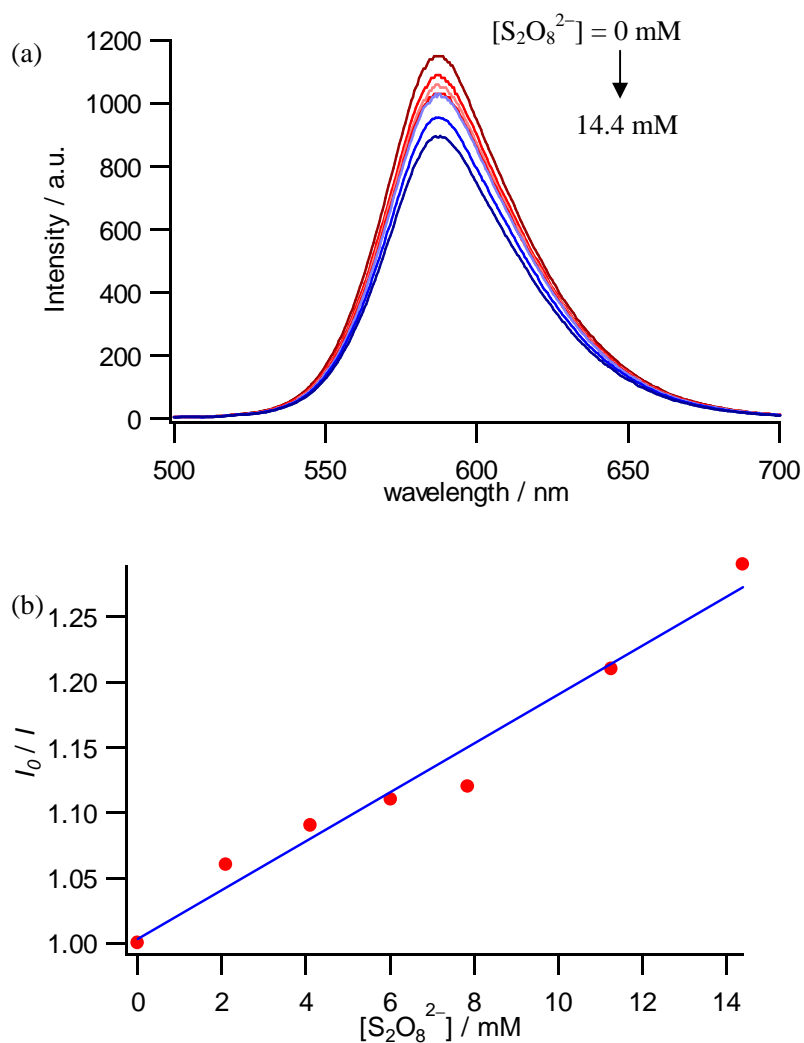


Figure 2-18. Quenching of $[\text{Ru}(\text{bpy})_3]^{2+}$ emission by $\text{S}_2\text{O}_8^{2-}$. (a) Decrease in intensity of $[\text{Ru}(\text{bpy})_3]^{2+}$ emission ($\lambda_{\text{ex}} = 450 \text{ nm}$) by the addition of $\text{Na}_2\text{S}_2\text{O}_8$: $[\text{Ru}(\text{bpy})_3]^{2+} = 51 \mu\text{M}$, in acetonitrile/aqueous borate buffer (40 mM, pH 8.0). (b) Stern-Volmer plot for quenching of the emission by $\text{S}_2\text{O}_8^{2-}$ using the emission intensity at 587 nm. The least-square analysis of the plot yields a quenching constant, $k_q\tau_0$, of 18.7 M^{-1} .

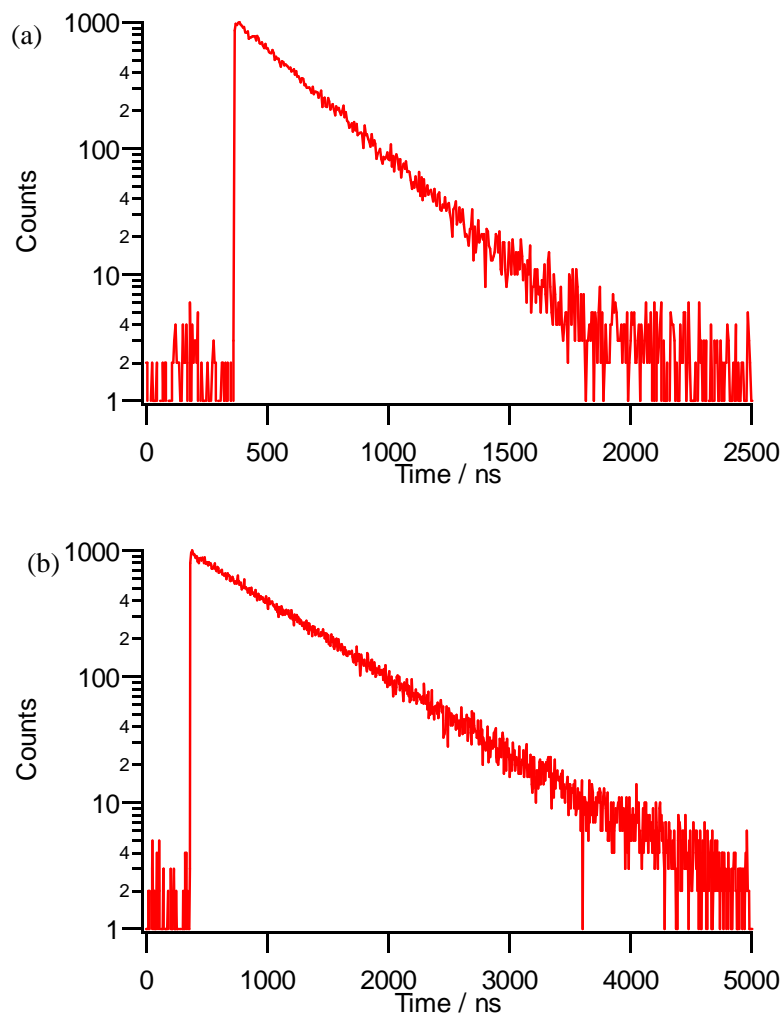


Figure 2-19. Decay profiles of emission of $[\text{Ru}(\text{bpy})_3]^{2+}$ in (a) air-saturated 1:1 acetonitrile/borate buffer (40 mM, pH 8.0) and (b) acetonitrile/borate buffer degassed by Ar-bubbling (the concentration of $[\text{Ru}(\text{bpy})_3]^{2+}$ is 52.4 μM (in air) and 78.5 μM (in Ar)): Excitation, 405 nm; Emission, 605 nm.

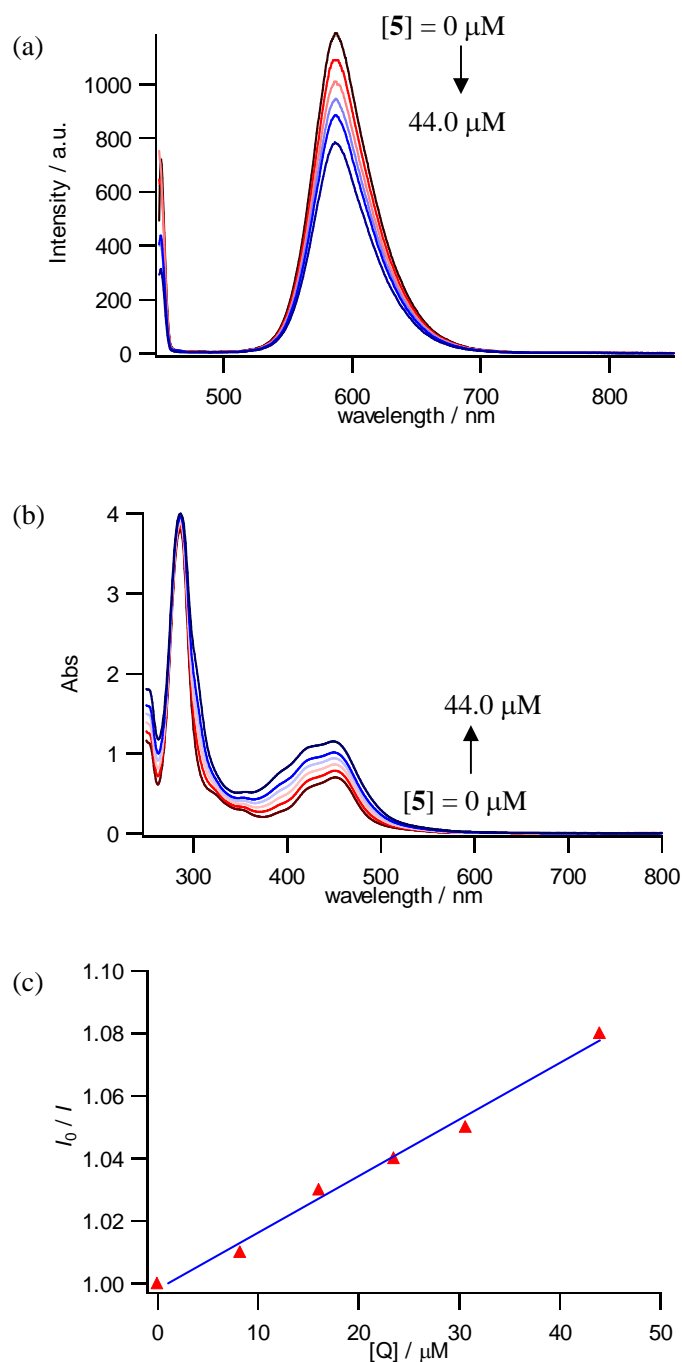


Figure 2-20. Quenching of $[\text{Ru}(\text{bpy})_3]^{2+}$ emission by complex **5**. (a) Decrease in intensity of $[\text{Ru}(\text{bpy})_3]^{2+}$ emission ($\lambda_{\text{ex}} = 450 \text{ nm}$) and (b) absorption spectral change by the addition of **5**: $[\text{Ru}(\text{bpy})_3]^{2+} = 53 \text{ } \mu\text{M}$, in 1:1 acetonitrile/aqueous borate buffer (40 mM, pH 8.0). (c) Stern-Volmer plot for quenching of the emission by **5** using the emission intensity at 588 nm. The least-square analysis of the plot yields a quenching constant, $k_q\tau_0$, of 1810 M^{-1} .

The quenching efficiency η_q , which represents the proportion of the excited sensitizers quenched by the quencher Q, can be estimated by Eq. 2.3.

$$\eta_q = k_q \tau_0 [Q] / (1 + k_q \tau_0 [Q] + k_q' \tau_0 [Q']) \quad (2.3)$$

In this equation, τ_0 represents the emission lifetime under Ar atmosphere, k_q and [Q] are the quenching rate constant and the concentration of the quencher Q, respectively. Moreover, k_q' and [Q'] are those of another quencher Q'.

From Eq. 2.3, the quenching efficiencies of $S_2O_8^{2-}$ and complex **5** were determined to be $\eta_q(S_2O_8^{2-}) = 19.4\%$ and $\eta_q(\mathbf{5}) = 6.4\%$ under the typical photochemical reaction condition ($[S_2O_8^{2-}] = 5.0 \text{ mM}$, $[\mathbf{5}] = 17 \text{ }\mu\text{M}$), respectively. These values suggest that the sensitizers in the excited state are mainly quenched by $S_2O_8^{2-}$.

The redox potential of $[Ru(bpy)_3]^{2+/+}$ has been reported to be -1.81 V (vs. Fc^+/Fc).⁷ In addition, the excited-state energy corresponding to the emission maximal wavelength of $[Ru(bpy)_3]^{2+}$ has been reported to be 2.04 eV .⁷ Based on these data, the reduction potential of the excited sensitizer, $[Ru(bpy)_3]^{2+(*)/+}$, is calculated to be 0.23 V . Fig. 2-21 shows the energy diagram for redox reactions involving $[Ru(bpy)_3]^{2+}$ and complex **5**, the $Ru^{III/II}$ oxidation potential of which is reported in §2.2.4. The figure indicates that the reductive quenching of $[Ru(bpy)_3]^{2+}$ in its excited state by complex **5** is slightly exothermic. However, the reductive quenching by the $Ru(III)$ or $Ru(IV)$ species of **5** is thought to be endothermic, since the redox potentials of these species are expected to be more positive than that of $Ru(II)$. As a reference, in the case of complex **2** ($R = Me$), redox potentials of $Ru^{III/II}$, $Ru^{IV/III}$ and $Ru^{V/IV}$ in aqueous CF_3SO_3H solution (pH 1.0) have been reported to be 0.86 V , 1.11 V and 1.5 V (vs. NHE) respectively.¹ Therefore, the catalytic photochemical water oxidation reaction is likely to proceed via oxidative quenching of $[Ru(bpy)_3]^{2+}$ in its excited state by $S_2O_8^{2-}$.

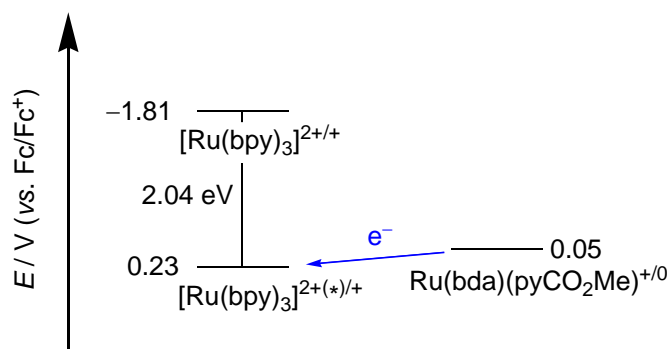
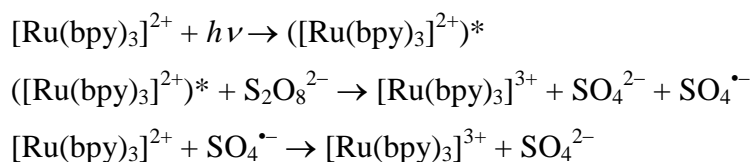


Figure 2-21. Energy diagram of reductive quenching of the excited $[\text{Ru}(\text{bpy})_3]^{2+}$ by $\text{Ru}^{\text{II}}(\text{bda})(\text{pyCO}_2\text{Me})_2$ (**5**).

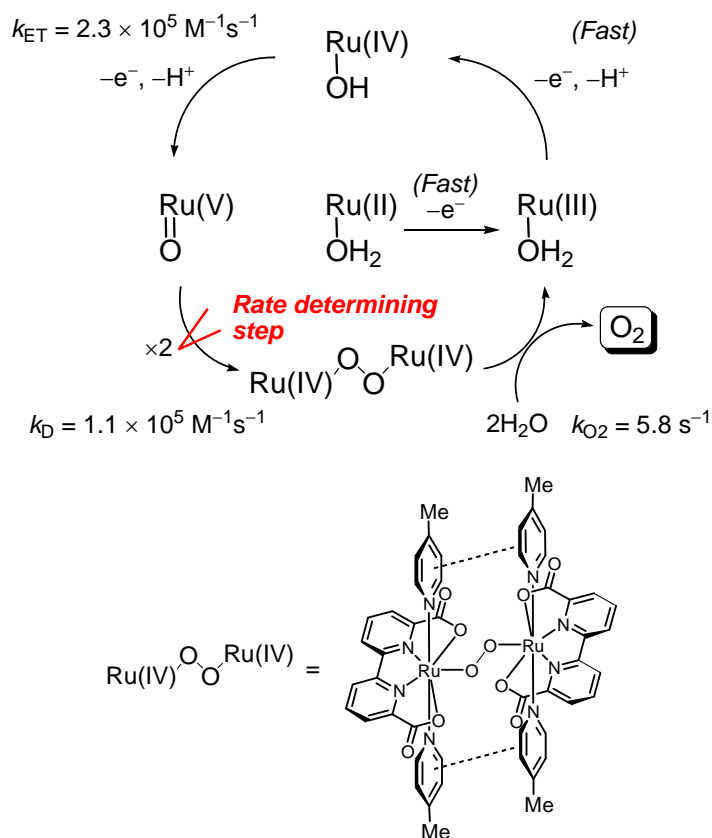
2.2.9 Reaction mechanism

It is known that $\text{S}_2\text{O}_8^{2-}$ reacts with $[\text{Ru}(\text{bpy})_3]^{2+}$ by a photochemical reaction, followed by a thermal reaction as shown below.^{1,8} When the excited state ($[\text{Ru}(\text{bpy})_3]^{2+*}$) is oxidatively quenched by $\text{S}_2\text{O}_8^{2-}$, a one-electron oxidized species $[\text{Ru}(\text{bpy})_3]^{3+}$ is generated. In addition, a strong oxidant $\text{SO}_4^{\bullet-}$, which is produced by the decomposition of the reduced $\text{S}_2\text{O}_8^{2-}$, oxidizes the ground state $[\text{Ru}(\text{bpy})_3]^{2+}$ to generate $[\text{Ru}(\text{bpy})_3]^{3+}$. Finally, in the photochemical water oxidation system, $[\text{Ru}(\text{bpy})_3]^{3+}$ oxidizes the ruthenium catalyst.



It has been reported by Sun and co-workers that the water oxidation reaction catalyzed by $\text{Ru}(\text{bda})(\text{pyMe})_2$ proceeds by a mechanism shown in Scheme 2-2.⁴ The catalyst is oxidized to the Ru(V) species through the Ru(III) and Ru(IV) species. Two Ru(V)=O molecules dimerize to form Ru(IV)-O-O-Ru(IV), and finally, O_2 is released with the regeneration of the Ru(III) species.

Scheme 2-2. The reaction cycle of water oxidation catalyzed by Ru(bda)(pyMe)₂ proposed by Sun and co-workers.⁴



In recent years, Sun *et al.* have also investigated chemical water oxidation catalyzed by Ru(bda)(pyR)₂ complexes using CAN as an oxidant and reported that electron-withdrawing groups enhance the catalytic activity of the complex because the dimerization step of two Ru(V)=O species to form Ru(IV)-O-O-Ru(IV) peroxo dimer is accelerated by the electron-withdrawing groups.² Although they have not examined the photochemical water oxidation, the photochemical reaction can be also accelerated by the electron-withdrawing groups because the reaction rate of the dimerization step is increased by the electron-withdrawing groups.

They have also reported that the OMe-substituted complex has a catalytic activity slightly higher than the unsubstituted one in the chemical water oxidation.² However, they have not referred to the reason why the electron-donating groups enhance the catalytic activity. Probably, two reasons can be considered. First, the electron-donating

groups accelerate the oxidation step of Ru(IV)→Ru(V) so that the steady-state concentration of the Ru(V)=O species are increased, leading to the acceleration of the dimerization step. Second, an increase in the strength of the Ru-N(py) bond by the electron donating ability of the substituents is possibly responsible for the high catalytic activity. Sun *et al.* have reported that Ru(bda)L₂ complexes deactivates in the catalytic reaction because of the dissociation of the axial *N*-heteroaromatic ligands.² Therefore, each reaction step in the catalytic cycle can be assumed to be competitive against the dissociation of the pyridine ligands. When the electron donating groups are introduced on the pyridine ligand, the coordination bond between the pyridine ligand and the Ru center will be strengthened, and the rate of the dissociation of the pyridine ligand is lowered, resulting in the acceleration of the desired catalytic reaction.

2.3 Summary

In this chapter, a series of Ru(bda)(pyR)₂ complexes **1–6** (R = OMe, Me, H, Br, CO₂Me, and CF₃) having substituent groups at the 4-position of the axial pyridine ligands were prepared, and their physical properties and catalytic activities in the chemical and photochemical water oxidation were investigated.

The DFT calculations indicated that the absorption assigned to the MLCT transition of Ru d → py π* largely shifts and the energy level of HOMO, which is localized to the Ru center, is slightly deviated by introduction of the substituent groups on the pyridine ligands. These results predicted by the calculations were consistent with the observation in the UV-Vis absorption spectra and cyclic voltammograms of complexes **1–6**.

Chemical water oxidation catalyzed by complexes **1–6** was examined using Ce(NH₄)₂(NO₃)₆ as an oxidant. The reaction rate was estimated from the consumption of Ce(IV) monitored by UV-Vis absorption measurement. The initial water oxidation rates using complexes **4–6** (R = Br, CO₂Me, CF₃) were found to be especially high, while the catalytic activity of complex **1** (R = OMe) was relatively higher than those of complexes **2** and **3** (R = Me, H). Then, photochemical water oxidation was examined using [Ru(bpy)₃]²⁺ as a sensitizer and S₂O₈²⁻ as a sacrificial electron acceptor, estimating the amounts of generated oxygen by GC analysis. It was found that the catalytic efficiency of complexes **5** and **6** (R = CO₂Me, CF₃) was particularly high, and complex **1** (R = OMe) had a relatively higher catalytic activity than complexes **2** and **3** (R = Me, H). This tendency of the substituent effect on the reaction efficiency is qualitatively consistent with that observed in the chemical water oxidation experiments.

Very recently, Sun and co-workers have reported the substituent effect on the chemical water oxidation catalyzed by Ru(bda)(pyR)₂ (R = OMe, H, Br, and CO₂Me).² They have concluded that the catalytic efficiency of the complexes is enhanced by electron-withdrawing groups because the electron-withdrawing nature of the substituents accelerates the dimerization step, 2Ru(V)=O → Ru(IV)-O-O-Ru(IV), while the small positive effect of the electron-donating groups has not been discussed. On the basis of the reaction mechanism presented by Sun *et al.*, I considered that the electron-donating

groups have two positive effects on the catalytic efficiency: (i) oxidation of Ru(IV), $\text{Ru(IV)-OH} \rightarrow \text{Ru(V)=O}$, is accelerated, leading to the high steady-state concentration of Ru(V)=O. (ii) Dimerization of Ru(V)=O species is accelerated by the intermolecular π - π interaction between the axial pyridine ligands. This interaction is enhanced by the electron-donating groups.

The incorporation of compounds into hydrophobic vesicle membranes often requires the introduction of long alkyl chains especially when the compounds have moderate hydrophilicity.⁹ In this chapter, complex **5** having CO_2Me substituents was found to have a particularly high catalytic activity in water oxidation. Therefore, I considered that an ester bond is expected not only to enhance the catalytic activity, but also to connect with long alkyl chains to the catalyst, which will give the amphiphilicity sufficient for the incorporation into vesicle membranes.

2.4 Experimental

Materials. Most of chemicals were purchased from Sigma-Aldrich or Tokyo Kasei Kogyo Co. Ltd. (TCI) or Wako Pure Industries Ltd. (Wako) or Kanto Chemical Co. Inc unless otherwise noted. All reagents were used as supplied unless otherwise stated. Spectrum grade organic solvents and distilled water used for spectroscopic measurements and water oxidation experiments were purchased from Wako.

General methods. Aluminum oxide 90 active neutral for column chromatography (70-230 mesh) was purchased from Merck KGaA. ^1H NMR spectra were recorded on a Bruker AVANCE 500 spectrometer. Chemical shifts are reported by using tetramethylsilane ($\delta = 0.00$) in CDCl_3 , and residual proton peak ($\delta = 2.50$) in $\text{DMSO-}d_6$ for ^1H NMR as internal standards. UV-Vis absorption spectra were recorded on a JASCO V-560 spectrometer. Phosphorescence spectra were recorded on a JASCO FP-777 spectrofluorometer. Melting points (m.p.) were recorded on YAZAWA BY-2. Elemental analyses were performed using an Elementar vario MICRO cube at the Microanalytical Laboratory (Department of Chemistry, School of Science, The University of Tokyo). Irradiation was carried out using a xenon arc lamp (Wacom, lamp house HX500W) with a cut-off filter (TOSHIBA L-39). Gas chromatographs were recorded on YANACO Gas Chromatograph G2700TF (TCD analytic column: 3 mm \times 3 mm stainless column, activated carbon (60-80 mesh)).

Preparation of 2,2'-bipyridine-6,6'-dicalboxylic acid (bdaH_2).¹⁰

6,6'-Dimethyl-2,2'-bipyridyl (99.4 mg, 540 μmol) was added slowly to concentrated sulfuric acid (2 mL) at 0°C. Chromium(VI) oxide (336.5 mg, 3.37 mmol) was added in small portions to the solution at 0°C. The reaction mixture was stirred for 2 days at room temperature and then poured onto crushed ice. The white precipitate formed was filtered off and washed with cold water, ethanol and ether to yield bdaH_2 (134.5 mg, 100%) as pale yellow solid; ^1H NMR (500 MHz, DMSO) δ 13.32 (brs, 2H), 8.75 (dd, $J = 7.8, 1.3$

Hz, 2H), 8.19 (t, $J = 7.8$ Hz, 2H), 8.14 (dd, $J = 7.8, 1.3$ Hz, 2H).

Preparation of dichlorotetrakis(dimethyl sulfoxide)ruthenium(II)

(Ru(DMSO)₄Cl₂).¹¹ A solution of ruthenium(III) chloride (211.1 mg, 1.02 mmol) and water (50 μ L) in dimethyl sulfoxide (2 mL) was stirred at 180°C for 10 min. The reaction mixture was concentrated by distillation under reduced pressure. Acetone (5 mL) was added, and yellow precipitate was filtered off. The solid was washed with acetone to give the target molecule (354.4 mg, 72%) as yellow solid; ¹H NMR spectrum of this compound in CDCl₃ is known to be complicated.^{11,12} Signals corresponding to DMSO coordinated by its S atom were observed around 3.3–3.6 ppm, DMSO coordinated by its O atom was at 2.73 ppm and DMSO dissociated from Ru centre was at 2.62 ppm.¹¹

Preparation of methyl isonicotinate (pyCO₂Me).¹³ A solution of isonicotinic acid (1.20 g, 9.74 mmol) and concentrated sulfuric acid (1 mL) in methanol (20 mL) was refluxed for 3 h. Water was added to the reaction mixture, and it was neutralized to pH 7 by a saturated NaHCO₃ aqueous solution. The solution was extracted with CH₂Cl₂. The organic layer was separated, dried over Na₂SO₄, filtered, and concentrated under reduced pressure to give pyCO₂Me (1.08 g, 81%) as pale yellow oil; ¹H NMR (500 MHz, CDCl₃) δ 8.78 (dd, $J = 4.5, 1.5$ Hz, 2H), 7.85 (dd, $J = 4.5, 1.5$ Hz, 2H), 3.97 (s, 3H).

Synthesis of Ru(bda)(pyOMe)₂ (1).² To a suspension of bdaH₂ (24.5 mg, 100 μ mol) and Ru(DMSO)₄Cl₂ (48.4 mg, 99.9 μ mol) in methanol (2 mL) deaerated by passing argon through it, triethylamine (80 μ L, 0.57 mmol) was added under argon atmosphere. After refluxing for 4 h, 4-methoxypyridine (0.25 mL, 2.5 mmol) was added and the mixture was refluxed for 6 h. The resulting mixture was concentrated under reduced pressure, and the residue was washed with ether. After purification by column chromatography on aluminum gel (CH₂Cl₂, CH₂Cl₂-methanol (10 : 1) as eluent), the resulting solid was recrystallized from CH₂Cl₂-ether, dissolved in CHCl₃, washed with water, dried over Na₂SO₄, and filtered. The filtrate was concentrated under reduced

pressure to give **1** (27.0 mg, 48%) as a red-brown solid; ^1H NMR (500 MHz, CDCl_3) δ 8.12 (d, $J = 7.8$ Hz, 2H), 8.11 (d, $J = 7.8$ Hz, 2H), 7.64 (t, $J = 7.8$ Hz, 4H), 7.53 (dd, $J = 5.8, 1.5$ Hz, 4H), 6.53 (dd, $J = 5.8, 1.0$ Hz, 4H), 3.72 (s, 6H).

Synthesis of Ru(bda)(pyMe)₂ (2).¹ To a suspension of bdaH₂ (23.7 mg, 97.1 μmol) and Ru(DMSO)₄Cl₂ (48.1 mg, 99.3 μmol) in methanol (2 mL) deaerated by passing argon through it, triethylamine (80 μL , 0.57 mmol) was added under argon atmosphere. After refluxing for 20 h, 4-picoline (0.20 mL, 2.1 mmol) was added and the mixture was refluxed for 3 h. The resulting mixture was concentrated under reduced pressure, and the residue was purified by column chromatography on aluminum gel (CH_2Cl_2 -methanol (50 : 1, 10 : 1) as eluent). The resulting solid was recrystallized from CH_2Cl_2 -ether and washed with ether to give **2** (30.0 mg, 58%) as a red-brown solid; ^1H NMR (500 MHz, CDCl_3) δ 8.14 (dd, $J = 8.0, 1.0$ Hz, 2H), 8.11 (dd, $J = 8.0, 1.0$ Hz, 2H), 7.67 (t, $J = 8.0$ Hz, 2H), 7.59 (dd, $J = 6.0, 1.5$ Hz, 4H), 6.82 (d, $J = 6.0$ Hz, 4H), 2.21 (s, 6H).

Synthesis of Ru(bda)(pyH)₂ (3).² To a suspension of bdaH₂ (24.2 mg, 99.1 μmol) and Ru(DMSO)₄Cl₂ (48.3 mg, 99.7 μmol) in methanol (2 mL) deaerated by passing argon through it, triethylamine (80 μL , 0.57 mmol) was added under argon atmosphere. After refluxing for 20 h, pyridine (0.16 mL, 2.0 mmol) was added and the mixture was refluxed for 3 h. The resulting mixture was concentrated under reduced pressure, and the residue was purified by column chromatography on aluminum gel (CH_2Cl_2 -methanol (50 : 1, 10 : 1) as eluent). The resulting solid was recrystallized from CH_2Cl_2 -ether and washed with ether to give **3** (26.8 mg, 54%) as a red-brown solid; ^1H NMR (500 MHz, CDCl_3) δ 8.18 (dd, $J = 8.1, 0.9$ Hz, 2H), 8.12 (dd, $J = 8.1, 0.9$ Hz, 2H), 7.80 (dd, $J = 7.0, 1.5$ Hz, 4H), 7.71 (t, $J = 8.1$ Hz, 2H), 7.49 (tt, $J = 7.0, 1.5$ Hz, 2H), 7.03 (td, $J = 7.0, 0.5$ Hz, 4H).

Synthesis of Ru(bda)(pyBr)₂ (4).² To a suspension of bdaH₂ (24.5 mg, 100 μmol) and Ru(DMSO)₄Cl₂ (48.8 mg, 101 μmol) in methanol (5 mL) deaerated by passing argon through it, triethylamine (200 μL, 1.4 mmol) was added under argon atmosphere. After refluxing for 3 h, a solution of 4-bromopyridine hydrochloride (156.0 mg, 802 μmol) in methanol (5 mL) and triethylamine (100 μL, 0.72 mmol) was added and the mixture was refluxed for 2 days. The resulting mixture was concentrated under reduced pressure, and the residue was purified by column chromatography on aluminum gel (CH₂Cl₂-methanol (50 : 1, 20 : 1) as eluent). The resulting solid was recrystallized from CHCl₃-ether and washed with ether to give **4** (13.6 mg, 21%) as a red-brown solid; ¹H NMR (500 MHz, CDCl₃) δ 8.18 (d, *J* = 7.8 Hz, 2H), 8.15 (d, *J* = 7.8 Hz, 2H), 7.74 (t, *J* = 7.8 Hz, 2H), 7.60 (d, *J* = 6.5 Hz, 4H), 7.20 (d, *J* = 6.5 Hz, 4H).

Synthesis of Ru(bda)(pyCO₂Me)₂ (5). To a suspension of bdaH₂ (24.4 mg, 99.9 μmol) and Ru(DMSO)₄Cl₂ (48.3 mg, 99.7 μmol) in methanol (2 mL) deaerated by passing nitrogen through it, triethylamine (80 μL, 0.57 mmol) was added under nitrogen atmosphere. After refluxing for 3 h, methyl isonicotinate (pyCO₂Me) (0.24 mL, 2.0 mmol) was added and the mixture was refluxed for 14 h. The resulting mixture was concentrated under reduced pressure and filtered with cotton. The filtrate was evaporated, and the residue was recrystallized from methanol-ether to give **5** (34.9 mg, 57%) as a red-brown solid; m.p. > 300 °C; ¹H NMR (500 MHz, CDCl₃) δ 8.24 (dd, *J* = 8.0, 0.5 Hz, 2H), 8.12 (dd, *J* = 8.0, 0.5 Hz, 2H), 8.00 (dd, *J* = 5.3, 1.5 Hz, 4H), 7.78 (t, *J* = 8.0 Hz, 2H), 7.57 (dd, *J* = 5.3, 1.5 Hz, 4H), 3.89 (s, 6H); Anal. Calcd for C₂₆H₂₀N₄O₈Ru•H₂O : C, 49.14; H, 3.48; N, 8.82. Found: C, 49.37; H, 3.63; N, 8.91.

Synthesis of Ru(bda)(pyCF₃)₂ (6).³ To a suspension of bdaH₂ (24.4 mg, 99.9 μmol) and Ru(DMSO)₄Cl₂ (49.9 mg, 103 μmol) in methanol (2 mL) deaerated by passing argon through it, triethylamine (80 μL, 0.57 mmol) was added under argon atmosphere. After refluxing for 16 h, 4-trifluoromethylpyridine (50 μL, 0.43 mmol) was added and the mixture was refluxed for 3 h. The resulting mixture was concentrated

under reduced pressure, and the residue was purified by column chromatography on aluminum gel (CH₂Cl₂-methanol (50 : 1, 10 : 1) as eluent). The resulting solid was recrystallized from CH₂Cl₂-ether to give **6** (37.0 mg, 58%) as a red-brown solid; ¹H NMR (500 MHz, CDCl₃) δ 8.26 (dd, *J* = 1.0, 7.8 Hz, 2H), 8.16 (dd, *J* = 1.0, 7.8 Hz, 2H), 8.06 (d, *J* = 6.3 Hz, 4H), 7.81 (t, *J* = 7.8 Hz, 2H), 7.28 (d, *J* = 6.3 Hz, 4H).

Chemical water oxidation. A solution of 1.5 mM cerium ammonium nitrate (CAN) in 0.1 M nitric acid (2.9 mL) was placed in a quartz cell (10 mm × 10 mm), and to the solution was injected a solution of 30 μM ruthenium catalyst in acetonitrile (100 μL). Just after the addition of the catalyst solution, the consumption of Ce(IV) was recorded on a UV-Vis absorption spectrometer (360 nm).

In the following equations, *A*, *C*, and *t* mean absorbance at 360 nm, concentration of Ce(IV), and time, respectively, and *A*₀, *C*₀, and *t*₀ mean the corresponding initial values. The change in absorbance at 360 nm was analyzed using a single exponential function as shown in Eq. 2.4.

$$A = k_0 + k_1 \exp(-k_2 t) \quad (2.4)$$

Here, the concentration of Ce(IV) (*C*) is estimated by Eq. 2.5, and the initial rate of Ce(IV) consumption (*v*_i) can be evaluated using Eq. 2.6.

$$C = A \times (C_0 / A_0) \quad (2.5)$$

$$\begin{aligned} v_i &= -dC / dt|_{t=t_0} \\ &= k_1 k_2 \exp(-k_2 t_0) \times (C_0 / A_0) \end{aligned} \quad (2.6)$$

From Eq. 2.4, the relationship of $k_1 \exp(k_2 t_0) = A_0 - k_0$ is obtained. Using this relationship, Eq. 2.6 can be eventually deformed to Eq. 2.7, which is employed for the estimation of *v*_i.

$$v_i = C_0 k_2 (1 - (k_0 / A_0)) \quad (2.7)$$

Photochemical water oxidation. A solution of [Ru(bpy)₃]Cl₂•6H₂O (1.9 mg, 2.5 μmol) and Na₂S₂O₈ (3.6 mg, 15 μmol) in 1:1 acetonitrile/borate buffer (40 mM, pH 8.0, 2.9 mL) was placed in a quartz cell (10 mm × 10 mm), and to the solution was added a solution of the ruthenium catalyst in acetonitrile (510 μM, 100 μL). Then the solution was irradiated using a xenon arc lamp through a cut-off filter ($\lambda > 390$ nm) after passing argon through the solution for 1 h to remove air. The gas (0.5 mL) was taken from the gas phase of the quartz cell by a gas tight syringe, then it was analyzed by gas chromatography to determine the quantity of generated oxygen.

Emission quenching studies. The quenching of [Ru(bpy)₃]²⁺ emission by addition of S₂O₈²⁻ was recorded by repetition of the following cycles; to a solution of [Ru(bpy)₃]²⁺ (50.9 μM) in 1:1 acetonitrile/borate buffer (40 mM, pH 8.0) was added a certain volume of a solution of [Ru(bpy)₃]²⁺ in acetonitrile/borate buffer containing Na₂S₂O₈ (86.4 mM) and the emission spectrum was recorded. Relative emission intensities (I_0/I) were determined by measuring the intensities of emission maximum (587 nm). The quenching of [Ru(bpy)₃]²⁺ emission by Ru(bda)(pyCO₂Me)₂ (**5**) was also carried out in a similar manner using [Ru(bpy)₃]²⁺ (52.9 μM) and complex **5** (337 μM).

Cyclic voltammetry. CH₂Cl₂ was distilled prior to use for the electrochemical measurement. Cyclic voltammetry was carried out in nitrogen-purged CH₂Cl₂ using a HOKUTO DENKO potentiostat/galvanostat HAB-151 equipped with a Runtime Corporation X-Y Recorder (Voltam-REC). Tetrabutylammonium perchlorate (0.1 M) in CH₂Cl₂ was used as a supporting electrolyte. The conventional three-electrode configuration consisted of a glassy carbon working electrode, a platinum wire auxiliary electrode and a Ag/Ag⁺ reference electrode.

Theoretical calculations. Calculations were carried out using the Gaussian 03 program package.¹⁴ Geometry optimizations were performed on the ground state using the B3LYP functional together with the 6-31G basis set on C, H, N, O, F, and Br atoms; the LANL2DZ effective core potentials and accompanying basis set were used on the Ru atom.

References and notes

1. L. Duan; Y. Xu; P. Zhang; M. Wang; L. Sun, *Inorg. Chem.*, **2010**, *49*, 209.
2. L. Duan; L. Wang; A. K. Inge; A. Fischer; X. Zou; L. Sun, *Inorg. Chem.*, **2013**, *52*, 7844.
3. Y. Jiang; F. Li; F. Huang; B. Zhang; L. Sun, *Chin. J. Cat.*, **2013**, *34*, 1489.
4. L. Duan; F. Bozoglian; S. Mandel; B. Stewart; T. Privalov; A. Llobet; L. Sun, *Nat. Chem.*, **2012**, *4*, 418.
5. J. An; L. Duan; L. Sun, *Faraday Discuss.*, **2012**, *155*, 267.
6. K. Kalyanasundaram, *Coord. Chem. Rev.*, **1982**, *46*, 159.
7. J. I. Goldsmith; W. R. Hudson; M. S. Lowry; T. H. Anderson; S. Bernhard, *J. Am. Chem. Soc.*, **2005**, *127*, 7502.
8. K. Henbest; P. Douglas; M. S. Garley; A. Mills, *J. Photochem. Photobiol. A: Chem.*, **1994**, *80*, 299.
9. M. Hansen; F. Li; L. Sun; B. König, *Chem. Sci.*, **2014**, *5*, 2683.
10. G. Bozoklu; C. Marchal; C. Gateau; J. Pécaut; D. Imbert; M. Mazzanti, *Chem. Eur. J.*, **2010**, *16*, 6159.
11. S. A. A. Santana; V. P. Carvalho Jr.; B. S. Lima-Neto, *J. Braz. Chem. Soc.*, **2010**, *21*, 279.
12. K. Nomiya; H. Torii; K. Nomura; Y. Sato, *J. Chem. Soc., Dalton Trans.*, **2001**, 1506.
13. K.-G. Liu; X.-Q. Cai; X.-C. Li; D.-A. Qin; M.-L. Hu, *Inorg. Chim. Acta*, **2012**, *388*, 78.
14. M. J. Frisch; G. W. Trucks; H. B. Schlegel; G. E. Scuseria; M. A. Robb; J. R. Cheeseman; J. A. Montgomery, Jr.; T. Vreven; K. N. Kudin; J. C. Burant; J. M. Millam; S. S. Iyengar; J. Tomasi; V. Barone; B. Mennucci; M. Cossi; G. Scalmani; N. Rega; G. A. Petersson; H. Nakatsuji; M. Hada; M. Ehara; K. Toyota; R. Fukuda; J. Hasegawa; M. Ishida; T. Nakajima; Y. Honda; O. Kitao; H. Nakai; M. Klene; X. Li; J. E. Knox; H. P. Hratchian; J. B. Cross; C. Adamo; J. Jaramillo; R. Gomperts; R. E. Stratmann; O. Yazyev; A. J. Austin; R. Cammi; C. Pomelli; J. W. Ochterski; P. Y. Ayala; K. Morokuma; G. A. Voth; P. Salvador; J. J. Dannenberg; V. G. Zakrzewski; S. Dapprich; A. D. Daniels;

M. C. Strain; O. Farkas; D. K. Malick; A. D. Rabuck; K. Raghavachari; J. B. Foresman; J. V. Ortiz; Q. Cui; A. G. Baboul; S. Clifford; J. Cioslowski; B. B. Stefanov; G. Liu; A. Liashenko; P. Piskorz; I. Komaromi; R. L. Martin; D. J. Fox; T. Keith; M. A. Al-Laham; C. Y. Peng; A. Nanayakkara; M. Challacombe; P. M. W. Gill; B. Johnson; W. Chen; M. W. Wong; C. Gonzalez; J. A. Pople, *Gaussian 03*, Revision C.02; Gaussian, Inc., Wallingford, CT, 2004.

Chapter 3 Photochemical Water Oxidation in Vesicles

3.1 Introduction

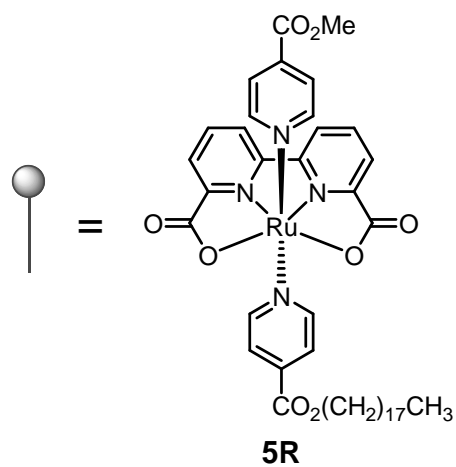
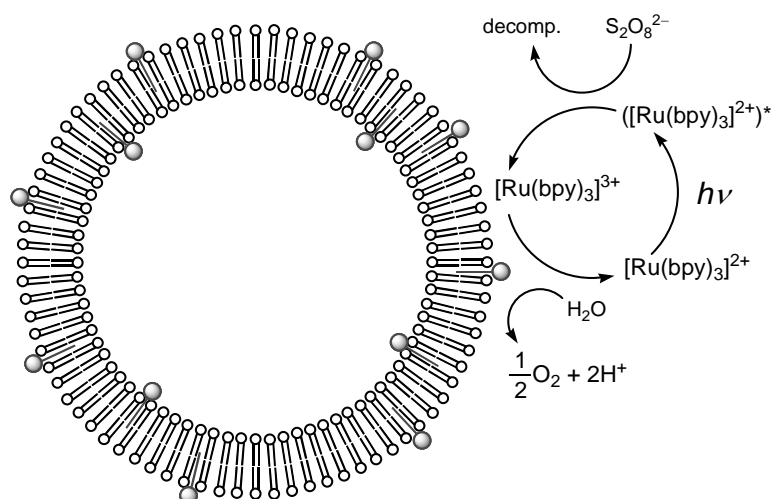
Natural photosynthetic system utilizes the bilayer membrane as a reaction field, in which the highly efficient electron transport is achieved and the charge separation energy is finally converted into chemical potential.

As previously stated in Chapter 1, vesicles are almost spherical bilayer membranes having an inner waterpool, which are formed by self-organization of amphiphiles such as phospholipids. As a model of photosynthetic system, vesicles are thought to be attractive because it has been reported that the membranes of micelles or vesicles work as a barrier to suppress undesired back electron transfer so that the charge-separated state has a long lifetime.¹ Additionally, in general, vesicles possess a relatively larger volume of hydrophobic field to embed molecules working as sensitizers or catalysts compared with micelles. Therefore, energy conversion in vesicles such as photochemical water splitting is an ideal system mimicking natural photosynthetic system. Photochemical hydrogen generation in vesicles has been reported by our laboratory.² However, the construction of catalytic water oxidation systems in vesicles is necessary to achieve water splitting in vesicles.

In Chapter 2, I revealed that the Ru(bda)(pyR)₂ complexes with electron-withdrawing substituents such as R = CO₂Me and CF₃ groups exhibit high catalytic activity in water oxidation. Taking this result into account, at first, I designed a symmetric complex Ru(bda)(pyCO₂Ocd)₂ (Ocd = *n*-octadecyl) having long alkyl chains connected by an ester bond as a catalyst in water oxidation working in vesicle membranes, which was readily synthesized through standard procedure using pyCO₂Ocd. However, as mentioned in §3.2.4, a vesicle solution containing Ru(bda)(pyCO₂Ocd)₂ was turbid, which was unsuitable for photochemical reactions. Thus, I designed an asymmetric ruthenium complex, Ru(bda)(pyCO₂Me)(pyCO₂Ocd) (**5R**, Scheme 3-1). In this chapter, I report the preparation of **5R**, its incorporation into vesicle membranes, and photochemical water oxidation catalyzed by **5R** embedded into vesicle membranes. The

photochemical water oxidation system described in this chapter is also sketched in Scheme 3-1.

Scheme 3-1. Chemical structure of Ru(bda)(pyCO₂Me)(pyCO₂Ocd) (**5R**) and schematic illustration of photochemical water oxidation catalyzed by complex **5R** embedded into vesicle membranes.



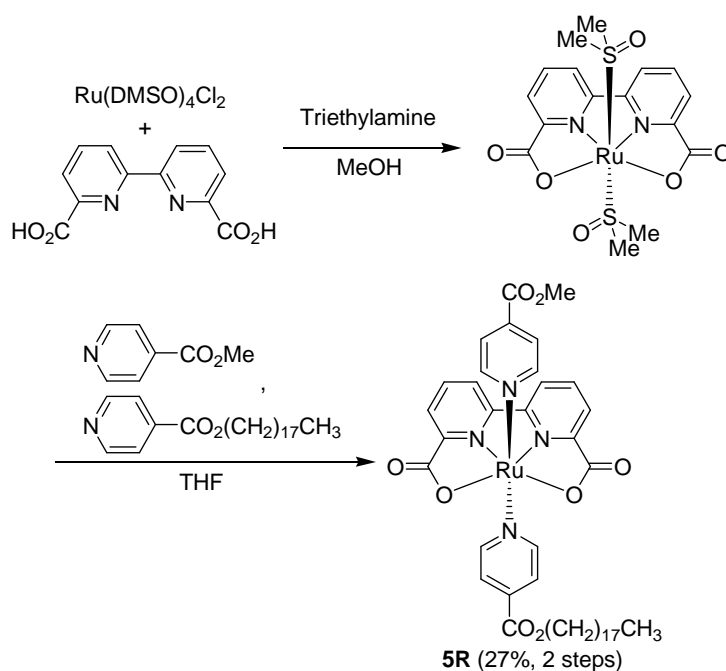
3.2 Results and discussion

3.2.1 Synthesis

Ru(bda)(pyCO₂Me)(pyCO₂Ocd) (**5R**) was synthesized according to the following procedure (Scheme 3-2). Reaction of Ru(DMSO)₄Cl₂ and H₂bda in the presence of excess triethylamine in MeOH produced Ru(bda)(DMSO)₂ as an intermediate complex. Ru(bda)(DMSO)₂ was isolated and treated with an equimolar mixture of methyl isonicotinate and octadecyl isonicotinate in THF to afford **5R** with Ru(bda)(pyCO₂Me)₂ and Ru(bda)(pyCO₂Ocd)₂ as by-products. The desired complex **5R** was isolated by column chromatography on alumina gel and obtained in a total yield of 27%.

The structure of **5R** was confirmed by ¹H NMR and elemental analysis. Moreover, ESI-MS spectrometry measurement was performed. As shown in Fig. 3-1, signals due to complex **5R** was mainly observed, while signals corresponding to Ru(bda)(pyCO₂Me)₂ and Ru(bda)(pyCO₂Ocd)₂ were exceedingly small. Therefore, it was confirmed that the obtained product is complex **5R**, not a mixture with Ru(bda)(pyCO₂Me)₂ and Ru(bda)(pyCO₂Ocd)₂.

Scheme 3-2. Synthesis of Ru(bda)(pyCO₂Me)(pyCO₂Ocd) (**5R**).



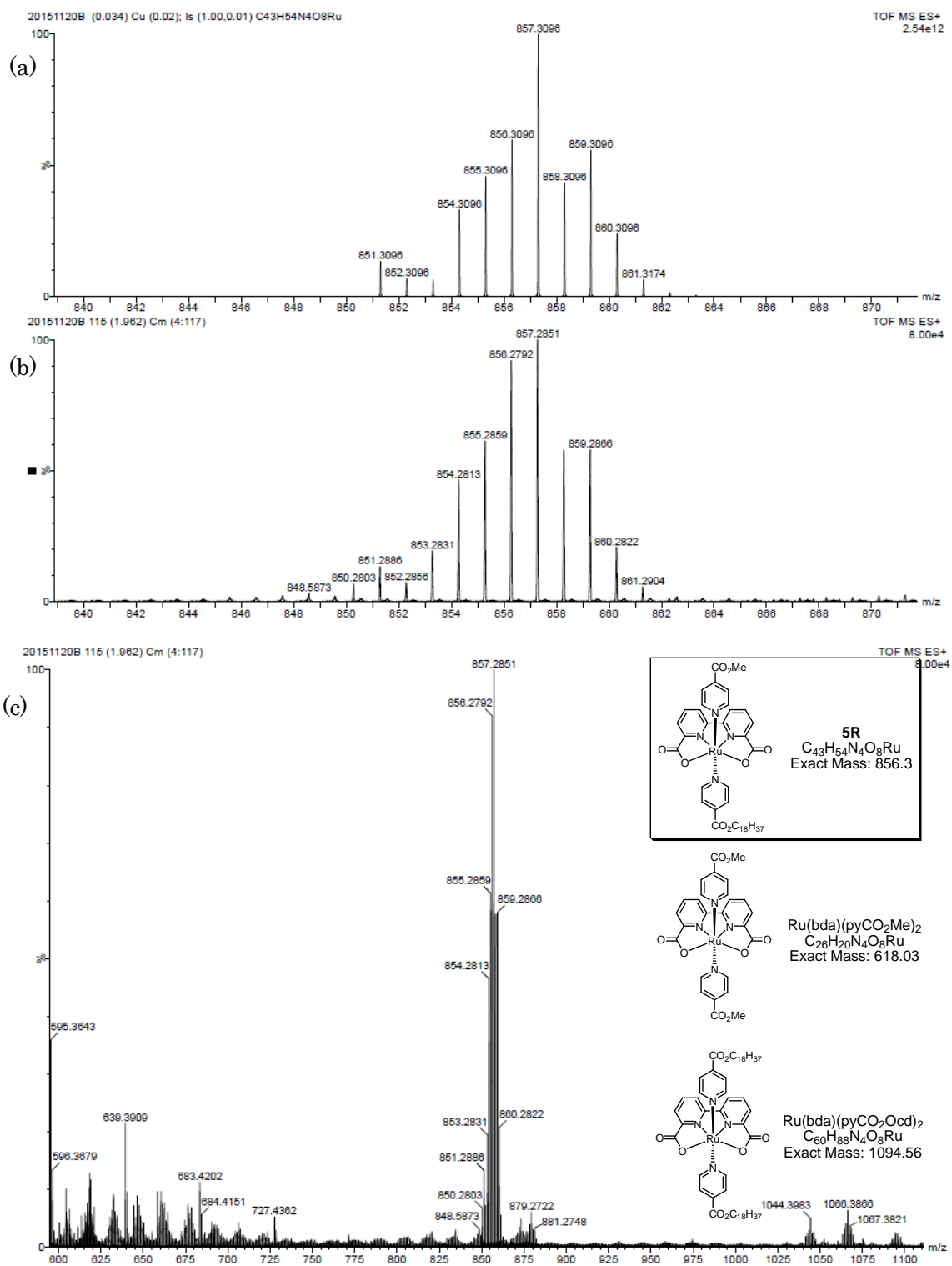


Figure 3-1. ESI-MS spectra of Ru(bda)(pyCO₂Me)(pyCO₂Ocd) (**5R**): (a) simulated spectrum for **5R**+H⁺; spectra measured in (b) m/z = 840–870 and (c) 600–1100 regions.

3.2.2 Photophysical properties

UV-Vis absorption spectrum of **5R** was measured in CHCl₃, which is shown in Fig. 3-2 (red line). The absorption maximal wavelengths and molar extinction coefficients are listed in Table 3-1. For comparison, the absorption spectrum of Ru(bda)(pyCO₂Me)₂ (**5**) and the detailed data are also shown in Fig. 3-2 (blue line) and Table 3-1, respectively. The absorption spectrum of **5R** was almost identical to that of **5**, indicating that the long alkyl chain of **5R** does not influence its photophysical property.

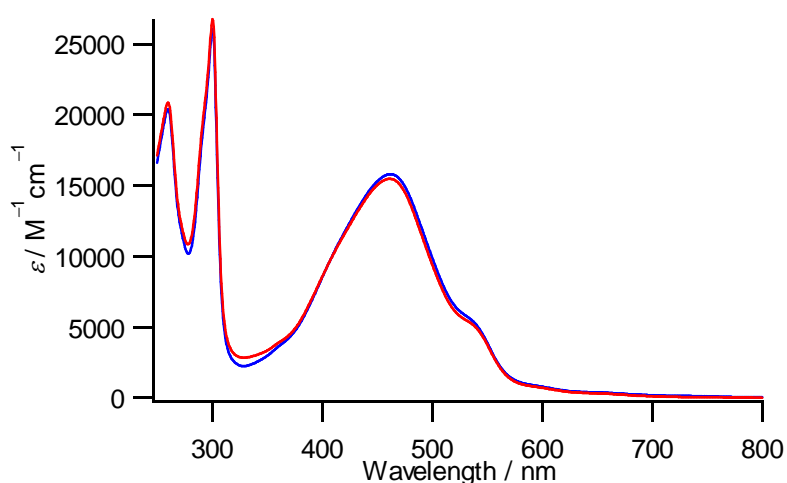


Figure 3-2. UV-Vis absorption spectrum of the complex Ru(bda)(pyCO₂Me)(pyCO₂Ocd) (**5R**, red) in CHCl₃. The spectrum of the complex Ru(bda)(pyCO₂Me)₂ (**5**, blue) in CHCl₃ is also shown for comparison.

Table 3-1. Photophysical properties of Ru(bda)(pyCO₂Me)(pyCO₂Ocd) (**5R**) and Ru(bda)(pyCO₂Me)₂ (**5**).

Complex	$\lambda_{\text{abs}}^a / \text{nm}$ ($\epsilon_{\text{max}} / 10^3 \text{ M}^{-1} \text{ cm}^{-1}$)
Ru(bda)(pyCO ₂ Me)(pyCO ₂ Ocd) (5R)	301 (26.7), 462 (15.5), 540sh (4.94)
Ru(bda)(pyCO ₂ Me) ₂ (5)	301 (26.1), 462 (15.8), 540sh (5.20)

^aWavelengths of absorption maxima recorded in CHCl₃.

3.2.3 Cyclic voltammetric measurement

Electrochemical property of complex **5R** was investigated by cyclic voltammetry in CH_2Cl_2 purged by N_2 . The cyclic voltammogram of **5R** is shown in Fig. 3-3 as a red line along with that of complex **5** as a blue line. As summarized in Table 3-2, the oxidation potential of **5R** was 0.06 V (vs. Fc^+/Fc), which is similar to that of **5**. This implies that the long alkyl chain of **5R** has almost no influence on its electrochemical property. Therefore, the catalytic property of **5R** can be assumed to be nearly the same as that of complex **5**.

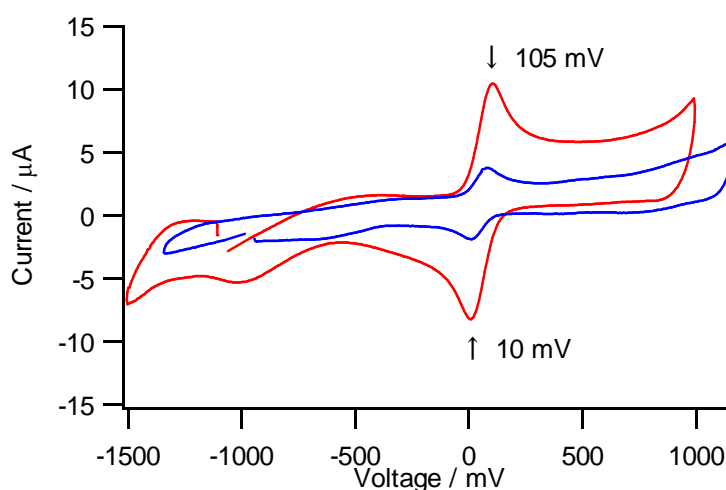


Figure 3-3. Cyclic voltammograms of $\text{Ru}(\text{bda})(\text{pyCO}_2\text{Me})(\text{pyCO}_2\text{Ocd})$ (**5R**, red) and $\text{Ru}(\text{bda})(\text{CO}_2\text{Me})_2$ (**5**, blue) recorded in CH_2Cl_2 (vs. Fc^+/Fc).

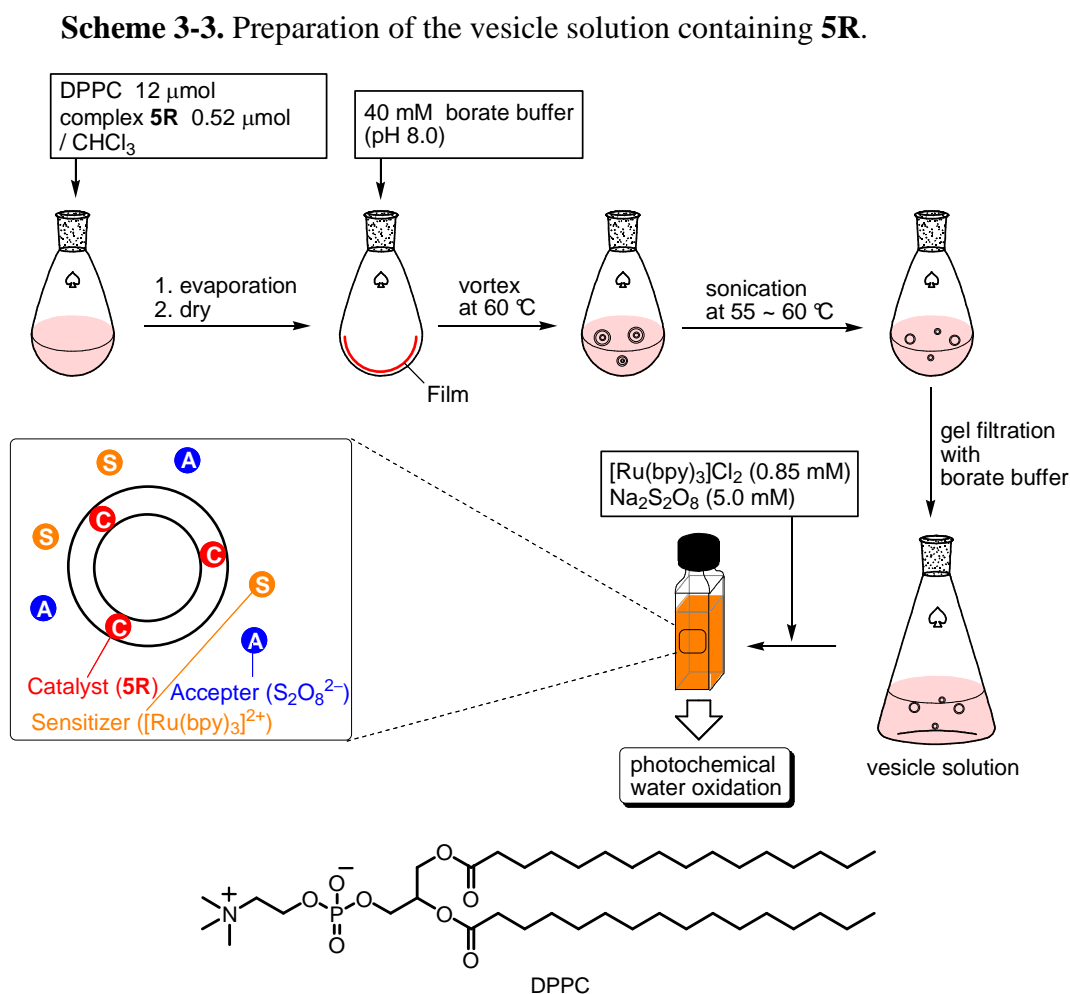
Table 3-2. Oxidation potentials of $\text{Ru}(\text{bda})(\text{pyCO}_2\text{Me})(\text{pyCO}_2\text{Ocd})$ (**5R**) and $\text{Ru}(\text{bda})(\text{pyCO}_2\text{Me})_2$ (**5**).

Complex	$E_{1/2(\text{oxdn})}^a / \text{V}$
$\text{Ru}(\text{bda})(\text{pyCO}_2\text{Me})(\text{pyCO}_2\text{Ocd})$ (5R)	0.06
$\text{Ru}(\text{bda})(\text{pyCO}_2\text{Me})_2$ (5)	0.05

^ain CH_2Cl_2 , vs. Fc^+/Fc

3.2.4 Incorporation into the vesicle membranes

The procedure for the preparation of vesicle solution containing complex **5R** is illustrated in Scheme 3-3. The chloroform solution of complex **5R** and 1,2-dipalmitoyl-*sn*-glycero-3-phosphocholine (DPPC) was evaporated, and the residue was dried under reduced pressure overnight to form a thin film. Then, borate buffer (40 mM, pH 8.0) was added to the film in the flask, and the flask was vortexed at 60 °C. After that, the resulting suspension was sonicated to make small unilamellar vesicles of even sizes. Compounds not incorporated into vesicles were removed by gel filtration to give the vesicle solution. To the vesicle solution, [Ru(bpy)₃]Cl₂ as a sensitizer and Na₂S₂O₈ as a sacrificial electron acceptor were added, and after degassing by Ar-bubbling, the solution was used for the photochemical water oxidation experiment.



UV-Vis absorption spectrum was measured for the vesicle solution, but the recorded spectrum of the vesicle solution was obviously different from that of complex **5R** in chloroform: a broad band at ca. 680 nm was observed in the spectrum of the vesicle solution (Fig. 3-4, blue line). This absorption band likely originates from the Ru(III) species, generated by the oxidation of **5R** by air in the course of the vesicle preparation. It is known that $[\text{Ru}(\text{bpy})_3]^{3+}$ has a characteristic absorption in the long wavelength region ($\lambda_{\text{max}} = 675 \text{ nm}$, $\epsilon = 409 \text{ M}^{-1} \text{ cm}^{-1}$ in acetonitrile).³ Moreover, the Ru(II) species of the $\text{Ru}(\text{bda})\text{L}_2$ ($\text{L} = N$ -heteroaromatic ligand) complexes have been reported to be readily oxidized by air to become the Ru(III) species.⁴ In addition, I found preliminarily that the color of the red-colored aqueous solution of $\text{Ru}(\text{bda})(\text{pyMe})_2$ turned to green in exposure to air, while the green solution changes the color to red by the addition of sodium ascorbate, which is known as a common reductant of Ru(III) species.

Therefore, the concentration of complex **5R** incorporated into vesicles was determined by the following procedure: to the vesicle solution containing **5R**, sodium ascorbate was added, and subsequently methanol was added to dissolve the vesicles completely in the aqueous solution. The solution was then extracted with dichloromethane. The organic layer was dried over Na_2SO_4 and evaporated. The residue was dissolved in chloroform, and UV-Vis absorption spectrum of this solution was measured. The spectrum of the extract in chloroform is also shown in Fig. 3-4 (green line), which indicates that the spectrum of the extract was almost identical to that of **5R** recorded in chloroform (red line). In this way, the concentration of **5R** embedded into vesicles was able to be estimated using the absorbance at 460 nm of the extract and the molar extinction coefficient at the corresponding wavelength observed in the spectrum of **5R** in chloroform.

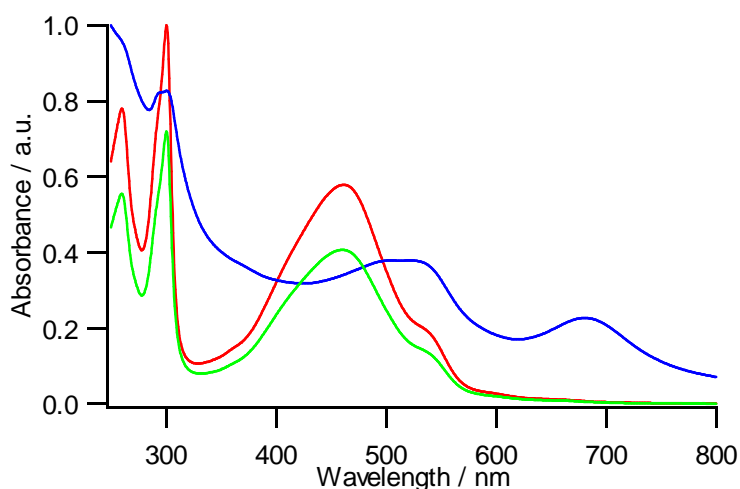


Figure 3-4. UV-Vis absorption spectra of the vesicle solution containing **5R** (blue), and the chloroform solution of **5R** extracted from the vesicle solution treated with sodium ascorbate and methanol (green). A red line shows UV-Vis absorption spectrum of **5R** recorded in chloroform.

To gain evidence supporting that complex **5R** is incorporated into the vesicle membranes, the partition coefficient of **5R** in 1-octanol/water extraction was determined preliminarily. Complex **5R** was dissolved in octanol, and then the solution was extracted with the same volume of water. UV-Vis absorption spectra of the octanol solution before and after the extraction are shown in Fig. 3-5a, and the spectrum of the aqueous solution after the extraction is also shown in Fig. 3-5b. The absorption spectra of **5R** in the octanol solution and aqueous solution were slightly different from each other because the absorption peaks assigned to the MLCT transition tend to shift largely by the change in the solvent polarity. The partition coefficient, P_{ow} , which is defined as the ratio of molar concentration in octanol to that in water, was estimated from the difference in the absorbance at 456 nm in octanol before and after the extraction. The absorbance at 456 nm decreased from 0.538 to 0.476 by the extraction, indicating that 11.6% of complex **5R** was dissolved in water. On the basis of these observations, the P_{ow} value was calculated to be $P_{ow} = 7.62$. Therefore, it is reasonable to think that complex **5R** is sufficiently hydrophobic, so that most of **5R** are incorporated into the membranes of vesicles.

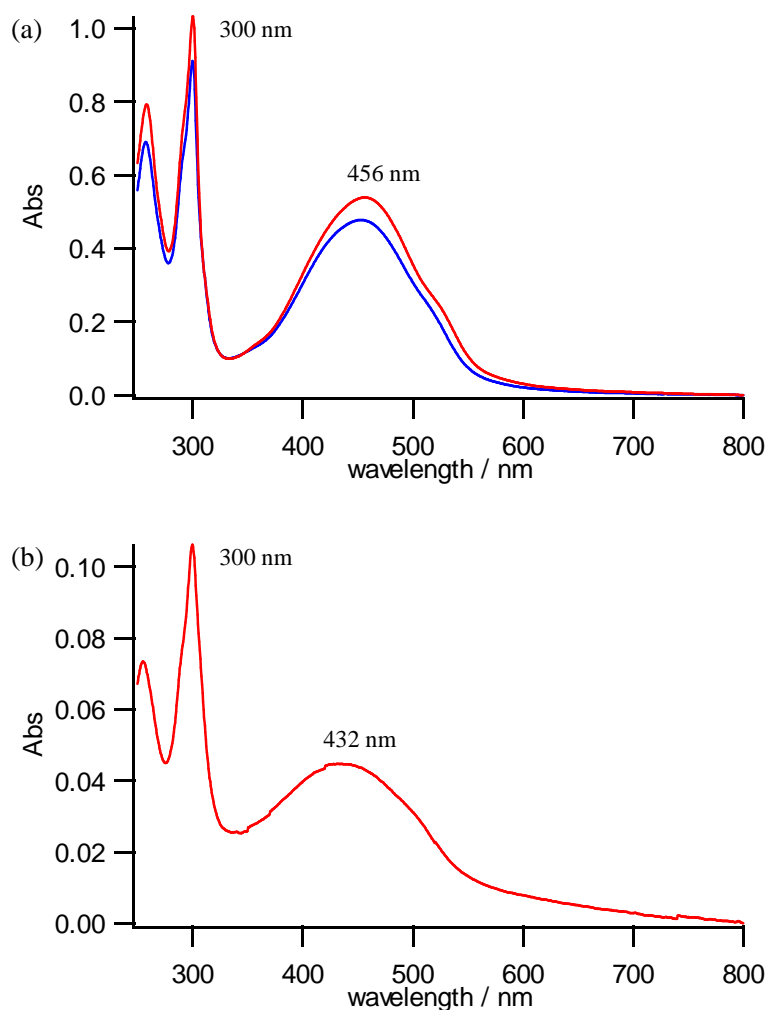


Figure 3-5. UV-Vis absorption spectra of (a) the octanol solution before extraction (red) and after extraction (blue), and (b) the aqueous solution after extraction.

I attempted the incorporation of $\text{Ru}(\text{bda})(\text{pyCO}_2\text{Ocd})_2$ into vesicle membranes, but the vesicle solution obtained according to the procedure described above was considerably turbid, the UV-Vis spectrum of which is shown in Fig. 3-6. This solution was not suitable for the photochemical experiments. In addition, preparation of the vesicle solution containing $\text{Ru}(\text{bda})(\text{pyCO}_2\text{Me})_2$ was tried. However, by the gel filtration chromatography, a fraction containing large amounts of the complex was separated from the vesicle solution, and UV-Vis absorption spectrum of the vesicle solution obtained (Fig. 3-7) revealed that few amounts of $\text{Ru}(\text{bda})(\text{pyCO}_2\text{Me})_2$ were incorporated into

vesicles. This result demonstrates that the hydrophobic Ocd substituent is essential for incorporation of the Ru complex into vesicle membranes.

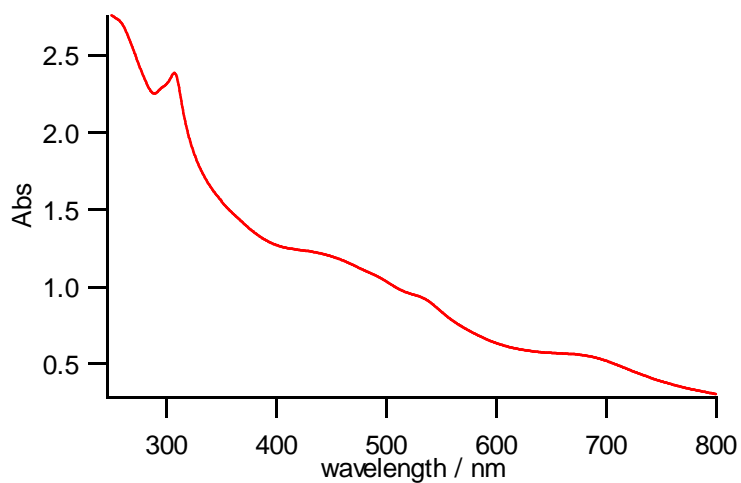


Figure 3-6. UV-Vis absorption spectrum of the vesicle solution containing Ru(bda)(pyCO₂Ocd)₂.

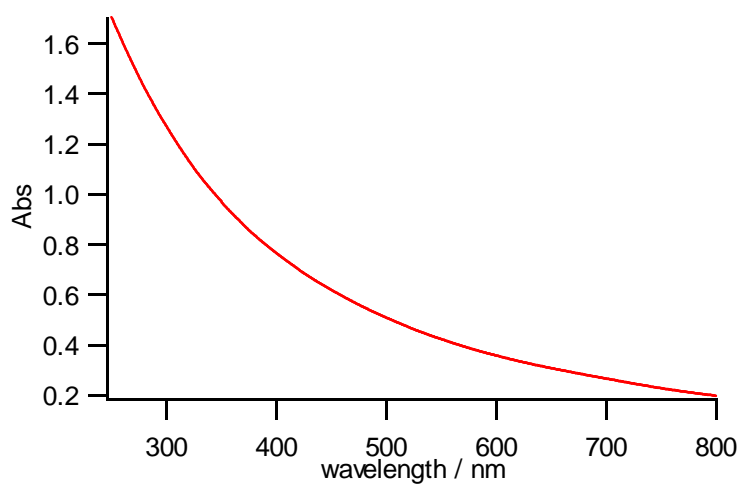


Figure 3-7. UV-Vis absorption spectrum of the vesicle solution containing Ru(bda)(pyCO₂Me)₂.

3.2.5 Photochemical water oxidation

Photochemical water oxidation experiments were carried out using the vesicle solution containing $[\text{Ru}(\text{bpy})_3]^{2+}$, $\text{S}_2\text{O}_8^{2-}$, and complex **5R** prepared according to the procedure described in §3.2.4. In this system, it is expected that $[\text{Ru}(\text{bpy})_3]^{3+}$ is generated in the outer aqueous phase through oxidative quenching of $[\text{Ru}(\text{bpy})_3]^{2+}$ in its excited state by $\text{S}_2\text{O}_8^{2-}$ and oxidation of $[\text{Ru}(\text{bpy})_3]^{2+}$ in its ground state by $\text{SO}_4^{\bullet-}$. Subsequently, $[\text{Ru}(\text{bpy})_3]^{3+}$ oxidizes complex **5R** embedded into the vesicle membranes, and the oxidized complex initiates the catalytic cycle for oxidation of water to oxygen.

When the vesicle solution containing $[\text{Ru}(\text{bpy})_3]^{2+}$ (0.85 mM) and $\text{S}_2\text{O}_8^{2-}$ (5.0 mM) in the outer aqueous phase and complex **5R** (ca. 20 μM) embedded into the vesicle membranes was photoirradiated ($\lambda > 390$ nm), evolution of oxygen (36.4 μL) was observed by GC analysis after 120 min of irradiation. This result proves that the photochemical water oxidation successfully proceeded in the vesicular system using the newly-synthesized Ru complex **5R** as a catalyst. The turnover number (TON) with respect to the catalyst was calculated to be 25.1.

The time course of TON of the photochemical water oxidation is shown in Fig. 3-8 (red line). As shown in the figure, the oxygen evolution rate was almost constant within initial 30 min, but the reaction practically ceased after 120 min of irradiation. The cessation of the oxygen generation is probably due to a decrease in pH of the solution during the irradiation. In fact, pH of the vesicle solution lowered from 8.0 to 2.9 after irradiation for 120 min. It has been reported that the reaction rate is considerably reduced in low pH and partially recovered by the addition of base in a homogeneous photochemical water oxidation system using $\text{Ru}(\text{bda})(\text{pyMe})_2$.⁵

Photochemical water oxidation experiment using $\text{Ru}(\text{bda})(\text{pyCO}_2\text{Me})_2$ (**5**) in the homogeneous solution was also conducted under the photochemical conditions identical to those in the vesicular system. The time profile of TON is also shown in Fig. 3-8 (blue line), indicating that both the TON after irradiation for 120 min and the initial turnover frequency (TOF) estimated for 30 min irradiation with respect to the catalyst in the vesicular system are more than twice as much as those in the homogeneous system. In

addition to the GC analysis, UV-Vis absorption spectra were also measured in the course of the photochemical water oxidation experiment (Fig. 3-9). As shown in the figure, in the vesicular system, an absorption band characteristic of Ru(III) species was observed at 680 nm, and its absorption intensity was notably larger than that in the homogeneous system. This indicates that the steady-state concentration of the Ru(III) species is much higher in the vesicular system than in the homogeneous solution.

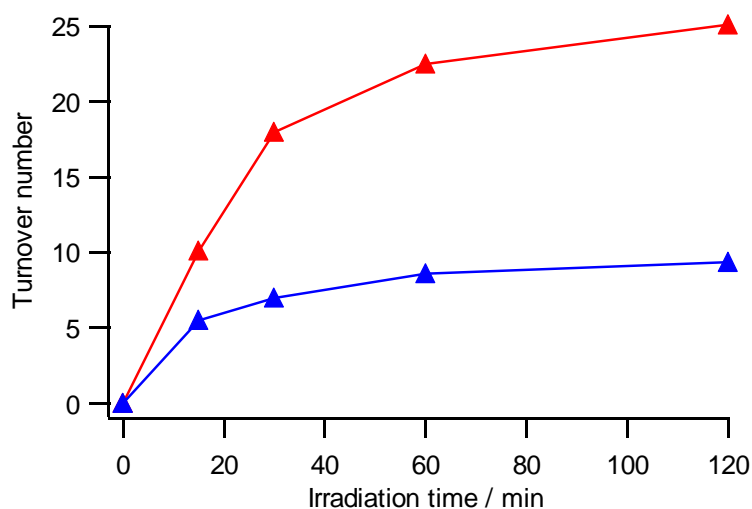


Figure 3-8. The time course of the turnover number of the photochemical water oxidation with respect to the catalyst using $[\text{Ru}(\text{bpy})_3]\text{Cl}_2$ (0.85 mM) and $\text{Na}_2\text{S}_2\text{O}_8$ (5.0 mM) in borate buffer (40 mM, pH 8.0): DPPC vesicular system ($[\mathbf{5R}] = 19.8 \mu\text{M}$), red; homogeneous system ($[\mathbf{5}] = 15.9 \mu\text{M}$), blue.

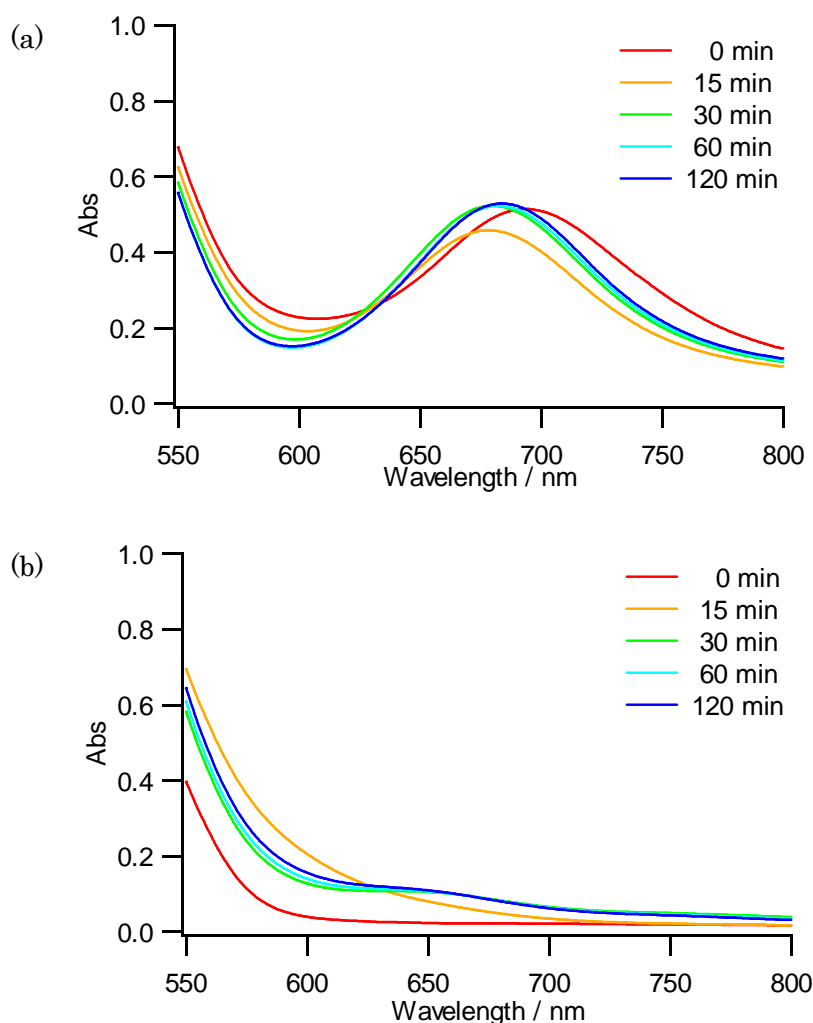


Figure 3-9. UV-Vis absorption spectral change in the photochemical water oxidation using $[\text{Ru}(\text{bpy})_3]\text{Cl}_2$ (0.85 mM) and $\text{Na}_2\text{S}_2\text{O}_8$ (5.0 mM) in borate buffer (40 mM, pH 8.0) (a) in the vesicular system ($[\mathbf{5R}] = 19.8 \mu\text{M}$) and (b) in the homogeneous system ($[\mathbf{5}] = 15.9 \mu\text{M}$): after 0 (red), 15 (orange), 30 (light green), 60 (light blue), 120 min (blue) of irradiation ($\lambda > 390 \text{ nm}$).

3.2.6 Dependence on the concentration of the sensitizer

To obtain more information about the photochemical water oxidation in the vesicular system, the dependence of the initial oxygen evolution rate on the concentrations of the sensitizer, the electron acceptor, and the catalyst was investigated.

First, the dependence on the sensitizer concentration was examined. Using various concentrations of the sensitizer, the photochemical water oxidation experiments were

carried out under the conditions identical to those stated in §3.2.5 except for the sensitizer concentration. The amount of oxygen evolved after 30 min of photoirradiation is shown in Fig. 3-10 as a function of the sensitizer concentration. The initial oxygen evolution rate increases with an increase in the sensitizer concentration, [sens], but it is saturated in [sens] > 0.5 mM.

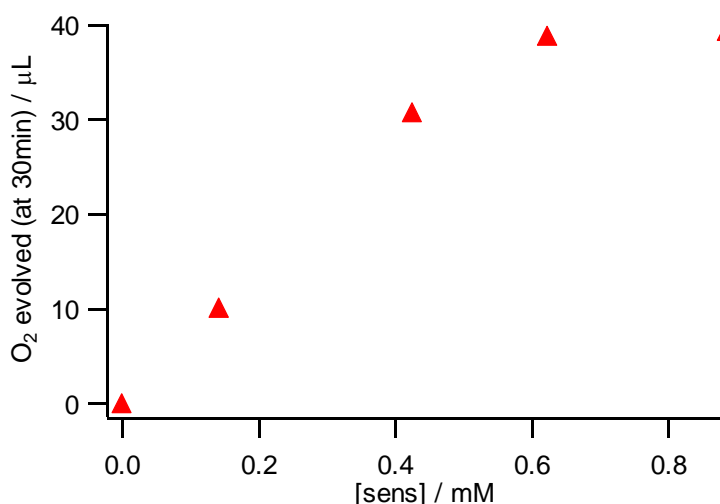


Figure 3-10. Dependence of the amount of oxygen evolved in the photochemical water oxidation in the vesicle solution on the concentration of [Ru(bpy)₃]Cl₂ in the outer aqueous solution (5.0 mM Na₂S₂O₈ in outer aqueous solution, ca. 20 μM complex **5R** embedded into DPPC vesicle membranes, in borate buffer (40 mM, pH 8.0)).

In order to understand these results, the intensity of light absorbed by the sensitizer was calculated. The UV-Vis absorption spectrum of [Ru(bpy)₃]²⁺ in aqueous borate buffer is shown in Fig. 3-11a (red line). The light intensity absorbed by the sensitizer, I_{abs} , can be calculated by Eq. 3.1,

$$I_{\text{abs}} = \int I_{\text{in}}(\lambda)(1 - 10^{-\varepsilon(\lambda)cl})d\lambda \quad (3.1)$$

where $I_{\text{in}}(\lambda)$, $\varepsilon(\lambda)$, c and l represent the incident light intensity, the molar extinction coefficient and the concentration of [Ru(bpy)₃]²⁺, and the length of light path, respectively.

Assuming that the light intensity of a Xe lamp is independent of wavelength in the visible region, $I_{in}(\lambda)$ is considered to be directly proportional to the transparency of the optical filter, which is shown in Fig. 3-11a (blue line). Hence, the relative value of I_{abs} , $I_{abs}(\text{rel})$, is calculated by the following equation using the transparency of the optical filter, $T(\lambda)$.

$$I_{abs}(\text{rel}) = \int T(\lambda)(1 - 10^{-\epsilon(\lambda)cl})d\lambda \quad (3.2)$$

The calculated $I_{abs}(\text{rel})$ value normalized so that the $I_{abs}(\text{rel})$ equals 1 at $c = 1$ mM is shown in Fig. 3-11b as a function of the sensitizer concentration ($c = [\text{sens}]$). From this graph, it is found that the light intensity absorbed by the sensitizer is almost saturated in $[\text{sens}] > 0.5$ mM, indicating that an increase in the concentration of the sensitizer above 0.5 mM has practically no effect on the photochemical reaction rate. Thus, the saturation of the amount of O_2 evolved shown in Fig. 3-10 is reasonably explained in terms of the saturation of the light intensity absorbed by the sensitizer.

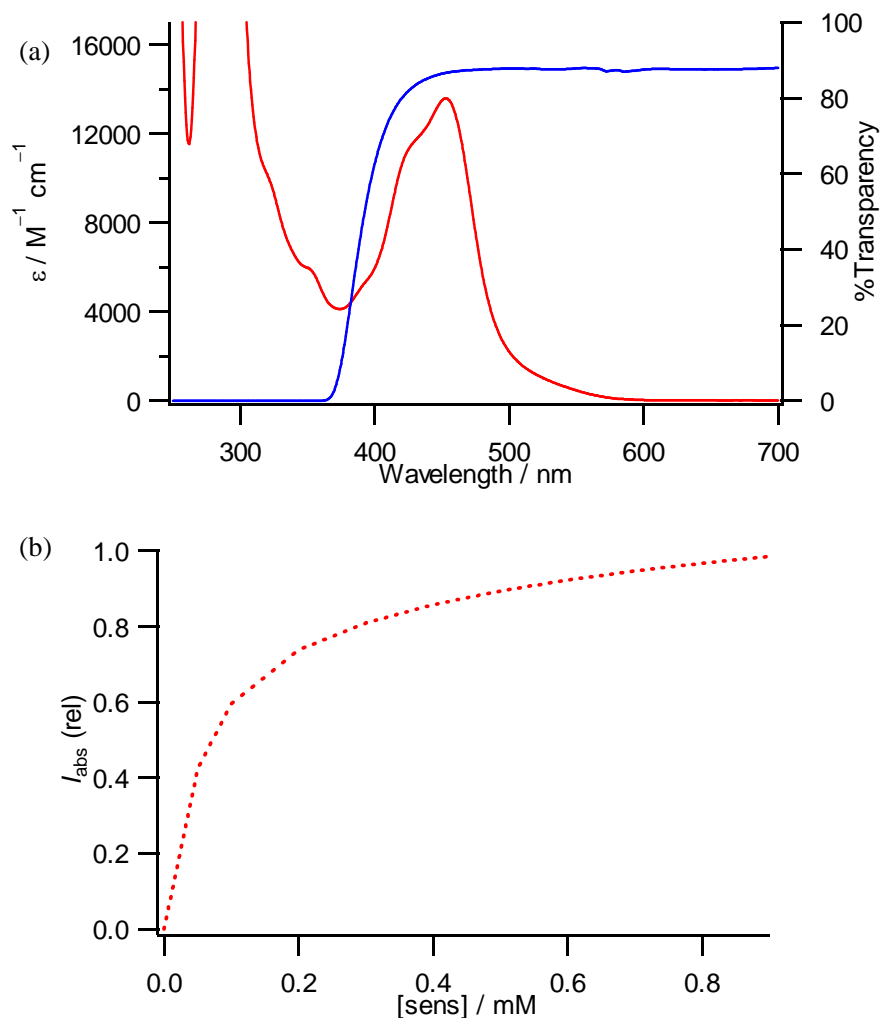


Figure 3-11. (a) The UV-Vis absorption spectrum of $[\text{Ru}(\text{bpy})_3]^{2+}$ in borate buffer (40 mM, pH 8.0, red) and the transparency of the optical filter employed in the irradiation experiment ($\lambda > 390$ nm, blue). (b) The calculated relative intensity of the light absorbed by the sensitizer as a function of the sensitizer concentration.

3.2.7 Dependence on the concentration of the electron acceptor

Next, the dependence of the initial oxygen evolution rate on the concentration of the electron acceptor, $\text{S}_2\text{O}_8^{2-}$, was examined. Fig. 3-12 shows the amount of oxygen evolved after irradiation for 30 min as a function of $[\text{S}_2\text{O}_8^{2-}]$. In $[\text{S}_2\text{O}_8^{2-}] > 20$ mM, formation of precipitate was observed after photoirradiation, which is presumed to be responsible for the decrease in the oxygen evolution rate in the high concentration region. In the low concentration region in $[\text{S}_2\text{O}_8^{2-}] < 20$ mM, it was found that the oxygen evolution rate is

saturated in $[\text{S}_2\text{O}_8^{2-}] > 5 \text{ mM}$. To elucidate the reason for the saturation of the oxygen evolution rate and to gain information about the reaction mechanism, emission quenching experiments of $[\text{Ru}(\text{bpy})_3]^{2+}$ in borate buffer were carried out, the results of which will be described in the next section.

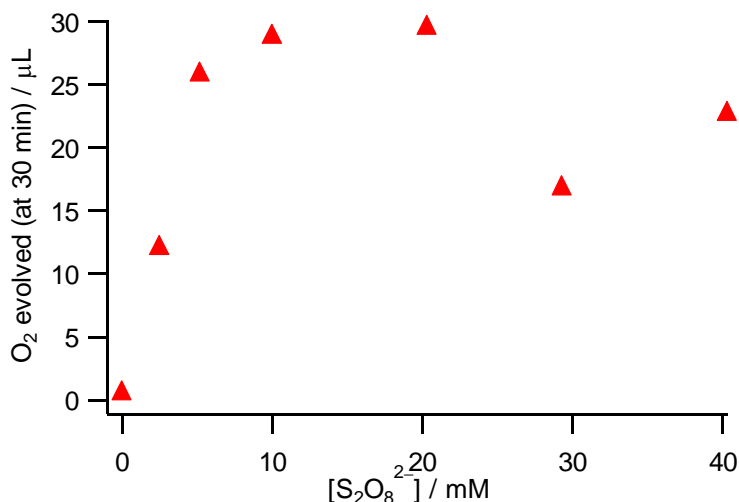


Figure 3-12. Dependence of the amount of oxygen evolved in the photochemical water oxidation in vesicles on the concentration of $\text{Na}_2\text{S}_2\text{O}_8$ in the outer aqueous solution (0.85 mM $[\text{Ru}(\text{bpy})_3]\text{Cl}_2$ in outer aqueous solution, ca. 20 μM complex **5R** embedded into DPPC vesicle membranes, in 40 mM borate buffer (pH 8.0)).

3.2.8 Emission quenching

Emission quenching of $[\text{Ru}(\text{bpy})_3]^{2+}$ in borate buffer (40 mM, pH 8.0) was examined using a decrease in the emission intensity with the addition of quencher. As shown in Fig. 3-13a, the emission of $[\text{Ru}(\text{bpy})_3]^{2+}$ was found to be quenched by the addition of $\text{S}_2\text{O}_8^{2-}$. However, decomposition of $[\text{Ru}(\text{bpy})_3]^{2+}$ was also observed in UV-Vis absorption spectrum (Fig. 3-13b), although this complex did not decompose in 1:1 acetonitrile/borate buffer (see §2.2.7). Bonchio *et al.* have reported that the oxidized species of the sensitizer, $[\text{Ru}(\text{bpy})_3]^{3+}$, is more stable in mixed solvent containing acetonitrile.⁶ In contrast, the decomposition of $[\text{Ru}(\text{bpy})_3]^{3+}$ is relatively faster in an aqueous solution without acetonitrile. Therefore, the degradation of $[\text{Ru}(\text{bpy})_3]^{2+}$ observed in the quenching experiment is attributable to the decomposition of

$[\text{Ru}(\text{bpy})_3]^{3+}$, which is generated by the oxidative quenching of $([\text{Ru}(\text{bpy})_3]^{2+})^*$ by $\text{S}_2\text{O}_8^{2-}$.

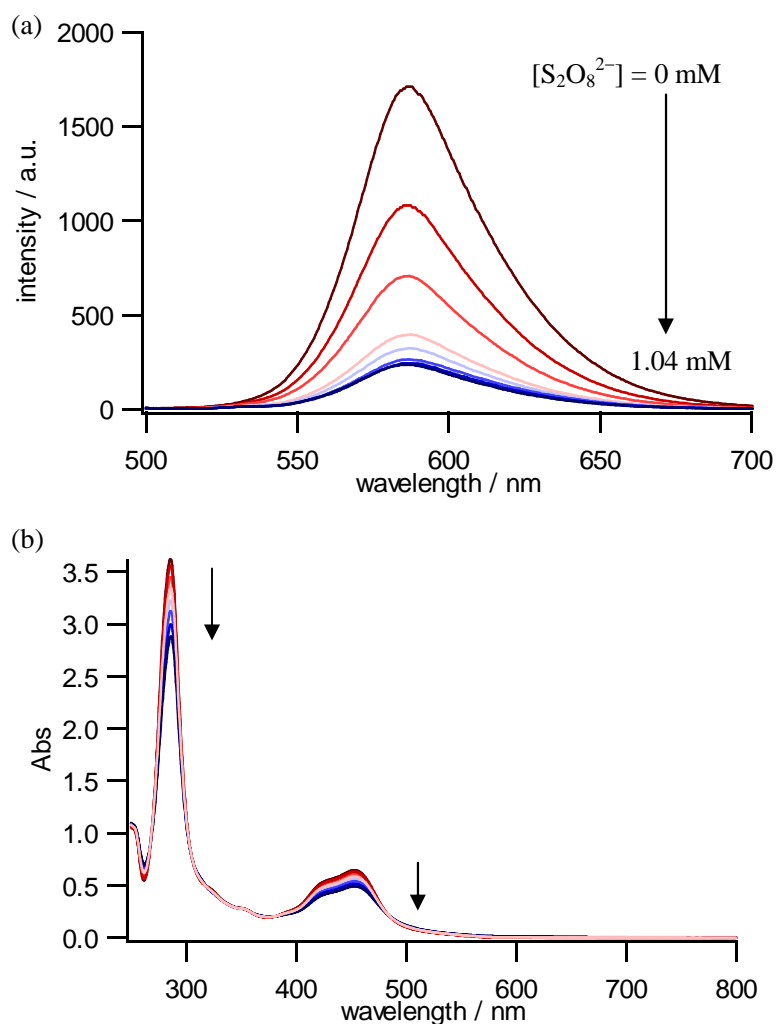


Figure 3-13. (a) A decrease in emission intensity and (b) UV-Vis spectral change after each emission measurement of $50.1 \mu\text{M}$ $[\text{Ru}(\text{bpy})_3]\text{Cl}_2$ in borate buffer (40 mM, pH 8.0) by the addition of $\text{Na}_2\text{S}_2\text{O}_8$ ($\lambda_{\text{ex}} = 450 \text{ nm}$).

Since the quenching experiment using emission intensity was found to be difficult because of the decomposition of $[\text{Ru}(\text{bpy})_3]^{2+}$, the emission quenching experiment was then carried out by emission lifetime measurement in borate buffer. The decay profile of $[\text{Ru}(\text{bpy})_3]^{2+}$ emission in air-saturated borate buffer is shown in Fig. 3-14, which is satisfactorily fitted to a single exponential function to give an emission lifetime of $\tau_0 =$

358 ns. A decrease in the emission lifetime was observed by the addition of $\text{S}_2\text{O}_8^{2-}$ (Fig. 3-15a). As shown in Fig. 3-15b, decomposition of $[\text{Ru}(\text{bpy})_3]^{2+}$ was not observed in the course of the lifetime measurement. The emission lifetimes calculated by single exponential fitting are listed in Table 3-3. By the Stern-Volmer treatment as stated in the previous section (see §2.2.7), a quenching constant was estimated as $k_q\tau_0 = 739 \text{ M}^{-1}$ (Fig. 3-16). Hence, using the lifetime of $[\text{Ru}(\text{bpy})_3]^{2+}$ in air-saturated borate buffer ($\tau_0 = 358 \text{ ns}$), the quenching rate constant was calculated to be $k_q = 2.06 \times 10^9 \text{ M}^{-1} \text{ s}^{-1}$.

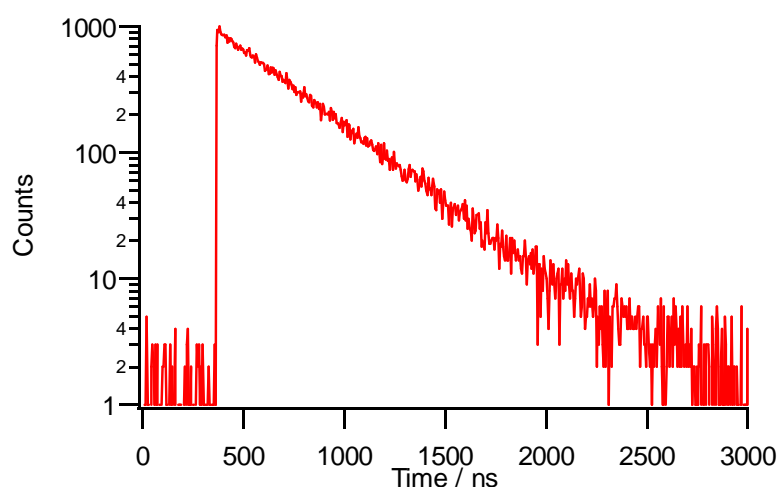


Figure 3-14. Time profile of $[\text{Ru}(\text{bpy})_3]^{2+}$ emission in air-saturated borate buffer (40 mM, pH 8.0). The concentration of $[\text{Ru}(\text{bpy})_3]^{2+}$ is 52.4 μM : Excitation, 405 nm; Emission, 605 nm. The lifetime of 358 ns was obtained by the single exponential fitting.

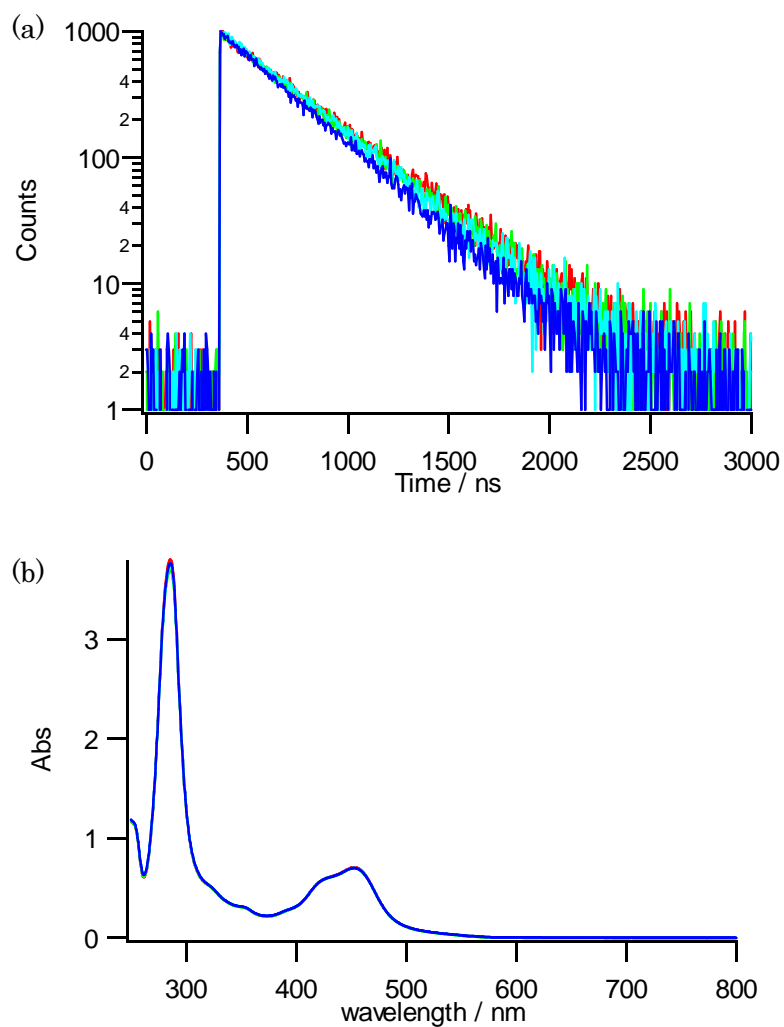


Figure 3-15. (a) The time profiles of emission and (b) UV-Vis absorption spectra after each emission lifetime measurement of 52.4 μM [Ru(bpy)₃]Cl₂ in borate buffer (40 mM, pH 8.0) in the presence of Na₂S₂O₈: [S₂O₈²⁻] = 0 (red), 53.7 (light green), 105 (light blue), 200 μM (blue).

Table 3-3. Emission lifetimes of $[\text{Ru}(\text{bpy})_3]^{2+}$ in the presence of $\text{S}_2\text{O}_8^{2-}$ at various concentrations.^a

$[\text{S}_2\text{O}_8^{2-}] / \mu\text{M}$	τ^b / ns
0	358
53.7	340
105	330
200	311

^a52.4 μM $[\text{Ru}(\text{bpy})_3]\text{Cl}_2$ in borate buffer (40 mM, pH 8.0); excitation, 405 nm; emission, 615 nm.

^bEmission lifetime.

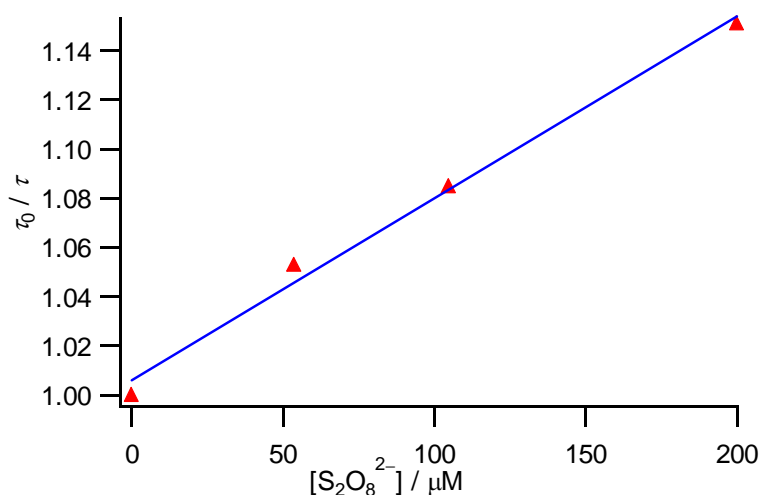


Figure 3-16. Stern-Volmer plot for quenching of the emission of $[\text{Ru}(\text{bpy})_3]^{2+}$ by $\text{S}_2\text{O}_8^{2-}$ using the emission lifetime ($[\text{Ru}(\text{bpy})_3]^{2+} = 52.4 \mu\text{M}$ in borate buffer (40 mM, pH 8.0), $\lambda_{\text{ex}} = 405 \text{ nm}$, $\lambda_{\text{em}} = 615 \text{ nm}$). The least-square analysis of the plot yields a quenching constant, $k_q\tau_0$, of 739 M^{-1} .

The quenching of $[\text{Ru}(\text{bpy})_3]^{2+}$ emission by $\text{Ru}(\text{bda})(\text{pyCO}_2\text{Me})_2$ (**5**) was also performed using emission intensity in borate buffer. As noted in §2.2.7, complex **5** has an absorption band near the excitation wavelength (450 nm). In fact, as shown in Fig. 3-17a, the addition of the quencher **5** caused an increase in the absorbance of UV-Vis spectrum of the $[\text{Ru}(\text{bpy})_3]^{2+}$ solution, indicating the correction in the absorption is required in the emission quenching experiment. The intensity of $[\text{Ru}(\text{bpy})_3]^{2+}$ emission decreased by the addition of complex **5** (Fig. 3-17b), and after the correction using Eq. 2.2 (see §2.2.7),

the emission intensity ratios, I_0/I , where I_0 and I are the emission intensity in the absence and the presence of quencher, respectively, were treated by the Stern-Volmer equation. As shown in Fig. 3-17c, the Stern-Volmer plot gives a good straight line, yielding a quenching constant, $k_q'\tau_0$, of 3400 M^{-1} . Since the emission lifetime of $[\text{Ru}(\text{bpy})_3]^{2+}$ in air-saturated borate buffer is $\tau_0 = 358 \text{ ns}$, the rate constant for quenching by complex **5** is evaluated to be $k_q' = 9.50 \times 10^9 \text{ M}^{-1} \text{ s}^{-1}$.

The quenching efficiency, η_q , which is defined by Eq. 2.3 (see §2.2.9) was estimated using k_q , k_q' and τ_0 in degassed borate buffer. The emission lifetime of $[\text{Ru}(\text{bpy})_3]^{2+}$ in degassed borate buffer (40 mM, pH 8.0) was determined by the decay profile of the emission (Fig. 3-18) to be $\tau_0 = 560 \text{ ns}$. As a result, the quenching efficiencies by $\text{S}_2\text{O}_8^{2-}$ and complex **5** were $\eta_q(\text{S}_2\text{O}_8^{2-}) = 84.1\%$ and $\eta_q(\mathbf{5}) = 1.3\%$, respectively, under the conditions employed in the photochemical water oxidation experiments ($[\text{S}_2\text{O}_8^{2-}] = 5.0 \text{ mM}$, $[\mathbf{5}] = 17 \text{ }\mu\text{M}$). Moreover, it has been reported that the rate constant for quenching of the emission of the sensitizer embedded in vesicle membranes is lower than that in the homogeneous solution by more than one order of magnitude.⁷ So it is unlikely that the excited state of $[\text{Ru}(\text{bpy})_3]^{2+}$ in the outer aqueous phase is quenched by complex **5R** embedded into vesicle membranes.

The quenching efficiency by $\text{S}_2\text{O}_8^{2-}$ calculated by Eq. 2.3 is shown in Fig. 3-19 as a function of $[\text{S}_2\text{O}_8^{2-}]$. From this graph, the quenching efficiency by $\text{S}_2\text{O}_8^{2-}$ appears to be saturated in $[\text{S}_2\text{O}_8^{2-}] > 5 \text{ mM}$. On the basis of these data, the observation that the oxygen evolution rate was saturated in $[\text{S}_2\text{O}_8^{2-}] > 5 \text{ mM}$ (Fig. 3-12) is reasonably explained by that the excited sensitizer is almost completely quenched by $\text{S}_2\text{O}_8^{2-}$ in the concentration range.

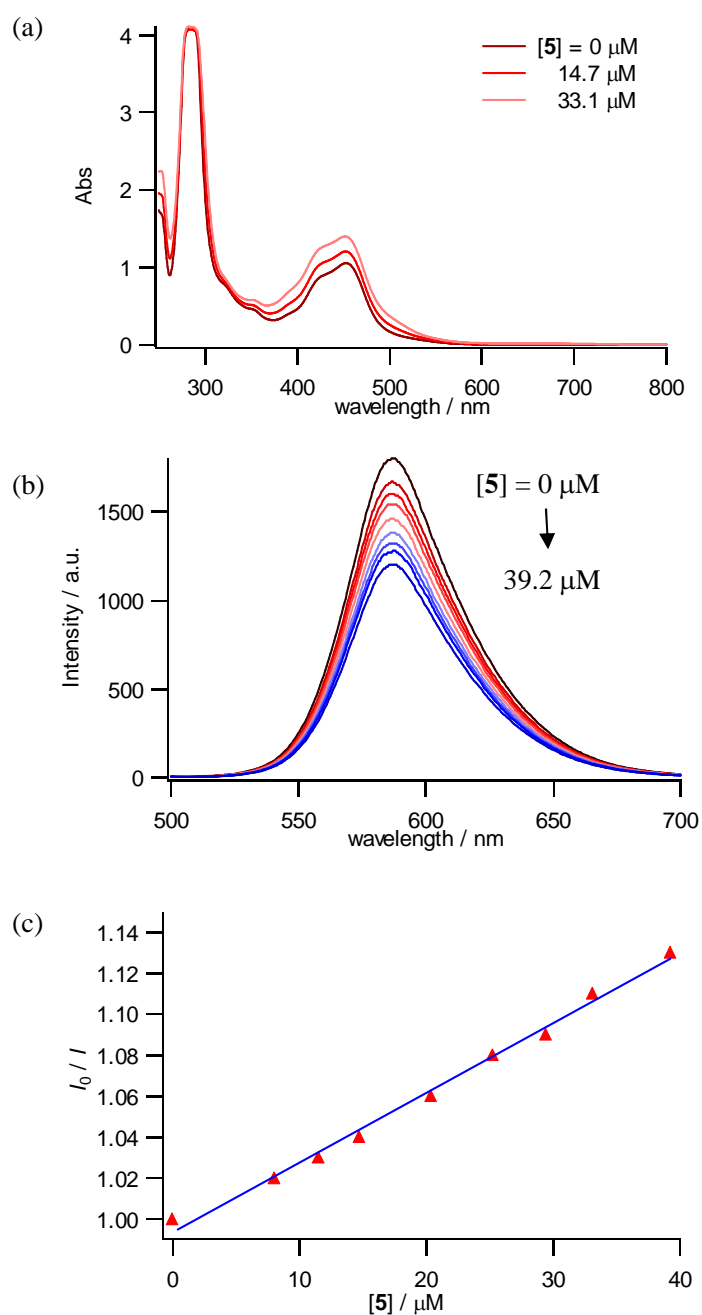


Figure 3-17. Quenching of $[\text{Ru}(\text{bpy})_3]^{2+}$ emission by $\text{Ru}(\text{bda})(\text{pyCO}_2\text{Me})_2$ (**5**). (a) UV-Vis absorption spectral change and (b) decrease in the intensity of $[\text{Ru}(\text{bpy})_3]^{2+}$ emission ($\lambda_{\text{ex}} = 450 \text{ nm}$) by the addition of complex **5**: $[\text{Ru}(\text{bpy})_3]^{2+} = 75.3 \mu\text{M}$, in borate buffer (40 mM, pH 8.0). (b) Stern-Volmer plot for quenching of $[\text{Ru}(\text{bpy})_3]^{2+}$ emission by complex **5** using the emission intensity at 587 nm. The least-squares analysis of the plot yields a quenching constant, $k_q\tau_0$, of 3400 M^{-1} .

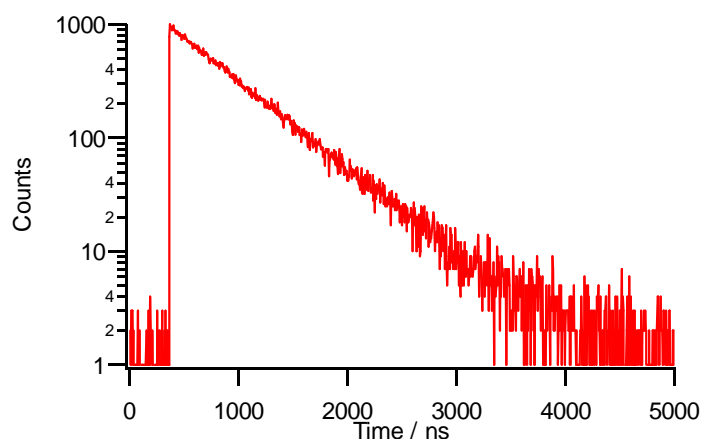


Figure 3-18. Time profile of $[\text{Ru}(\text{bpy})_3]^{2+}$ emission in borate buffer (40 mM, pH 8.0) degassed by Ar-bubbling. The concentration of $[\text{Ru}(\text{bpy})_3]^{2+}$ is 62.5 μM ; Excitation, 405 nm; Emission, 605 nm. The lifetime of 560 ns was obtained by the exponential fitting.

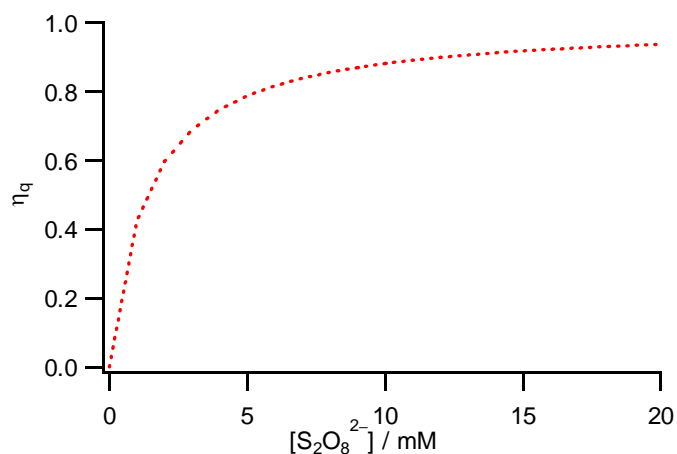


Figure 3-19. The calculated quenching efficiency of $[\text{Ru}(\text{bpy})_3]^{2+}$ by $\text{S}_2\text{O}_8^{2-}$ as a function of the concentration of $\text{S}_2\text{O}_8^{2-}$ in borate buffer (40 mM, pH 8.0).

3.2.9 Dependence on the concentration of the catalyst

Finally, the dependence of the initial oxygen evolution rate on the concentration of complex **5R** was examined. It was found that the concentration of complex **5R** incorporated into vesicle membranes was able to be roughly controlled by changing the amount of **5R** used to prepare the vesicle solution. Moreover, the concentration of **5R** in the vesicle solution was determined in each experiment by the procedure involving the treatment of the vesicle solution with sodium ascorbate and methanol described in §3.2.4.

The amount of oxygen evolved in the vesicle solution after 30 min of irradiation is shown in Fig. 3-19 as a function of the catalyst concentration (red triangles). In the vesicular system, the initial oxygen evolution rate increased almost linearly with an increase in the catalyst concentration in $[cat] < 30 \mu\text{M}$, but it decreased in the high concentration region. The numerical data of the dependence of the initial oxygen evolution rate on the concentration of **5R**, as well as the amount of **5R** employed in the vesicle preparation, are collected in Table 3-4(1).

Furthermore, the dependence on the concentration of the catalyst in the photochemical water oxidation in the homogeneous solution was also examined using complex **5** as a catalyst. The results are shown in Fig. 3-19 (blue triangles), and the numerical data are also presented in Table 3-4(2). The oxygen evolution rate increased linearly in all concentration ranges examined in these experiments.

Noteworthy, the initial oxygen evolution rate showed an almost linear relationship with $[cat]$, both in the vesicle and homogeneous solutions, but the reaction rate in the vesicular system is more than twice larger than that in the homogeneous solution in $[cat] < 30 \mu\text{M}$. These results will be discussed in the following subsection.

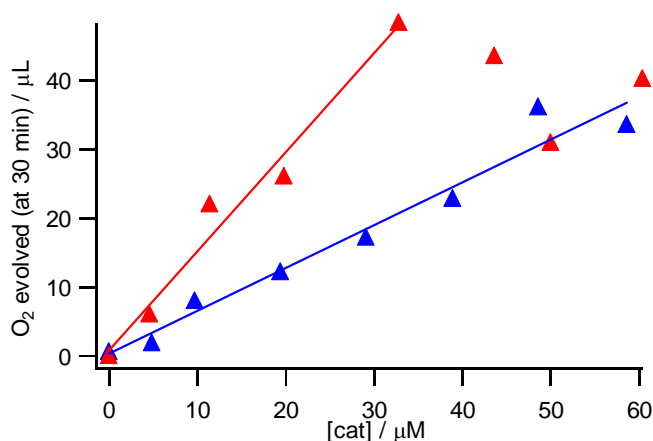


Figure 3-19. Dependence of the amount of oxygen evolved in the photochemical water oxidation on the concentration of the catalyst concentration in the vesicular system (red, complex **5R** embedded into DPPC vesicles) and in the homogeneous system (blue, complex **5**) (0.85 mM $[\text{Ru}(\text{bpy})_3]\text{Cl}_2$ and 0.5 mM $\text{Na}_2\text{S}_2\text{O}_8$ in borate buffer (40 mM, pH 8.0), $\lambda_{\text{ex}} > 390 \text{ nm}$).

Table 3-4. Dependence of the initial rate of O₂ evolution on the concentration of complex **5R** or **5** in the photochemical water oxidation.^a

(1) In vesicle solution

$n^b / \mu\text{mol}$	$[\mathbf{5R}]^c / \mu\text{M}$	Incorporation ^d / %	$v_i^e / \mu\text{mol h}^{-1}$	TOF ^f / h ⁻¹
0	0	–	0.01	–
0.131	4.6	40.0	0.50	36
0.262	11.4	49.7	1.80	52.8
0.518	19.8	43.6	2.13	35.9
0.658	32.8	56.9	3.95	40.2
0.789	43.6	63.0	3.56	27.2
0.785	50.0	72.3	2.54	16.9
1.05	60.4	65.5	3.29	18.2

(2) In homogeneous solution

$[\mathbf{5}] / \mu\text{M}$	$v_i^e / \mu\text{mol h}^{-1}$	TOF ^f / h ⁻¹
0	0.06	–
4.9	0.16	11
9.7	0.66	23
19.4	1.00	17.3
29.1	1.41	16.2
38.9	1.87	16.1
48.6	2.95	20.3
58.6	2.75	15.6

^a(1) In the vesicle solution containing **5R** or (2) the homogeneous solution of **5**, in borate buffer (40 mM, pH 8.0) in the presence of [Ru(bpy)₃]²⁺ (0.85 mM) and S₂O₈²⁻ (5.0 mM), $\lambda_{\text{ex}} > 390$ nm. ^bThe amount of **5R** used for the vesicle preparation. ^cThe concentration of **5R** in the vesicle solution determined by UV-Vis spectroscopy. ^dThe amount of **5R** incorporated vesicles as a percentage to that employed for vesicle preparation. ^eThe amount of oxygen evolved by photoirradiation for 30 min. ^fTurnover frequency of the oxygen evolution with respect to the catalyst.

3.2.10 Reaction mechanism

From the quenching experiments, it is clear that the photoreaction starts from oxidative quenching of $[\text{Ru}(\text{bpy})_3]^{2+}$ * by $\text{S}_2\text{O}_8^{2-}$ to generate $[\text{Ru}(\text{bpy})_3]^{3+}$. This is consistent with the case of the photochemical reaction discussed in Chapter 2.

As previously stated in §2.2.9, it has been reported that water oxidation reaction catalyzed by $\text{Ru}(\text{bda})\text{L}_2$ proceeds through the catalytic cycle depicted in Scheme 2-2. Moreover, Sun *et al.* have reported that the reaction rate of chemical water oxidation using CAN as an oxidant depends on $[\text{cat}]^2$, and they have also revealed that the rate-determining step is dimerization of $\text{Ru}(\text{V})=\text{O}$ by UV-Vis absorption spectrum measurement using a stopped-flow system.⁴

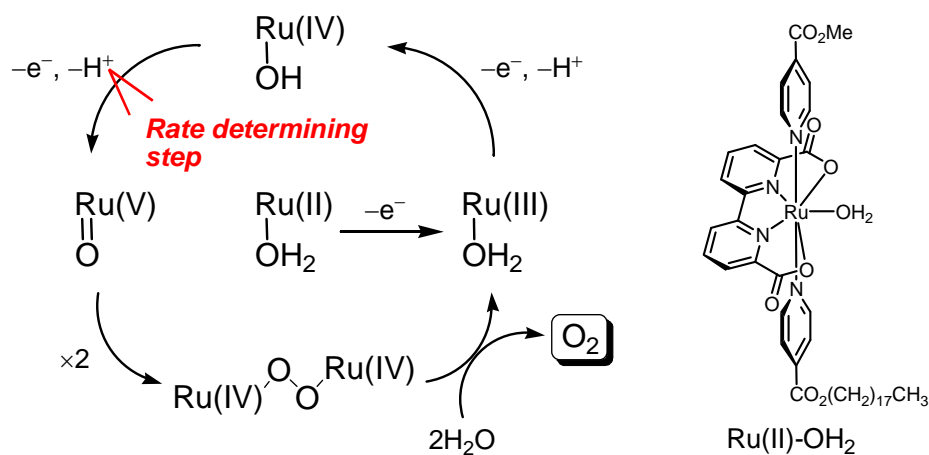
However, as described in §3.2.9, the fact that the reaction rate was linear to the catalyst concentration suggests that only one molecule derived from the catalyst is involved in the rate-determining step in the photochemical water oxidation. This is not consistent with the mechanism reported by Sun *et al.* Considering that the steady-state concentration of the oxidant in the photochemical water oxidation, $[\text{Ru}(\text{bpy})_3]^{3+}$, is lower than that of Ce(IV) in the chemical water oxidation, and that it has been reported that the rate constant for the oxidation of the Ru(IV) species of $\text{Ru}(\text{bda})(\text{pyMe})_2$ is relatively low ($2.3 \times 10^5 \text{ M}^{-1} \text{ s}^{-1}$)⁴, the rate-determining step of the photochemical water oxidation is thought to be shifted from the dimerization of $\text{Ru}(\text{V})=\text{O}$ to the electron transfer step between the Ru(IV) species of the catalyst and the oxidant, $\text{Ru}(\text{IV})-\text{OH} \rightarrow \text{Ru}(\text{V})=\text{O}$. Thus, I propose that the photochemical water oxidation proceeds by the mechanism illustrated in Scheme 3-4.

As shown in Fig. 3-9, since the steady-state concentration of the Ru(III) species of the catalyst in the vesicular system was found to be notably higher than that in the homogeneous solution, it is likely that the oxidation steps are accelerated by the high concentration of reactive species in the vesicular system, although the concentration of Ru(IV) species could not be estimated by UV-Vis absorption measurement unfortunately. This could be the reason for the higher efficiency of the photochemical water oxidation in the vesicular system than that in the homogeneous solution.

Finally, the decrease in the oxygen evolution rate in $[\text{cat}] > 30 \mu\text{M}$ in the vesicular

system could be tentatively explained by the possibility that the undesired electron transfer reactions between the catalysts such as $\text{Ru(II)} + \text{Ru(IV)} \rightarrow 2\text{Ru(III)}$ are accelerated due to the high local concentration of the catalysts in vesicle membranes.

Scheme 3-4. Plausible mechanism of the photochemical water oxidation catalyzed by $\text{Ru(bda)(pyCO}_2\text{Me)(pyCO}_2\text{Ocd)}$ (**5R**) embedded into vesicle membranes.



3.3 Summary

In this chapter, the synthesis of newly-designed amphiphilic Ru complex **5R**, and its incorporation behavior into vesicle membranes and catalytic activity toward the photochemical water oxidation in the vesicular system were described. UV-Vis absorption spectral measurement of the extract from the vesicle solution revealed that complex **5R** can be incorporated into vesicle membranes and allowed me to determine the concentration of **5R**. The incorporation of complex **5R** into vesicle membranes was also supported by the extraction experiment using 1-octanol/water. When the vesicle solution containing $[\text{Ru}(\text{bpy})_3]^{2+}$ and $\text{S}_2\text{O}_8^{2-}$ in the outer aqueous phase and complex **5R** embedded into vesicle membranes was irradiated by visible light ($\lambda > 390 \text{ nm}$), generation of molecular oxygen was observed by GC analysis. In this way, the construction of the photochemical water oxidation system utilizing vesicles as a reaction field was achieved. The turnover number and turnover frequency of oxygen evolved with respect to the catalyst are more than twice as much as those in the homogeneous solution.

Dependences of the initial oxygen evolution rate on the concentration of the sensitizer $[\text{Ru}(\text{bpy})_3]^{2+}$, the electron acceptor $\text{S}_2\text{O}_8^{2-}$, and the catalyst were examined, and the following results were obtained. (1) The initial oxygen evolution rate increased with an increase in the sensitizer concentration in $[\text{sens}] < 0.5 \text{ mM}$. By calculating the intensity of the light absorbed by the sensitizer, it was found that incident light was almost fully absorbed by the sensitizer in $[\text{sens}] > 0.5 \text{ mM}$. (2) The initial oxygen evolution rate was saturated at the point where the concentration of the electron acceptor was nearly equal to 5 mM. Quenching experiments of $[\text{Ru}(\text{bpy})_3]^{2+}$ emission revealed that the excited sensitizers were quenched predominantly by $\text{S}_2\text{O}_8^{2-}$ under the typical photochemical reaction condition, and the quenching efficiency by $\text{S}_2\text{O}_8^{2-}$ was saturated in $[\text{S}_2\text{O}_8^{2-}] > 5 \text{ mM}$. The water oxidation efficiency decreased in $[\text{S}_2\text{O}_8^{2-}] > 20 \text{ mM}$ due to the aggregation of vesicles to form precipitate in the presence of the high concentration of electrolyte. (3) In the vesicular system, the initial oxygen evolution rate increased linearly with an increase in the catalyst concentration in $[\text{cat}] < 30 \text{ }\mu\text{M}$. On the other hand, in the homogeneous system, the reaction rate increased linearly in $[\text{cat}] < 60$

μM , but the slope was almost half of that in the vesicular system.

On the basis of the reaction mechanism reported by Sun and co-workers, the rate determining step of the photochemical water oxidation is thought to be the oxidation step of the Ru(IV) species, $\text{Ru(IV)-OH} \rightarrow \text{Ru(V)=O}$. UV-Vis absorption spectra of the reaction solution demonstrated that the steady-state concentration of the Ru(III) species of complex **5R** in the vesicular system was relatively higher than that in the homogeneous solution. This suggests that the reaction in the vesicular system is accelerated by the higher concentration of reactive species involved in the catalytic cycle.

As just described above, my study in this chapter demonstrated that vesicles work as a reaction field of the photochemical water oxidation. It should also be noted that the oxygen evolution rate in the vesicular system is more than twice as much as that in the homogeneous solution under the almost same conditions. This result indicates that vesicles can enhance the catalytic activity of the Ru complex in the photochemical water oxidation.

3.4. Experimental

Materials. Most of chemicals were purchased from Sigma-Aldrich, Tokyo Kasei Kogyo Co. Ltd. (TCI), Wako Pure Industries Ltd. (Wako), and Kanto Chemical Co. Inc unless otherwise noted. All reagents were used as received unless otherwise stated. Spectrum grade organic solvents and distilled water used for spectroscopic measurements and water oxidation experiments were purchased from Wako. 1,2-Dipalmitoyl-*sn*-glycero-3-phosphocholine (DPPC) was purchased from Avanti Polar Lipids and used without further purification. Aluminum oxide 90 active neutral for column chromatography (70-230 mesh) was purchased from Merck KGaA. Sephadex G-50 used for vesicle preparation was purchased from Amersham Biosciences.

General methods. ^1H NMR spectra were recorded on a Bruker AVANCE 500 spectrometer. Chemical shifts are reported by using tetramethylsilane ($\delta = 0.00$) in CDCl_3 for ^1H NMR as internal standards. Electrospray ionization time-of-flight (ESI-TOF) mass spectra were obtained using a Waters Xevo G2-S ToF mass spectrometer. UV-Vis absorption spectra were recorded on a JASCO V-560 spectrometer. Phosphorescence spectra were recorded on a JASCO FP-777 spectrofluorometer. Phosphorescence lifetimes were measured on Hamamatsu Photonics Quantaaurus-Tau. Melting points (m.p.) were recorded on YAZAWA BY-2. Elemental analyses were performed using an Elementar vario MICRO cube at the Microanalytical Laboratory (Department of Chemistry, School of Science, The University of Tokyo). Sonication was carried out using IWAKI ultrasonic cleaner USC-100Z38S-22 or SHARP ultrasonic cleaner UT-206H. Irradiation was carried out using a xenon arc lamp (Wacom, lamp house HX500W) with a cut-off filter (TOSHIBA L-39). Gas chromatographs were recorded on a YANACO gas chromatograph G2700TF (TCD analytic column: 3 mm \times 3 mm stainless column, activated carbon (60-80 mesh)).

Preparation of octadecyl isonicotinate (pyCO₂Ocd)⁷. A solution of isonicotinic acid (1.48 g, 12.0 mmol) in thionyl chloride (5 mL) was refluxed for 2 h. Excess thionyl chloride was removed under reduced pressure and the residue was dried under vacuum for 2 h to afford isonicotinoyl chloride. 1-Octadecanol (2.70 g, 9.98 mmol) and *N,N*-dimethyl-4-aminopyridine (249.2 mg, 2.04 mmol) were dissolved in CH₂Cl₂ which was distilled over CaH₂ prior to use. To the solution was slowly added isonicotinoyl chloride prepared as shown above. The mixture was stirred for 14 h at room temperature, and the resulting suspension was quenched by water, extracted with CH₂Cl₂. The organic layer was separated, dried over Na₂SO₄, filtered, and concentrated under reduced pressure to give pyCO₂Ocd (3.62 g, 96%) as a white solid; ¹H NMR (500 MHz, CDCl₃) δ 8.78 (dd, *J* = 4.5, 1.5 Hz, 2H), 7.85 (dd, *J* = 4.5, 1.5 Hz, 2H), 4.35 (t, *J* = 7.0 Hz, 2H), 1.78 (quint, *J* = 7.0 Hz, 2H), 1.44 (quint, *J* = 7.0 Hz, 2H), 1.26-1.37 (m, 28H), 0.88 (t, *J* = 6.8 Hz, 3H).

Synthesis of Ru(bda)(pyCO₂Me)(pyCO₂Ocd) (5R). To a suspension of H₂bda (48.9 mg, 200 μmol) and Ru(DMSO)₄Cl₂ (97.4 mg, 201 μmol) in methanol (4 mL) deaerated by passing nitrogen through it, triethylamine (0.16 mL, 1.1 mmol) was added under nitrogen atmosphere. After refluxing for 7 h, the mixture was filtered and washed by cold methanol to give brown solid containing Ru(bda)(DMSO)₂⁸. To a suspension of the brown solid in deaerated THF (4 mL) was added a solution of pyCO₂Me (52.2 mg, 381 μmol) and pyCO₂C18 (147.8 mg, 394 μmol) in THF (4 mL), and the mixture was then refluxed for 2 days under nitrogen atmosphere. The resulting mixture was concentrated under reduced pressure, and the residue was purified by column chromatography on aluminum gel (CH₂Cl₂-methanol (50 : 1, 20 : 1) as eluent) to give **5R** (47 mg, 27%) as a dark red solid; m.p. > 300 °C; ¹H NMR (500 MHz, CDCl₃) δ 8.24 (d, *J* = 7.6 Hz, 2H), 8.12 (d, *J* = 7.6 Hz, 2H), 8.00 (d, *J* = 6.0 Hz, 2H), 7.99 (d, *J* = 6.0 Hz, 2H), 7.78 (t, *J* = 7.6 Hz, 2H), 7.57 (d, *J* = 6.0 Hz, 2H), 4.27 (t, *J* = 6.5 Hz, 2H), 3.89 (s, 3H), 1.69 (quint, *J* = 6.5 Hz, 2H), 1.25 (brs, 30H), 0.88 (t, *J* = 6.5 Hz, 3H); LRMS (ESI): *m/z*⁺ = 857.3 (M + H⁺), calcd: 857.3; Anal. Calcd for

$C_{43}H_{54}N_4O_8Ru \cdot 2H_2O$: C, 57.90; H, 6.55; N, 6.28. Found: C, 57.81; H, 6.26; N, 6.14.

Vesicle preparation. A chloroform solution of DPPC (12 μmol) and **5R** (0.52 μmol) was concentrated under reduced pressure to form a thin film in a flask. The film was dried under vacuum overnight, and then dispersed in borate buffer (40 mM, pH 8.0) at 60 $^{\circ}\text{C}$ by vortex mixing. The dispersion was treated with ultrasonic process at 55–60 $^{\circ}\text{C}$ under argon for 30 min to form a vesicle solution of DPPC containing **5R**. The vesicle solution was passed through a column with Sephadex G-50 equilibrated with a buffer solution to remove **5R** outside vesicles and 11.4 mL of a vesicle solution was obtained.

Determination of the partition coefficient in 1-octanol/water. 1 mL of saturated solution of complex **5R** in 1-octanol was diluted to 10 mL, and UV-Vis absorption spectrum was measured. After that, 10 mL of water was added to 10 mL of the diluted octanol solution, and the mixture was vigorously shaken. The aqueous phase and octanol phase was separated, and then the UV-Vis spectra of both phases were measured. The concentration of **5R** in the aqueous phase was estimated from the absorbance decrease of the octanol solution after the extraction. The partition coefficient, P_{ow} , was determined by an equation $P_{ow} = C_o/C_w$, where C_o and C_w represent the concentration of **5R** in the octanol phase and the aqueous phase, respectively.

Photochemical water oxidation in the vesicular system. A vesicle solution (3.0 mL) containing **5R** was placed in a quartz cell (10 mm \times 10 mm), and to the solution were added $[\text{Ru}(\text{bpy})_3]\text{Cl}_2 \cdot 6\text{H}_2\text{O}$ (1.9 mg, 2.5 μmol) and $\text{Na}_2\text{S}_2\text{O}_8$ (3.6 mg, 15 μmol). Then, the solution was irradiated using a xenon arc lamp through a cut-off filter ($\lambda > 390$ nm) after passing argon through the solution for 1 h to remove air. 0.5 mL of gas was taken from the gas phase of the quartz cell by a gas tight syringe, and analyzed by gas chromatograph to determine the quantity of generated oxygen.

Photochemical water oxidation in the homogeneous solution. A solution of Ru(bda)(pyCO₂Me)₂ (**5R**) (0–59 μM) in borate buffer (40 mM, pH 8.0, 3.0 mL) was placed in a quartz cell (10 mm × 10 mm), and to the solution were added [Ru(bpy)₃]Cl₂·6H₂O (1.9 mg, 2.5 μmol) and Na₂S₂O₈ (3.6 mg, 15 μmol). Then the solution was irradiated using a xenon arc lamp through a cut-off filter ($\lambda > 390$ nm) after passing argon through the solution for 1 h to remove air. 0.5 mL of gas was taken from the gas phase of quartz cell by a gas tight syringe, then it was analyzed by gas chromatograph to determine the quantity of generated oxygen.

Emission quenching study. The phosphorescence quenching by the addition of S₂O₈²⁻ was recorded by repetition of the following cycles; to the solution of [Ru(bpy)₃]²⁺ (52.4 μM) in borate buffer (40 mM, pH 8.0) was added a certain volume of a solution of [Ru(bpy)₃]²⁺ in borate buffer containing Na₂S₂O₈ (2.20 mM), and the phosphorescence lifetime was measured. Relative phosphorescence lifetimes (τ_0/τ) were determined by measuring phosphorescence lifetimes at 615 nm.

Cyclic voltammetry. CH₂Cl₂ was distilled prior to use for the electrochemical measurement. Cyclic voltammetry was carried out in nitrogen-purged CH₂Cl₂ using a HOKUTO DENKO potentiostat/galvanostat HAB-151 equipped with a Runtime Corporation X-Y Recorder (Voltam-REC). Tetrabutylammonium perchlorate (0.1 M) in CH₂Cl₂ was used as a supporting electrolyte. The conventional three-electrode configuration consisted of a glassy carbon working electrode, a platinum wire auxiliary electrode and a Ag/Ag⁺ reference electrode.

References and notes

1. (a) B. Katušin-Ražem, M. Wong, J. K. Thomas, *J. Am. Chem. Soc.*, **1978**, *100*, 1679.
(b) W. E. Ford, J. W. Otvos, M. Calvin, *Nature*, **1978**, *274*, 507.
2. K. Watanabe; S. Takizawa; S. Murata, *Chem. Lett.*, **2011**, *40*, 345.
3. J. L. Dempsey; J. R. Winkler; H. B. Gray, *J. Am. Chem. Soc.*, **2010**, *132*, 1060.
4. L. Duan; F. Bozoglian; S. Mandel; B. Stewart; T. Privalov; A. Llobet; L. Sun, *Nat. Chem.*, **2012**, *4*, 418.
5. L. Duan; Y. Xu; P. Zhang; M. Wang; L. Sun, *Inorg. Chem.*, **2010**, *49*, 209.
6. S. Berardi; G. L. Ganga; M. Natali; I. Bazzan; F. Puntoriero; A. Sartorel; F. Scandola; S. Campagna; M. Bonchio, *J. Am. Chem. Soc.*, **2012**, *134*, 11104.
7. T. Mizushima; A. Yoshida; A. Harada; Y. Yoneda; T. Minatani; S. Murata, *Org. Biomol. Chem.*, **2006**, *4*, 4336.
8. U. Oesch; Z. Brzózka; A. Zu; B. Rusterholz; G. Suter; H. V. Pham; D. H. Welti; D. Ammann; E. Pretsch; W. Simon, *Anal. Chem.*, **1988**, *58*, 2285.
9. (a) F. Li; B. Zhang; X. Li; Y. Jiang; L. Chen; Y. Li; L. Sun, *Angew. Chem. Int. Ed.*, **2011**, *50*, 12276. (b) Y. Gao; X. Ding; J. Liu; L. Wang; Z. Lu; L. Li; L. Sun, *J. Am. Chem. Soc.*, **2013**, *135*, 4219. (c) L. Wang; M. Mirmohades; A. Brown; L. Duan; F. Li; Q. Daniel; R. Lomoth; L. Sun; L. Hammarström, *Inorg. Chem.*, **2015**, *54*, 2742.

Chapter 4 Conclusion

In this doctoral thesis, “construction of photochemical water oxidation system catalyzed by ruthenium complexes in vesicles” was studied with the aim of the construction of vesicular water splitting systems mimicking natural photosynthesis. In Chapter 1, natural photosynthetic system was outlined as a basis of this study. In addition, artificial mimics of photosynthesis were introduced in the following three points of view: (i) light harvesting in the antenna complex, (ii) charge separation in the reaction center, and (iii) energy conversion where charge separation energy is utilized to synthesize chemical species having high chemical potential.

Sun and co-workers have reported that the Ru complex Ru(bda)(pyMe)₂ works as a highly active water oxidation catalyst. On the basis of this report, in Chapter 2, a series of complexes Ru(bda)(pyR)₂ **1–6** having R = OMe, Me, H, Br, CO₂Me, and CF₃ were prepared, and examined for their catalytic activities in the chemical and photochemical water oxidation reactions to find suitable structures for the photochemical water oxidation in vesicles. Chemical water oxidation reactions catalyzed by complexes **1–6** were conducted and their catalytic activities were evaluated using Ce(IV) as an oxidant. Complexes **4–6** (R = Br, CO₂Me, CF₃) exhibited especially high catalytic efficiency, while complex **1** (R = OMe) catalyzed the reaction more efficiently than complex **2** and **3** (R = Me, H). Then, the catalytic activity of complexes **1–6** in the photochemical water oxidation sensitized by [Ru(bpy)₃]²⁺ was examined. As a result, the catalytic activity of complexes **5** and **6** (R = CO₂Me, CF₃) was notably high, and that of complex **1** (R = OMe) was relatively higher than that of complex **2** and **3** (R = Me, H). Based on the reaction mechanism proposed by Sun *et al.*, the acceleration by electron-withdrawing groups is thought to be due to a decrease in the activation energy of dimerization of the Ru(V)=O species involved in the catalytic cycle. Moreover, I consider that the electron-donating group accelerates the reaction because the Ru(IV) species are oxidized in an efficient way, and/or dimerization of Ru(V)=O is accelerated by the enhanced π-π interaction between the axial pyridine ligands of the two Ru complexes.

In Chapter 3, amphiphilic Ru complex **5R** having a long alkyl chain on the pyridine

ligand linked by an ester bond was synthesized. It was found that complex **5R** was moderately incorporated into vesicles, while complex **5** was not incorporated sufficiently. Photochemical water oxidation catalyzed by complex **5R** embedded into vesicle membranes was conducted using $[\text{Ru}(\text{bpy})_3]^{2+}$ as a sensitizer and $\text{S}_2\text{O}_8^{2-}$ as a sacrificial electron acceptor, both of which are located in the outer aqueous phase. Irradiation of the vesicle solution by visible light ($\lambda > 390 \text{ nm}$) resulted in generation of molecular oxygen. Thus, the construction of the photochemical water oxidation system using vesicles as a reaction field was successfully achieved. Then, the dependences of the initial water oxidation rate on the concentration of the sensitizer, the electron acceptor, and the catalyst were investigated in the vesicular system. The water oxidation rate was saturated at $[\text{sens}] \sim 0.5 \text{ mM}$ and $[\text{S}_2\text{O}_8^{2-}] \sim 5 \text{ mM}$, where the incident light was almost fully absorbed by $[\text{Ru}(\text{bpy})_3]^{2+}$, and almost all the excited sensitizers were quenched by $\text{S}_2\text{O}_8^{2-}$, respectively. The initial water oxidation rate increased almost linearly with the increase of the catalyst concentration in $[\text{cat}] < 30 \text{ }\mu\text{M}$. Photochemical water oxidation in the homogeneous solution catalyzed by complex **5** was also examined for comparison. It is noted that both the turnover number and the initial turnover frequency of the oxygen evolution in the vesicular system are more than twice as much as those in the homogeneous solution. On the basis of the reaction mechanism presented in Chapter 2 and the fact that the reaction rate depended linearly on the catalyst concentration, I proposed that the rate-determining step of the catalytic cycle was oxidation of the Ru(IV) species to Ru(V) in the photochemical water oxidation. It is likely that the oxidation step to generate Ru(V) species of the catalyst is faster in the vesicular system because of the high concentration of the reactive species involved in the catalytic cycle, which is the reason for the larger efficiency in the photochemical water oxidation in the vesicular system.

This study is the first example revealing that the catalytic activity of the water oxidation catalyst is enhanced by the incorporation into vesicles. I believe that water splitting into hydrogen and oxygen molecules in vesicles will be achieved in the future using this water oxidation system by combining with vesicular hydrogen generation

system, mediated by sufficient redox couples. Furthermore, if the water oxidation and water reduction catalysts can be incorporated at the inner and outer surfaces of the vesicle membranes, respectively, photoinduced electron transport across the vesicle membranes and subsequent redox reactions inside and outside the vesicles are able to be achieved in one vesicle. This is one of the final goals to the light-energy conversion system using vesicles as a model of natural photosynthetic system.

Acknowledgement

I sincerely thank Professor Shigeru Murata (The University of Tokyo) for his considerate guidance, supports on this dissertation, and encouragement during the course of this work by thoughtful advices.

I deeply thank Dr. Shin-ya Takizawa (The University of Tokyo) for his supports on this dissertation and helpful discussion.

I also thank Dr. Naoya Ikuta (The University of Tokyo) for a lot of meaningful suggestions.

I would like to thank my thesis committee in The University of Tokyo, Professors Shuichi Hiraoka, Yutaka Matsuo, Masayuki Satake, and Hayato Thuji for sparing their time to review this dissertation.

I would like to thank Professor Shuichi Hiraoka and Dr. Tatsuo Kojima (The University of Tokyo) for the measurement of ESI-TOF mass spectra.

I would like to thank all the members of Murata's laboratory for their discussion and advices.

Finally, I would like to express gratitude to my family for their continuous encouragement and financial support.

List of Publications

1. "Substituent Effects on Physical Properties and Catalytic Activities toward Water Oxidation in Mononuclear Ruthenium Complexes" Yoichi Sato, Shin-ya Takizawa, Shigeru Murata, *Eur. J. Inorg. Chem.* **2015**, 5495.
2. "Photochemical Water Oxidation System Using Ruthenium Catalysts Embedded into Vesicle Membranes" Yoichi Sato, Shin-ya Takizawa, Shigeru Murata, *J. Photochem. Photobiol. A: Chem.* in press.